UNIVERSITY OF OKLAHOMA

GRADUATE COLLEGE

3-D GEOMETRY AND KINEMATIC EVOLUTION OF THE KUPE INVERSION STRUCTURE, SOUTHERN TARANAKI BASIN, NEW ZEALAND

A THESIS

SUBMITTED TO THE GRADUATE FACULTY

in partial fulfillment of the requirements for the

Degree of

MASTER OF SCIENCE

By

SPENCER CLAYTON
Norman, Oklahoma
2017

3-D GEOMETRY AND KINEMATIC EVOLUTION OF THE KUPE INVERSION STRUCTURE, SOUTHERN TARANAKI BASIN, NEW ZEALAND

A THESIS APPROVED FOR THE
CONOCOPHILLIPS SCHOOL OF GEOLOGY AND GEOPHYSICS

BY

_____
Dr. Shankar Mitra, Chair

_____
Dr. Kurt Marfurt

_____
Dr. Matthew Pranter

Table of Contents

List of Tables vi

List of Figures vii

Abstract xiv

Chapter 1: Introduction 1

1.1 Overview 1

1.2 Structure of the Southern Taranaki Basin 3

1.3 Stratigraphy of the Southern Taranaki Basin 7

1.4 Geologic History of the Southern Taranaki Basin 10

1.5 Data Used 11

Chapter 2: Method 14

2.1 Seismic Horizon Interpretation 14

2.2 Structural Interpretation and Depth Conversion 19

2.3 Fault Modeling Theory 21

2.4 Manaia Fault Modeling Method 29

2.5 Rua Fault Modeling Method 32

2.6 Unfolding Theory and Method 35

Chapter 3. Geometry and Evolution of the Kupe Structure 39

3.1 Maps 39

3.2 Cross Sections 46

3.3 3D Geometry 61

3.4 Restorations 66

Chapter 4. Discussion 70

4.1 Fault Propagation in Inversion Structures 70

4.2 Deep fault geometry 81

Summary..... 85

References 86

List of Tables

Table 1. Wells within the study area, the wells used in the study are indicated. 11

Table 2. Acquisition parameters of the Kerry 3D survey. Modified from CGG Australia Services Pty Ltd, 2004. 13

Table 3. Seismic horizons interpreted with their approximate lithostratigraphic formation and reflector type picked. 16

List of Figures

Figure 1. Location of the Taranaki Basin of New Zealand outlined in red. Modified from Wandrey (2013) 2

Figure 2. Location of large scale faults and data available for interpretation. (Reilly, 2015) 3

Figure 3. Schematic cross sections showing the general structures found in the Southern Taranaki Basin. Reverse faults, normal faults, and inversion structures are present. The faults with hanging wall thickening of the green Cretaceous units are indicative of inversion. (Reilly, 2015) 4

Figure 4. Basic concept of inversion on a concave-upward listric fault. The top figure shows the resulting bed geometries of pregrowth, syngrowth, and postgrowth units during extension. The second image shows the compressional reactivation of the fault. Compressional reactivation causes reverse offset of hanging wall thickening units. It also causes both reverse and normal offsets along the fault separated by the null point which is the location with no apparent offset. The final image shows how further compression could result in no apparent normal offset. 6

Figure 6. General stratigraphy of the Southern Taranaki Basin with ages and relative sea level. Known oil and gas reservoir units within the Taranaki basin are shown with grey boxes to signify the wells located within the Kupe area. Modified from King and Thrasher (1996). 9

Figure 7. The data used by Fohrmann (2012) to produce regional maps. The Kerry 3D dataset is shown in gray with gray lines indicating the location of 2D seismic lines. Significant faults within the area as well as oil wells are also shown. 12

Figure 8. Stratigraphy of the Kupe area with ages. The seismic horizons are shown in the center of the figure. Modified from Fohrmann (2013) using units from Bull (2015). 17

Figure 9. The left side shows the original Kerry3D data and the right shows the seismic after applying a low pass filter to suppress high frequency multiples. 18

Figure 10. Idealized representation of the goals of fault modeling. Image A shows how some beds may be well imaged while others are poorly imaged. Image B and C show how different interpretations would suggest different geometries at depth. (Dula, 1991) 22

Figure 11. Geometric construction for modeling a fault using inclined shear. The fault can be modeled using the red bed with apparent reverse offset of the blue bed with apparent normal offset. The parameters needed are the apparent horizontal extension (E') or apparent horizontal compression (C'), the shear angle (α), and a deformed bed geometry. 25

Figure 12. Inclined shear theoretical geometry after compression or extension. The grey hashed polygons indicate the areas which are in balance after deformation. In compression, the area of uplift is equal to the area which would overlap with horizontal translation. In extension, the area of subsidence is equal to the area below the fault block with horizontal translation. 27

Figure 13. Observed null point bed geometry. The red dashed line is an extension of the back-limb dip. The area above and below the line is in near area balance. 28

Figure 14. The workflow used to area balance the structure. After establishing the location of the fault using seismic interpretation of the hanging wall and footwall fault

intersections the fault is extended below at 60 degrees. The hanging wall bed is then forward modeled from the original position such that the area above (A') and below (A) the observed bed geometry to the modeled bed are in area balance. This gives the horizontal compression parameter used for inclined shear modeling. 30
Figure 15. After the horizontal compression parameter is set by area balancing, the inclined shear method is used to model the fault. In this figure, the bed is extended beyond the available seismic data to model the fault to a greater depth. 31
Figure 16. Combined movement vector to accommodate movement along two faults. Line AB shows the displacement of the bed caused by movement on the Manaia fault and the line BC shows the displacement caused by the movement on the Rua fault. The Combined vector AC shows the total displacement of the bed from the two faults. 33
Figure 17. The iterative process used to model the Rua fault. The dashed blue line is the initial geometry of the Rua fault and the solid blue line shows the geometry after forward modeling on the Manaia fault. The dashed pink line shows the initial bed geometry and the solid pink shows an intermediary geometry to account for movement on the Manaia fault. The bed is then forward modeled on the Rua fault to the final position of the bed. 34
Figure 18. A schematic comparison of the observed fault propagation style with trishear. A and B show the volume gain and loss in the hanging wall and footwall which balance out in trishear. The combined deformation is shown in C with the location of the translated blocks outlined in red. The observed fault propagation style in the study area is shown in D. Modified from Erslev (1991). 36

Figure 19. A comparison of various flattening techniques. The template line is shown in pink and is flattened to the dashed pink position. The solid red line is passively flattened and the modeled position using inclined shear is shown as a dashed red line. The solid purple lines show the different outputs and the solid blue line is the result of the flexural slip algorithm which was used for restorations. 38
Figure 20. Basement depth map. 40
Figure 21. Basement time map. 41
Figure 22. P10 depth map. 42
Figure 23. P10 time map. 43
Figure 24. N40 depth map. 44
Figure 25. N40 time map. 45
Figure 26. Cross section legend. 47
Figure 27. Map of the depth to basement with cross section locations to show their location relative to fault locations. 48
Figure 28. Depth cross section A. 49
Figure 29. Time cross section A. 49
Figure 30. Depth cross section B. 50
Figure 31. Time cross section B. 50
Figure 32. Depth cross section C. 51
Figure 33. Time cross section C. 51
Figure 34. Depth cross section D. 52
Figure 35. Time cross section D. 52
Figure 36. Depth cross section E. 53

Figure 37. Time cross section E. 53
Figure 38. Depth cross section F. 54
Figure 39. Time cross section F. 54
Figure 40. Depth cross section G. 55
Figure 41. Time cross section G. 55
Figure 42. Depth cross section H. 56
Figure 43. Time cross section H. 56
Figure 44. Depth cross section I. 57
Figure 45. Time cross section I. 57
Figure 46. Depth cross section J. 58
Figure 47. Time cross section J. 58
Figure 48. The 3D model showing the units deposited during extension. The Pink horizon is the approximate reservoir horizon. 61
Figure 49. Fault throw at the end of extension. The Manaia fault is shown with solid lines and the Rua fault is shown with dashed lines. 63
Figure 50. Cumulative fault throw at the end of compression. The Manaia fault is shown with solid lines and the Rua fault is shown with dashed lines. The percent of fault heave lost to fault propagation is shown as a solid black line. 64
Figure 51. P10 structure map showing the location of the potential slump features. 65
Figure 52. Section B inclined shear restoration. 66
Figure 53. Section E inclined shear restoration. 67
Figure 54. Section E restored section. 68
Figure 55. Section I inclined shear restoration. 69

Figure 56. Section I restored section. 69
Figure 57. Structural cross section of the Maui structure in the Taranaki basin of New Zealand from Abbott (1990) showing folding adjacent to a compressionally reactivated normal fault. 70
Figure 58. Structural cross section of the Arreton structure in the Wessex basin of southern England from Underhill and Patterson (1998) showing folding adjacent to a compressionally reactivated normal fault. 71
Figure 59. Structural cross section of the Sakala structure in the East Java Sea from Mitra (2005) showing folding adjacent to a compressionally reactivated normal fault. 72
Figure 60. Fault-independent buckle folding through buttressing of incompetent units. The footwall is un-deformed and deformation is confined to the hanging wall. (Cooper, 1989) 73
Figure 61. Fault propagation accommodated by back thrusts. (Underhill and Patterson, 1998) 74
Figure 62. A representation of how the percent area lost and gained can be calculated. The area within the downward and upward folding deformation panels are calculated between the modeled horizon and the observed horizon. This is then compared to the total area below the modeled horizon within the deformation panel. The areas A/B=A'/B' and C/D=C'/D'. 75
Figure 63. The basic approach to unfolding uses the length of the modeled bed to the base of the triangular deformation zone (Line AE) and the length from the modeled bed to the observed horizon (AB) to maintain a constant percent length change. A bed can be passively unfolded using AB/AE=X/DE where X is the unknown length which the

bed should be unfolded. The unknown X should move the bed more than the length DC to restore the bed above the modeled position resulting in a drape folded geometry. ... 77
Figure 64. Comparison of passive unfolding techniques of the purple P00 horizon using the pink P10 as a template. The red line shows the output using the new technique and the blue line shows the output using flexural slip with the fault as a pin. 79
Figure 65. Basement horizon structure map from Fohrmann et al. (2012) 82
Figure 66. P10 horizon structure map from Fohrmann et al. (2012)..... 83
Figure 67. The deep fault geometry is shown on the gravity model created by Stagpoole and Nicol (2008). Below that the deep fault geometry is expanded to show detail. The dashed black line shows the extent of the fault which can be modeled from the horizon do to the presence of the Taranaki fault which is shown in black. 84

Abstract

The Southern Taranaki Basin underwent extension during the Late Cretaceous to Eocene, followed by a compression during the Oligocene to the Late Miocene, resulting in inversion of some of the pre-existing normal faults. The style of the structures and related faults varies depending on the relative magnitudes of extension and compression, and the orientation of the faults. The Kupe structure is related to two overlapping faults, the Manaia and Rua faults, with different magnitudes of slip along structural trend. A series of structural cross sections using the Kerry 3D seismic dataset and existing regional maps was made to develop a 3-D structural model of the Kupe structure. Kinematic reconstructions of the cross sections were used to validate the interpretations and understand the structural evolution. The magnitude of extension on the Manaia fault unit is greatest to the north, and decreases significantly to the south where it overlaps with the Rua fault. Inversion occurred during the Oligocene to Miocene, with the greatest magnitude of compression in the central part of the area. The inversion occurred primarily on the Manaia fault in this area, but fault slip was progressively transferred to the Rua fault in the south. Fault-bend folding along a listric fault with a deep decollement level within the basement was primarily responsible for the formation of the structure, but some fault-propagation folding and/or fault-independent folding was also important.

There is considerable variation in the structural styles along the trend of the structure. The northern part is dominated by a broad structure formed by fault-bend folding with a broad zone of fault propagation folding. The central transfer between the two faults is marked by a steep front limb and a tight zone of fault propagation folding

is needed to explain this geometry. This area includes the structural closure drilled by the producing Kupe South well. The southern area is marked by a broad structure with a gently dipping front limb, and the progressive transfer of inversion from the Manaia to the Rua fault.

Chapter 1: Introduction

1.1 Overview

The Taranaki Basin is located west of the north Island of New Zealand (Figure 1). The Taranaki basin is bounded by the Taranaki fault to the east, the Challenger Plateau to the southwest, and a poorly defined boundary to the Northwest where sediments thin. The Taranaki basin is believed to contain 464 MMBO, 9.343 TCFG, and 389 MMBNGL of undiscovered resources (Wandry, 2013), leading to intensive study of the geology of the region and the availability of a wide range of data. This study will be focused on the Kupe Inversion structure located in the southeastern part of the Taranaki Basin.

The Kupe structure is a laterally continuous asymmetric fault cored anticline which formed as the result of compressional reactivation of a normal fault. It has a series of oil and gas fields along its crest. This study is focused on better understanding the geometry and kinematics of the structure. Better characterization of the geometry and kinematics of the structure can be used to better locate and evaluate potential hydrocarbon traps in the area and can give better insight into how overlapping faults interact through inversion.

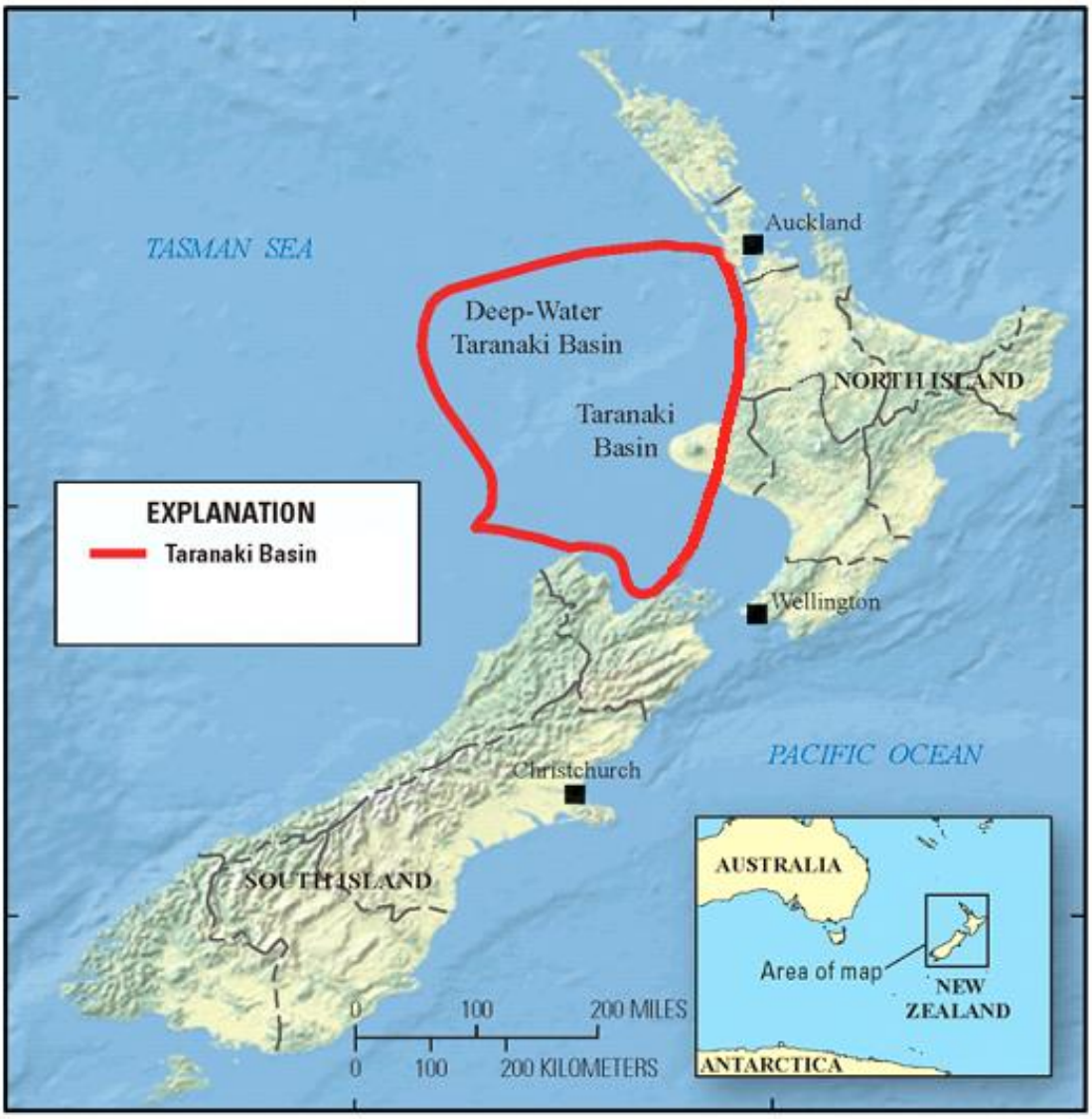

Figure 1. Location of the Taranaki Basin of New Zealand outlined in red. Modified from Wandrey (2013)

1.2 Structure of the Southern Taranaki Basin

The structure of the Southern Taranaki Basin is characterized by North to Northeast trending basement-involved normal and reverse faults. The location of the primary faults and their type are shown in Figure 2. Figure 3 shows two schematic cross sections across the basin. The eastern side of the basin is bounded by large subduction-related back thrusts. Late Cretaceous-age basement involved normal faults are distrusted across the basement. The normal faults trend North to Northeast and dip to both the East and West. Displacement on these faults varies from hundreds of meters to kilometers.

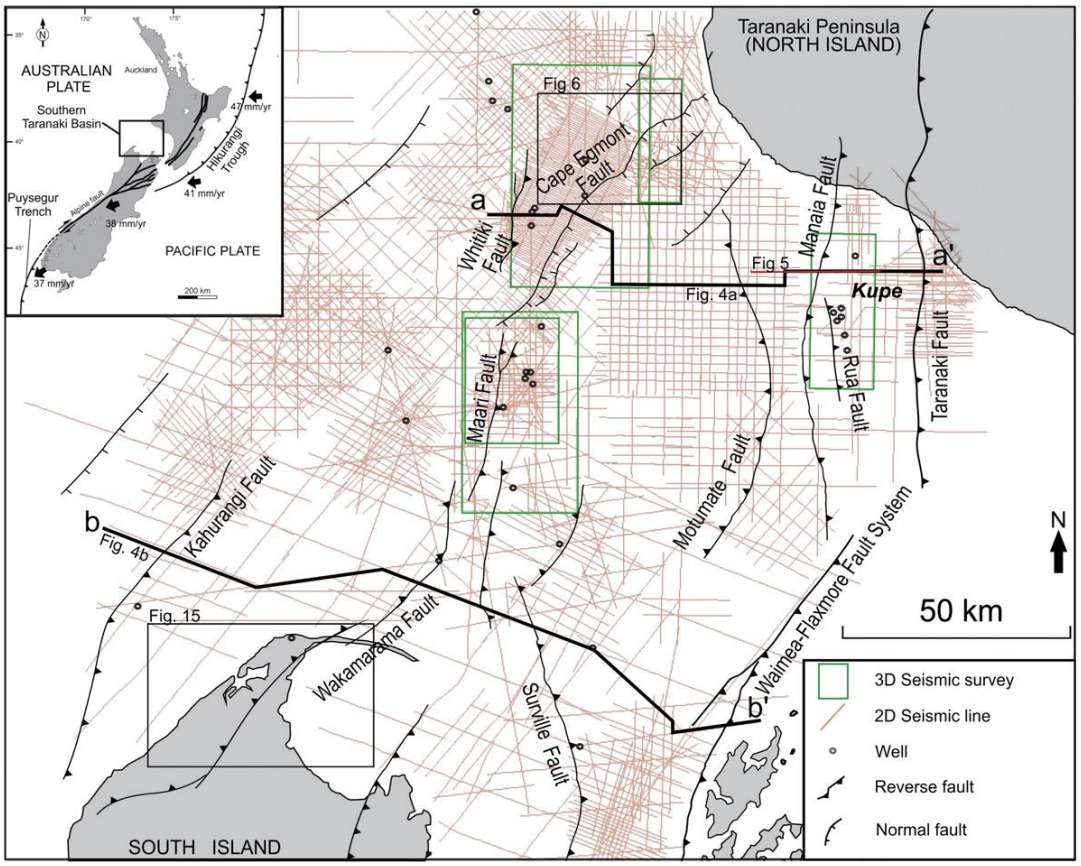

Figure 2. Location of large scale faults and data available for interpretation. (Reilly, 2015)

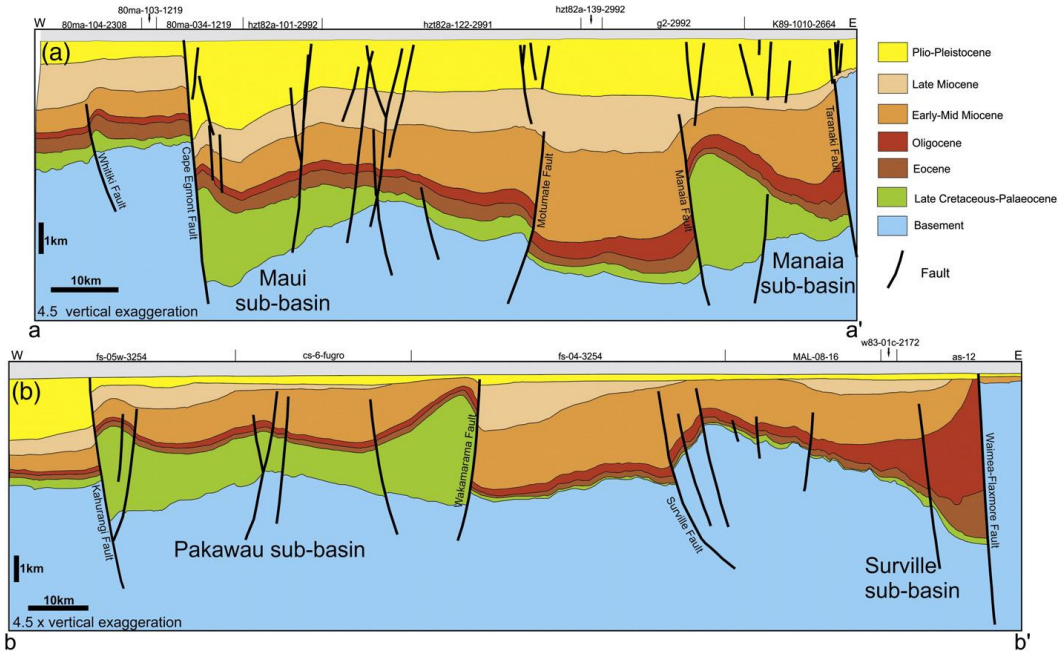

Figure 3. Schematic cross sections showing the general structures found in the Southern Taranaki Basin. Reverse faults, normal faults, and inversion structures are present. The faults with hanging wall thickening of the green Cretaceous units are indicative of inversion. (Reilly, 2015)

Many normal faults have been compressionally reactivated in the eastern and central part of the basin resulting in inversion structures. The reactivated compressional faults generally have high dips and dip to either the East or West. These faults are believed to have a deep crustal detachment in the brittle-ductile transition. They are generally associated with asymmetric fault cored anticlines.

The basic concept of inversion on a concave-upward listric fault is illustrated in figure 4. Early extension results in the formation of rollover structures with the syngrowth units thickening in the hanging wall. The thickness changes reach their maximum value adjacent to the fault. Later compression results in these faults being reactivated as reverse faults. Syngrowth units deposited during the compressional phase typically exhibit thinning of hanging wall units adjacent to the fault. Two characteristic

features of inversion are (1) the presence of thicker hanging wall units in the uplifted block; and (2) changes in separation patterns of faults from normal separation in the deeper units to reverse separation in the shallower units. These two characteristic features can be used to effectively identify inversion. Some of the faults in this area showing compressional displacement exhibit no hanging wall thickening of units suggesting pure compression without inversion.

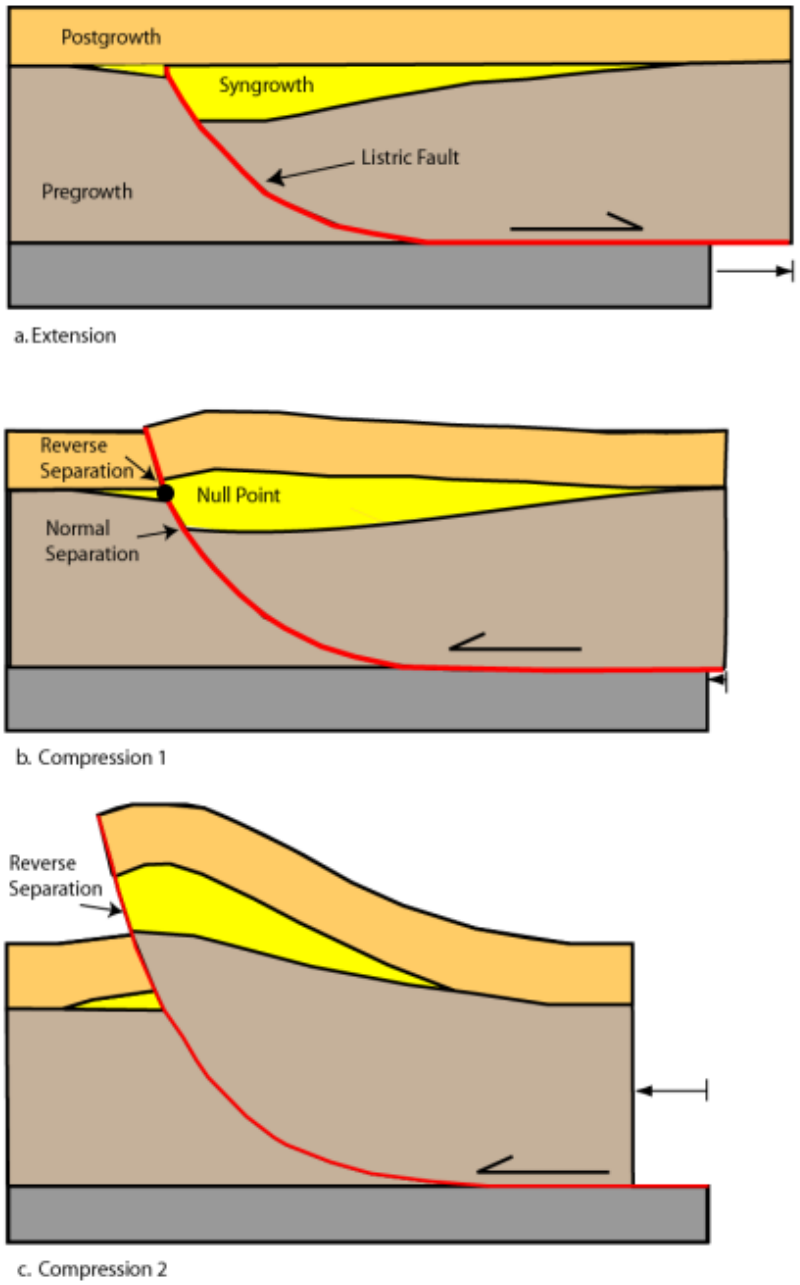

Figure 4. Basic concept of inversion on a concave-upward listric fault. The top figure shows the resulting bed geometries of pregrowth, syngrowth, and postgrowth units during extension. The second image shows the compressional reactivation of the fault. Compressional reactivation causes reverse offset of hanging wall thickening units. It also causes both reverse and normal offsets along the fault separated by the null point which is the location with no apparent offset. The final image shows how further compression could result in no apparent normal offset.

1.3 Stratigraphy of the Southern Taranaki Basin

The general stratigraphy of the Southern Taranaki Basin is shown in Figure 5 with producing reservoirs and the associated wells shown. The wells located in the Kupe area are indicated on the figure with a gray box. The lithostratigraphic formations associated with the initial extensional phase are the basal Rakopi, North Cape, and Farewell. The sediments are believed to have been sourced from the surrounding relatively uplifted basement. The Rakopi formation is believed to be dominantly terrestrial sediments and the primary source rock for the area. The North Cape formation is a shore face facies in the west and transitions to terrestrial facies in the Kupe area to the east. There is no well data for these units in the Kupe area and the understanding of these units is based on surrounding well data and outcrops on the north island of New Zealand. The final unit deposited in the extensional phase is the Farewell formation. This is the reservoir for the Kupe South Field and is composed of terrestrial and marginal marine facies.

The Eocene units in the Kupe area are thin and pinch out to the south. The Kaimiro unconformably overlies the Farewell formation and the Mangahewa unconformably overlies the Kaimiro. These units are composed of terrestrial facies.

The Otaroa Formation is the first unit deposited during compression. The base of the Otaroa Formation is the Matapo Member which is a thin shore face sand. The Matapo Member is the reservoir interval in the Toru well. The rest of the Otaroa Formation is dominantly shaley marine facies. The overlying Taimana, Manganui, and Urenui Formations are also shaley marine facies but generally coarsen upward. Some isolated turbidite sands can be found in these units. These units are capped by an erosional unconformity.

The Pliocene to present units consist of the basal Matemateaonga, the Tangahoe, and Whenuakura. The Matemateaonga is a shore face sand and the overlying Tangahoe and Whenuakura are a series of prograding shelf facies.

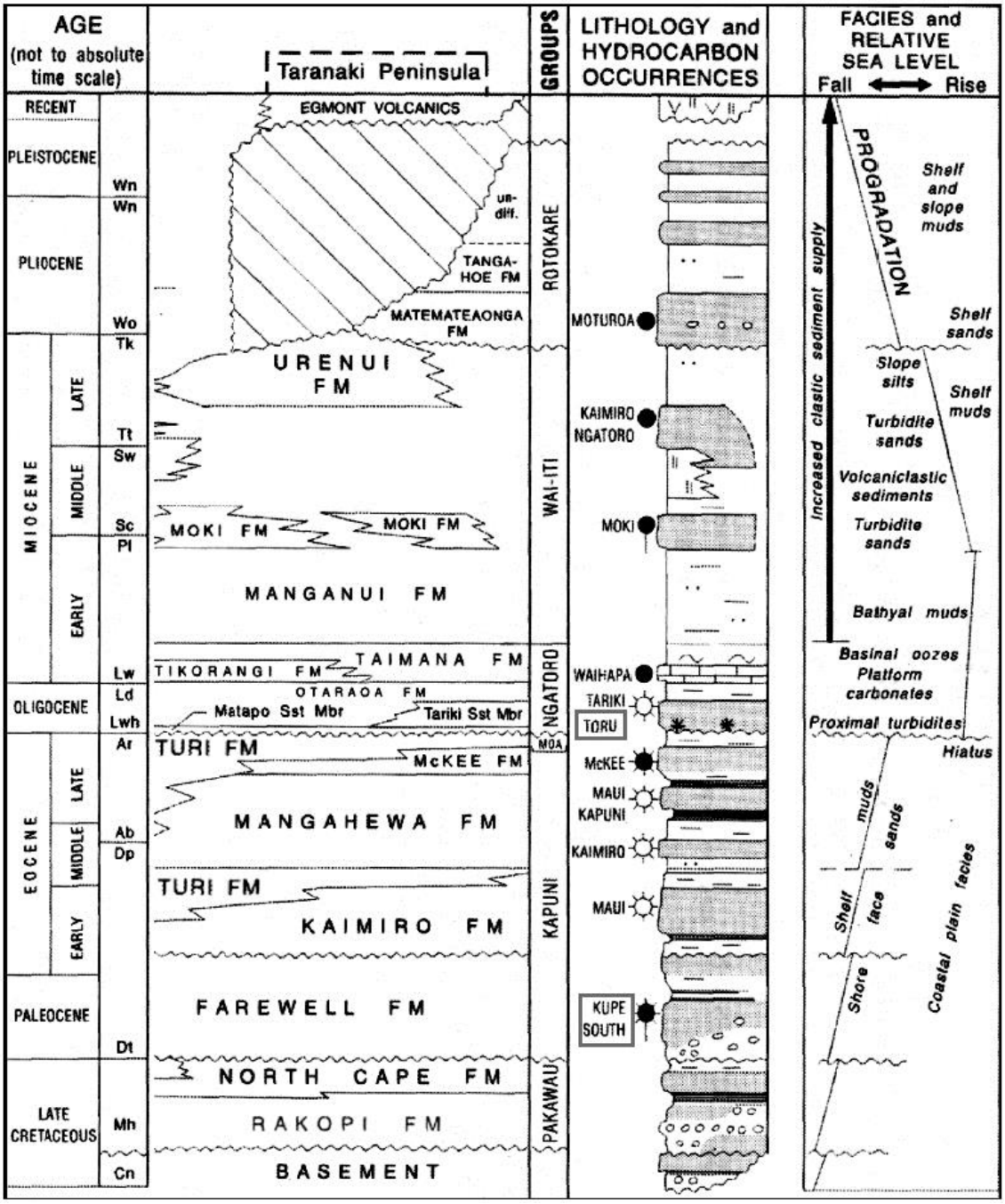

Figure 5. General stratigraphy of the Southern Taranaki Basin with ages and relative sea level. Known oil and gas reservoir units within the Taranaki basin are shown with grey boxes to signify the wells located within the Kupe area. Modified from King and Thrasher (1996).

1.4 Geologic History of the Southern Taranaki Basin

The Taranaki Basin formed during a period of extension during the Late Cretaceous to the end of the Paleocene. This extension is associated with the breakup of Gondwana and seafloor spreading in the Tasman sea. North to Northeast striking basement involved normal faults created small (10-50km by 50-150km) half grabens. Sedimentation during this period was primarily preserved in the half grabens. This was followed by a period of tectonic and depositional quiescence during the Eocene.

A compressional phase during the early Oligocene to the late Miocene reactivated some of the existing normal faults creating inversion structures. The compressional phase is associated with subduction of the Pacific plate to the east of the Taranaki Basin. It is believed that the rate of convergence slowed in the late Miocene causing slab roll back resulting in the end of compression in the basin (King and Thrasher, 1996).

From the Late Miocene to present the basin has undergone little tectonic deformation although some normal faults are present in these units. These units primarily detach in the late Miocene units which suggests the extension is related to gravity sliding and differential compaction. The location of the underlying basement involved faults strongly influences the geometry of these faults.

1.5 Data Used

The data used in this study is available to the public through New Zealand Petroleum and Minerals(NZP&M). The Kerry 3D dataset and 7 wells were used for seismic interpretation. Several previous studies were used to establish the tectonic framework. Maps produced from a regional study were used to extend horizons beyond the 3D dataset and to check the accuracy of the depth conversion (Fohrmann, 2012). These extended horizons were produced using the additional 2D seismic lines which can be seen in figure 6. Table 1 shows the wells which have been drilled in the area to date with the wells used for this study indicated. The data from the more recent wells were not available for this study.

Table 1. Wells within the study area, the wells used in the study are indicated.

Used	Name	Year	Total Depth (m)	Content	Status
X	Kupe-1	1975	3682	gas shows	plugged and abandoned
X	Kupe South-1	1986	3503	oil/gas	suspended
X	Kupe South-2	1987	3250	oil/gas	suspended
X	Kupe South-3B	1988	3447	shows	suspended
X	Kupe South-4	1989	3800	shows	plugged and abandoned
X	Toru-1	1990	4150.8	gas/condensate	suspended
X	Kupe South-5	1990	3200	oil	suspended
	Kupe South-6	2007	3385	gas/condensate	producing
	Kupe South-7	2007	3454	dry	plugged and abandoned
	Kupe South-8	2007	3834	gas/condensate	producing
	Momoho-1	2008	3145	gas/condensate	plugged and abandoned
	Kupe South-7ST1	2008	3503	gas/condensate	producing

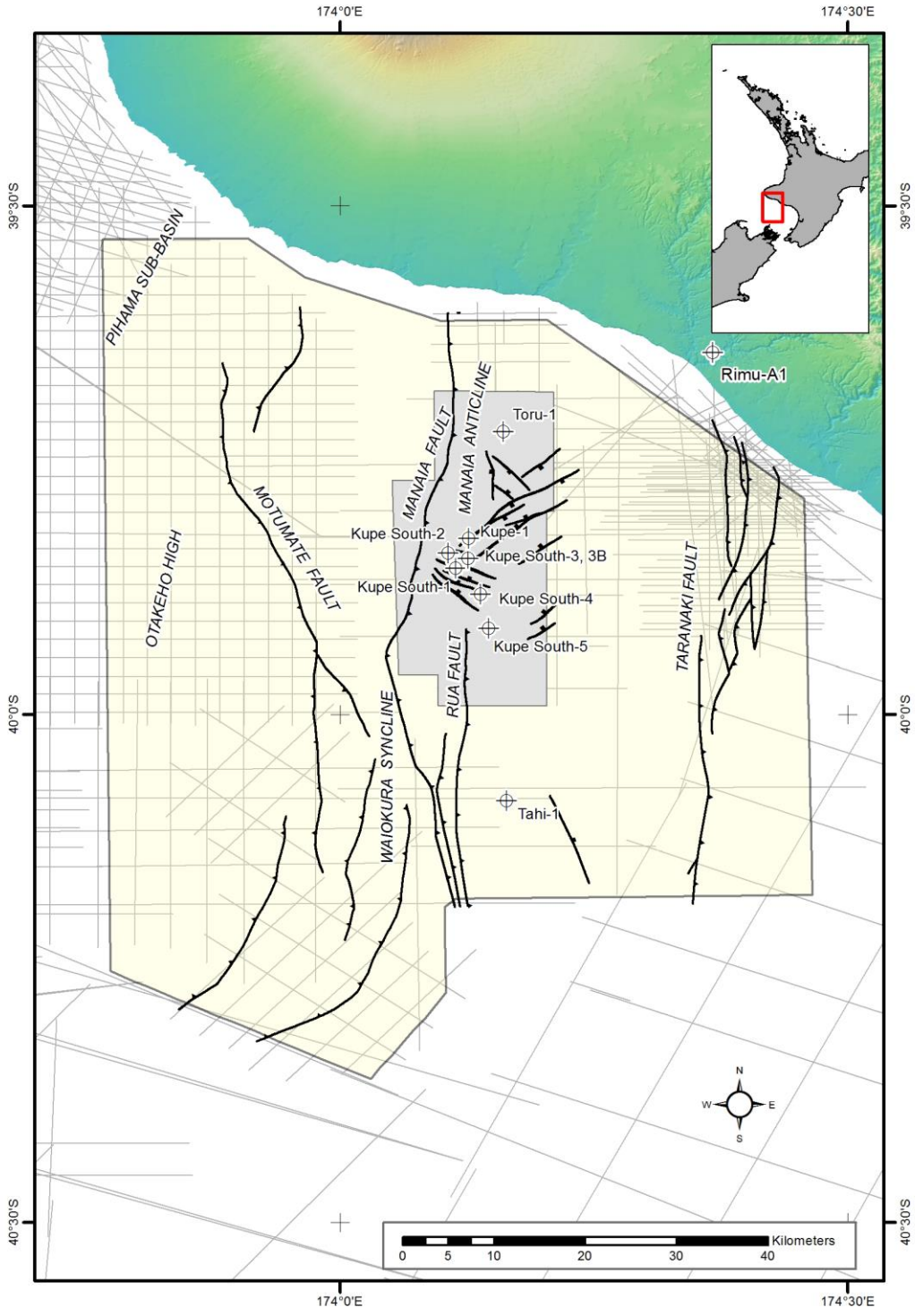

Figure 6. The data used by Fohrmann (2012) to produce regional maps. The Kerry 3D dataset is shown in gray with gray lines indicating the location of 2D seismic lines. Significant faults within the area as well as oil wells are also shown.

The Kerry 3D seismic survey was shot between February and April 1996 and was re-processed between 2004 and 2005. The survey covers an area of approximately 410 square kilometers. The acquisition parameters for the Kerry 3D survey are shown in Table 2. The Kerry 3D seismic survey was provided in time.

Table 2. Acquisition parameters of the Kerry 3D survey. Modified from CGG Australia Services Pty Ltd, 2004.

Energy Source	
Array Type	Bolt Airgun array
Total Volume	3397 cu.in per source
Air Pressure	2000psi
Shooting Mode	Flip-flop
Gun Depth	7.0m
Shotpoint Interval between alternate guns	18.75m
Centre Source separation	37.5m
Streamers	
Type of Streamer	HSSL/Nessie2, Digital
Hydrophones per group	24
Number of Streamers	4
Number of Groups per Streamer	304
Recording Channels (System A)	608 (2 x 304)
Recording Channels (System B)	608 (2 x 304)
Group Interval	12.5m
Group Length	16.15m
Steamer Depth	7.0m
Streamer Length	3800m
Streamer Separation	100m
Near Offsets	180 – 220m
Recording	
Recording system	2 x GDR-1000 SW.3.52
Tape format	SEG-D 8015
Filters	Low Cut – 3Hz/18dB
High Cut	180Hz/70dB
Record length	5000ms
Sample interval	2ms

Chapter 2: Method

2.1 Seismic Horizon Interpretation

Thirteen seismic horizons were interpreted using the guidelines found in Bull et al. (2015). The seismic parameters used to pick each horizon can be found in Table 3. The approximate age and formation correlation are shown in Figure 7. A regional naming convention was outlined for this area by Roncaglia et al (2010) and suggests naming seismic horizons using a letter to represent the age period followed by a number which increases from oldest to youngest. This naming convention has been widely adopted so it will be used in this study. Oil and gas production in the model area is from the Matapo Member and the Farewell formation which correspond to the base of the N05 interval and the P10 interval respectively.

The seismic interpretation of the footwall of the Manaia fault has a high degree of uncertainty because of a lack of well control and no seismic continuity across the fault. Regional cross sections were used to estimate the location of these horizons. The P22 and P10 horizons likely have some thickness in the footwall based on regional correlation but the exact thickness of each cannot be determined from seismic data alone.

The basement horizon has a seismic depth of 3 to 5+ seconds in the Kerry 3D seismic dataset. The basement horizon in the hanging wall of the Manaia fault deepens to the North and is below the recorded depth of Kerry 3D seismic dataset of ~5 seconds. The depth was approximated using published 2D lines with longer recording times. The basement horizon is notably poorly imaged between the Manaia and Rua faults. The seismic interpretation in this area is approximate at best.

The K96 through P10 horizons were deposited during the initial basin forming extensional event. The K96 and P00 horizons were deposited entirely in the hanging wall of the Manaia fault. These units are generally well imaged away from the two primary faults but are sometimes distorted near the fault.

The N05 through N44 horizons show apparent compressional deformation. These units generally thicken away from the crest of the anticline and thicken in the footwall. The N44 horizon is the last interpreted horizon showing apparent compressional deformation. The N44 horizon was eroded by the overlying N50 horizon in the southern part of the area. The N50 through N82 horizons are nearly horizontal and are well imaged.

A suite of seismic attributes was generated to try and better interpret the Manaia and Rua faults. Attributes used include coherency, similarity, curvature, Sobel filtering, and a range of co-rendered attributes. The attributes image faults in the upper units well but no attribute was found which improved interpretation of the deeper Manaia or Rua faults. The greatest improvement found was using a lowpass filter to remove high frequency multiples from the seismic data. This noise appears as horizontal lines cutting across the seismic in time and has a center frequency of ~ 40 Hz. A low pass filter with a pass of 20 Hz and a cut of 30 Hz was used. The improvement in data quality below ~1.5 s can be seen in figure 8. The filtering is especially helpful when trying to determine the bed and fault intersection of dipping units, where the horizontal noise creates an artificial breakup of the otherwise continuous reflectors making it harder to distinguish the end of the reflector.

Table 3. Seismic horizons interpreted with their approximate lithostratigraphic formation and reflector type picked.

Seismic Surface	Approximate Lithostratigraphic Formation	Boundary Type	Reflector Type (SEG reverse)
N82	Whenuakura	Erosional	Peak
N75	Tangahoe	Conformable	Peak
N68	Matemateaonga	Conformable	Trough
N50	Manganui	Erosional	Peak
N44	Manganui	Conformable	Trough
N34	Manganui	Conformable	Trough
N15	Taimana	Conformable	Trough
N05	Taimana	Conformable	Peak
P22	Kaimiro	Erosional	Peak
P10	Farewell	Erosional	Peak
P00	North Cape	Conformable?	Peak
K96	Rakopi	Conformable?	Trough
Basement	Basement	Erosional?	Peak

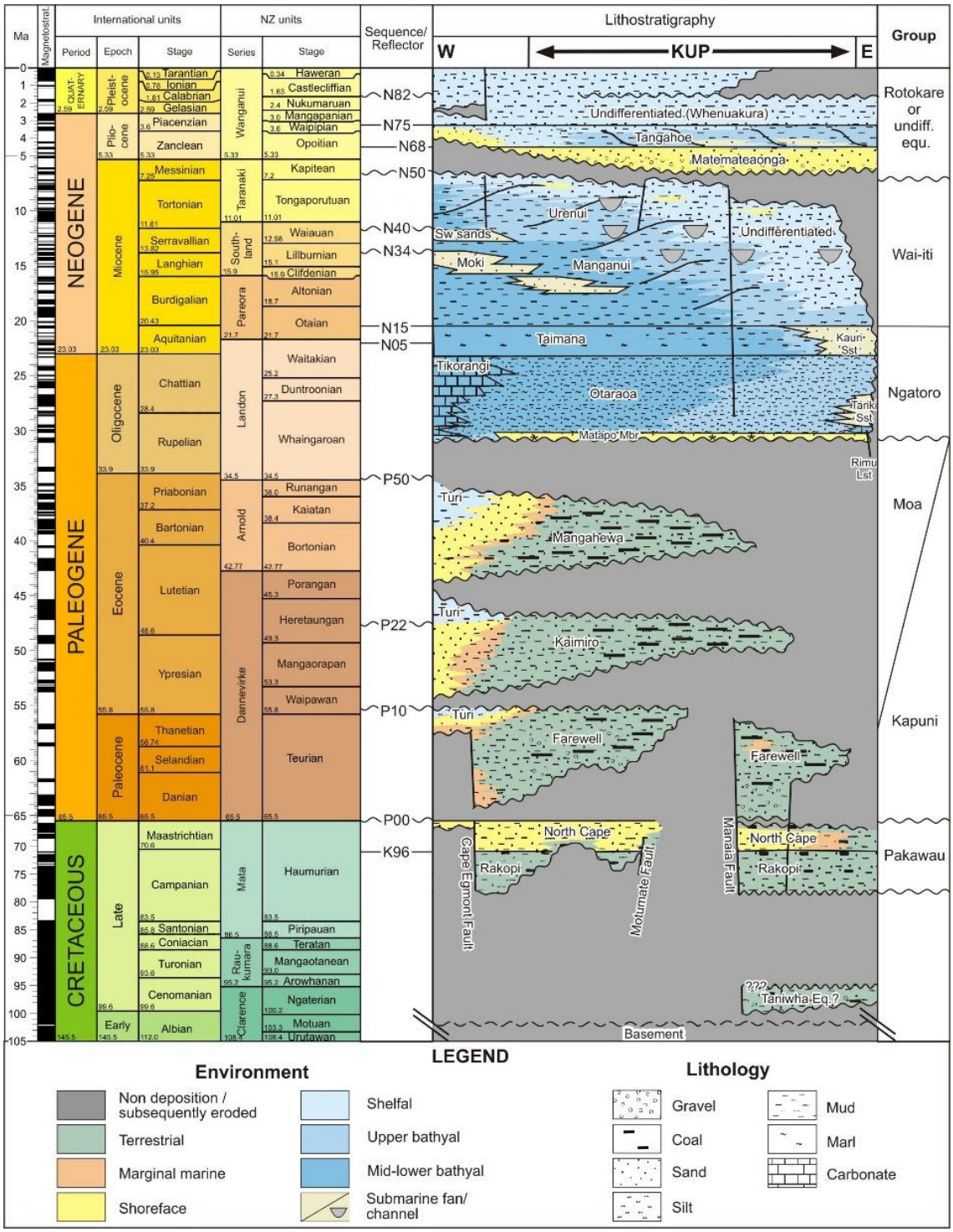

Figure 7. Stratigraphy of the Kupe area with ages. The seismic horizons are shown in the center of the figure. Modified from Fohrmann (2013) using units from Bull (2015).

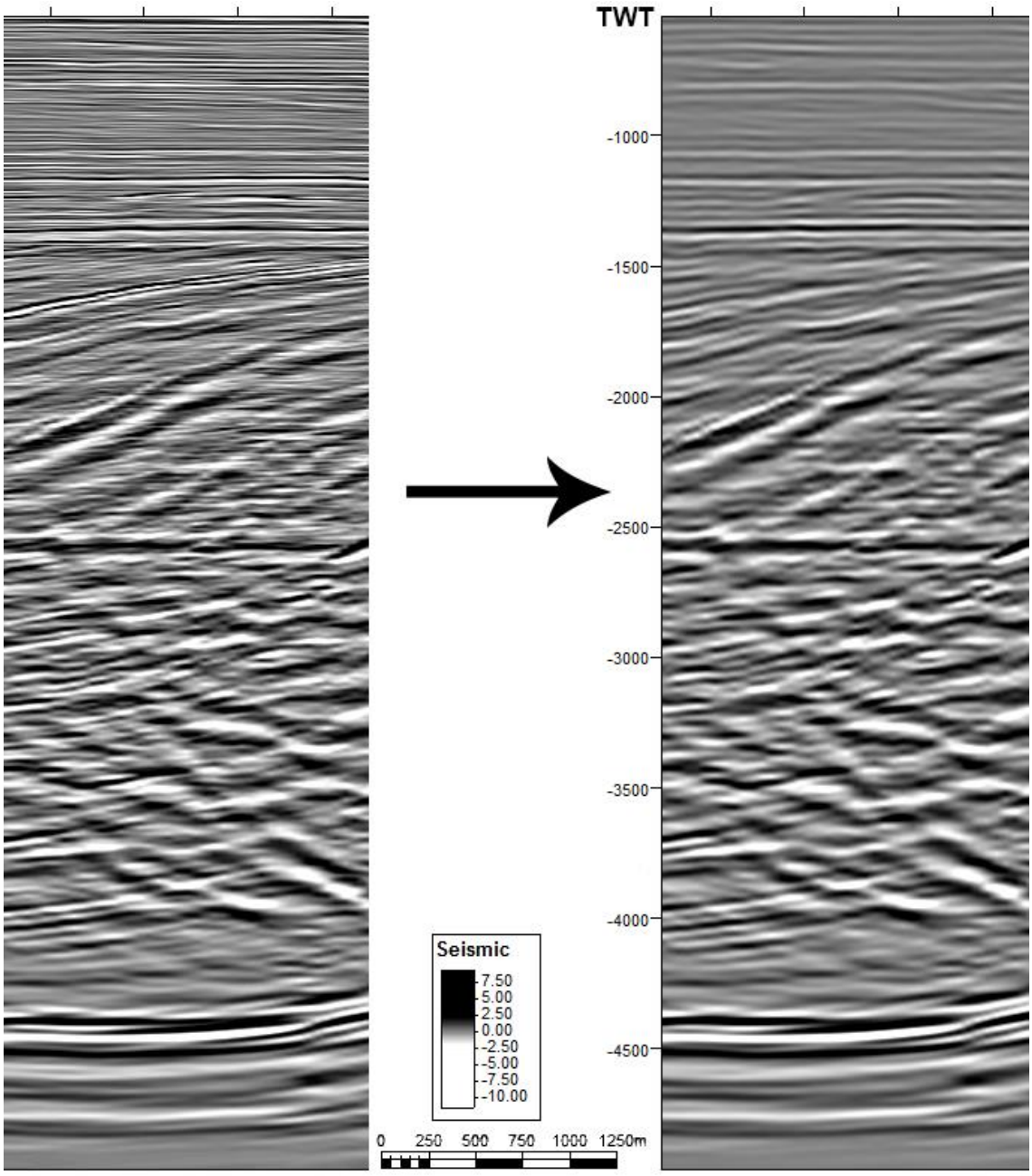

Figure 8. The left side shows the original Kerry3D data and the right shows the seismic after applying a low pass filter to suppress high frequency multiples.

2.2 Structural Interpretation and Depth Conversion

This study is focused on characterizing the geometry and kinematics of the Manaia and Rua faults. These faults are basement involved and have several kilometers of displacement on them. Imaging the faults in time distorts the geometry because of the significant change in seismic velocity with depth. To understand the geometry of these faults the seismic data and interpretation must first be converted to depth from time.

Seven wells were used for this project and they were approximately tied to the seismic using a time depth curve available from GNS Science. Synthetic seismic traces were generated for the wells to validate the time-depth relationship. The wells used seen in Figure 6 are located along the crest of the anticline leaving the footwall of the Manaia fault and the back limb with no well control.

The seismic horizons on which the interpretation is based have been used to create a basin wide depth conversion by GNS Science. Although that velocity model is not publicly available, some associated products are. The velocity model created for this study is largely based on the data available from Hill and Milner (2012). Selected horizon depth maps are available from the GNS Science velocity modeling project and they were used to check the validity of the velocity model created for this project.

The velocity model was created using the advanced velocity model module within the Petrel software suite. Velocity data were extracted from the wells in the dataset and used to create a varying velocity value across the dataset for each horizon. The velocity model used the equation $V=V_0+K*(Z-Z_0)$ with V_0 and K set from the well time depth relationship for each horizon with well velocity data and using V=1500m/s for the sea water interval. The P00, K96, and basement horizons are not intercepted by

any wells in the dataset and were modeled using the values of the overlying P10 interval with a set velocity of 4500m/s below basement. The velocity parameters used gave a reasonable fit with published data.

The velocities in the footwall of the Manaia fault likely differ significantly from the hanging wall but there is no well control to provide a more accurate estimate. The lack of available velocities below the P10 horizon and in the footwall of the Manaia fault have created a wide variety of published velocity models for this area. The modeled depth for horizons varies in publications up to 2km or more (Hill et al., 2013). The depth model used in this study most closely matches that of Hill and Milner (2012) which used velocity data from more recently drilled wells and attempted to account for the change in footwall velocities.

One problem with the velocity model is the overlapping of units across the Manaia and Rua faults. The velocity modeling method used uses horizons covering the entire model area with velocities assigned to the horizon. These horizons cannot account for overlapping of a single unit because only one depth can be assigned to a surface at each x/y location. The hanging wall velocities were used to reflect the greater available data in the hanging wall.

2.3 Fault Modeling Theory

The goal of fault modeling is to provide insight into the geometry of units and faults in areas of poor data using areas of good data. Figure 9 shows how different interpretations within areas with poor data can greatly change the geometry of poorly imaged beds and faults. Fault modeling takes a logical approach to try and best predict the true geometry.

A combination of two techniques was used to model the fault geometries. Inclined shear fault modeling was used to model the component of deformation accounted for by fault bend folding and equal area balancing was used to account for fault propagation folding and fault-independent folding. Inclined shear restoration has been shown to reasonably model fault bend folding along listric faults (Dula,1991).

Inclined shear fault modeling assumes that heave along a fault is constant and that deformation is accommodated through simple shear along parallel planes. This means that the geometry of a bed after deformation is directly related to the geometry of any faults below it along the shear plane. The angle between the shear plane and the plane perpendicular to the original bed geometry is referred to as the shear angle. Experimental work and real-world examples have shown that shear angle values are typically between 20 and 40 degrees (Dula, 1991).

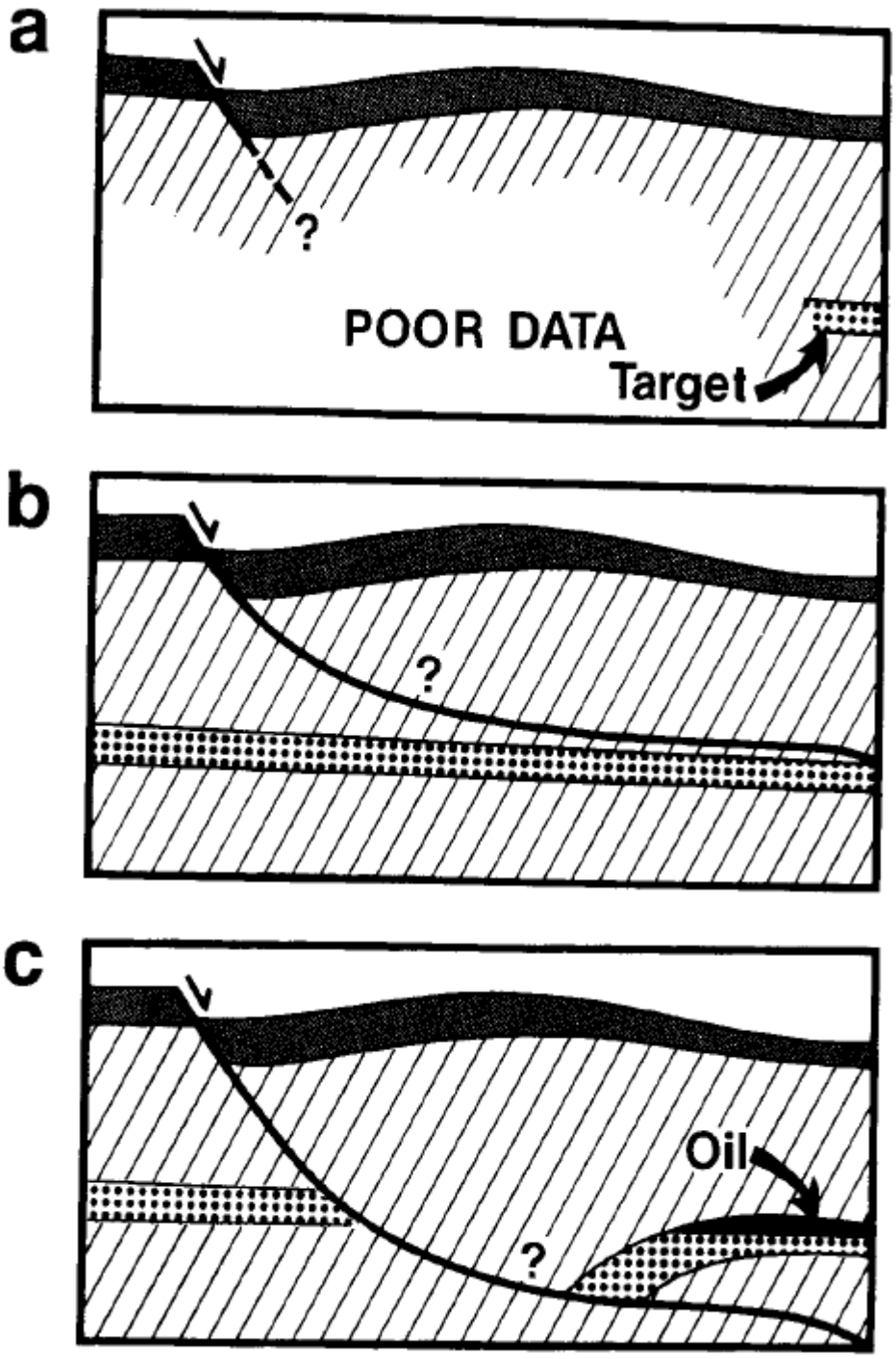

Figure 9. Idealized representation of the goals of fault modeling. Image A shows how some beds may be well imaged while others are poorly imaged. Image B and C show how different interpretations would suggest different geometries at depth. (Dula, 1991)

Modeling a fault using inclined shear requires the modeler to define a bed geometry, shear angle, amount of extension or compression, and the initial bed geometry. The amount of extension or compression parameter is typically found by locating the hanging wall and footwall bed intersections and measuring the horizontal distance between shear planes which intersect those points. The initial bed geometry is typically assumed to be a horizontal plain at the footwall bed level.

There are several ways to estimate the shear angle. One approach is to use the angle of subsidiary faults. This approach does not work in the study area because there is no consistent subsidiary fault angle. Another approach is to determine the shear angle assuming the depth of the detachment. The detachment depth is not known in the study area so this method was not used. If the upper part of a fault is well imaged the shear angle can be determined by finding the angle which matches observations. The observed additional component of folding in the upper beds in this area makes this technique unusable. Coulomb theory predicts a shear angle of 20 to 25 degrees for a concave upward listric fault (Xiao, 1990) like the one in the study area and so a shear angle of 20 degrees was used.

Once the observational parameters have been set the fault can be modeled as shown in Figure 10. Figure 10 shows a bed with compressional deformation in red and a bed with extensional deformation in blue with equal but opposite horizontal displacement parameters. Any point along the horizon is assumed to have been translated along a vector parallel to the fault relative to the shear angle. The manual procedure to model the fault from a bed starts by defining the original position of the

bed as shown by the dashed horizontal line AB in Figure 10. Next a line that is perpendicular to the regional level line is drawn to connect the regional level with the hanging wall bed and fault intersection shown as lines CD. Then a line which is rotated from line CD by the shear angle α is projected to the regional level shown as line DE. A series of construction lines parallel to line DE are then drawn spaced according to the horizontal displacement parameter shown as E' in extension and C' in compression. Then a line connecting the intersection of the construction lines and the original level line is drawn to the intersection of the next construction line and the observed bed level in the direction of deformation. These lines are shown with an associated number in figure 10. The numbered lines are then projected downward along the inclined shear lines so that they connect with the observed fault location or a previous line. This creates the modeled fault geometry.

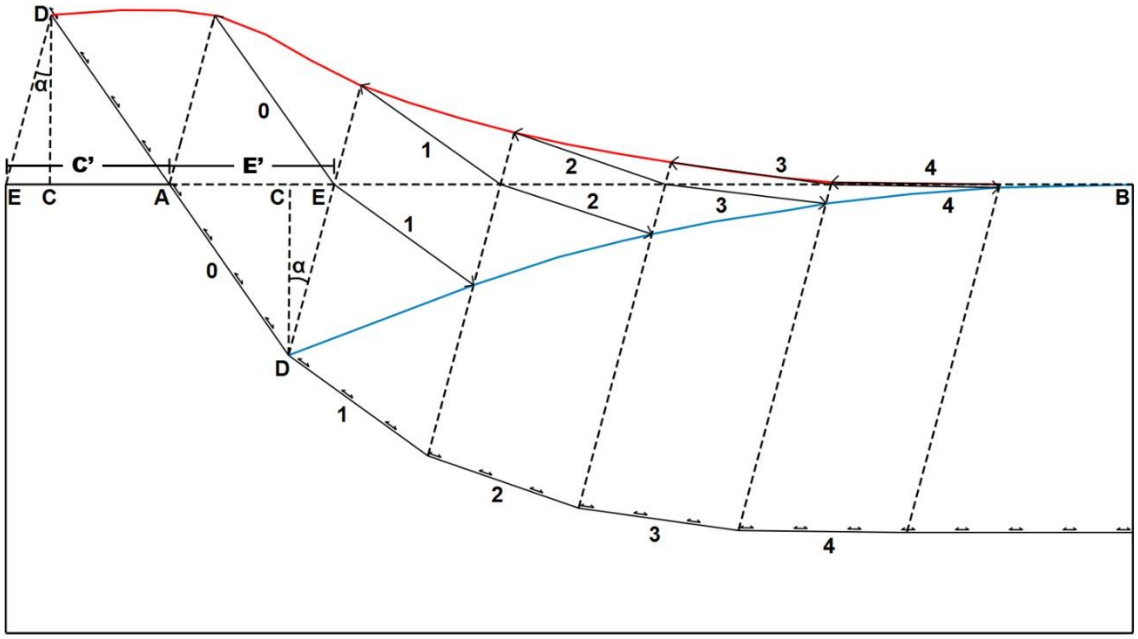

Figure 10. Geometric construction for modeling a fault using inclined shear. The fault can be modeled using the red bed with apparent reverse offset of the blue bed with apparent normal offset. The parameters needed are the apparent horizontal extension (E') or apparent horizontal compression (C'), the shear angle (α), and a deformed bed geometry.

Inclined shear is a simplification of reality. The shear angle is likely to change along the trend of any fault and the shear angle used is attempting to find an average. Another potential problem is that according to Coulomb theory the shear angle direction is determined by the direction of curvature of the fault. In figure 10 the shear angle is rotated clockwise because the curvature of the fault is concave upward. If the same fault were concave downward the shear angle would be rotated counterclockwise based on coulomb theory. A change in curvature direction is observed on the Manaia fault in the upper part of the fault in some places along trend. The same direction of shear angle was used to model this part of the fault because it is only a small part of the larger structure. It is also possible that the average shear angle is maintained in this area

because of reactivation of the existing shear fractures associated with the extensional phase.

Fault propagation or fault-independent folding is needed to account for several observations within the model area. The first evidence of fault propagation folding is the youngest compressionally deformed beds which are not broken by the fault. Pure inclined shear deformation assumes constant heave along a fault. If heave is maintained along a fault the fault must continue to the surface and any laterally continuous beds deformed by a fault must be cut by that fault.

The second observation which is inconsistent with pure fault bend folding is the steeply dipping front limb. Figure 11 shows the geometry of a bed after extension or compression along a listric fault using inclined shear to model the bed. As shown in the figure, a listric fault that has undergone compressional deformation will produce gently to horizontal dipping beds in the hanging wall against the fault. In pure inclined shear, a sharp change in bed dip would have to reflect an equally sharp change in the fault dip. A sharp change in fault dip is not mechanically advantageous and so the sharp changes in dip are better explained with a different mechanism.

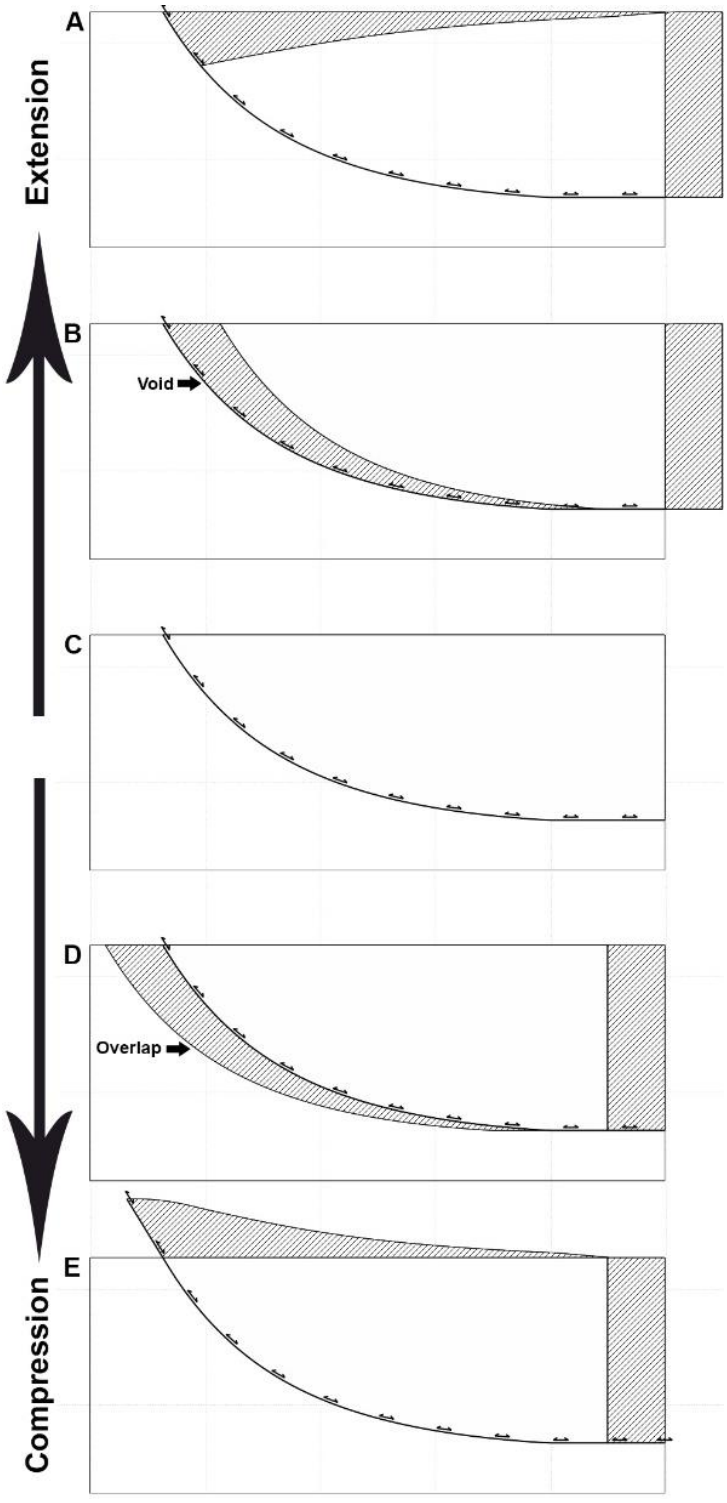

Figure 11. Inclined shear theoretical geometry after compression or extension. The grey hashed polygons indicate the areas which are in balance after deformation. In compression, the area of uplift is equal to the area which would overlap with horizontal translation. In extension, the area of subsidence is equal to the area below the fault block with horizontal translation.

The third evidence of fault propagation folding is the geometry of beds near or at the null point of the fault. The null point along an inverted fault is the point at which beds show no apparent offset. In a positive inversion structure, the beds above the null point exhibit reverse offset and the beds below exhibit normal offset. The bed shown in figure 12 is near the null point of the fault and so if inclined shear was the only deformation mechanism the bed should be horizontal. The bed has a distinct downward flexure near the fault followed by an upward flexure before returning to a nearly horizontal and constant dip away from the fault. The bed dip away from the fault was extended as shown by the dotted line in figure 12. The area above and below extended ling to the observed position are in near area balance. This form of fault propagation has been observed in other inversion structures (Mitra 2005).

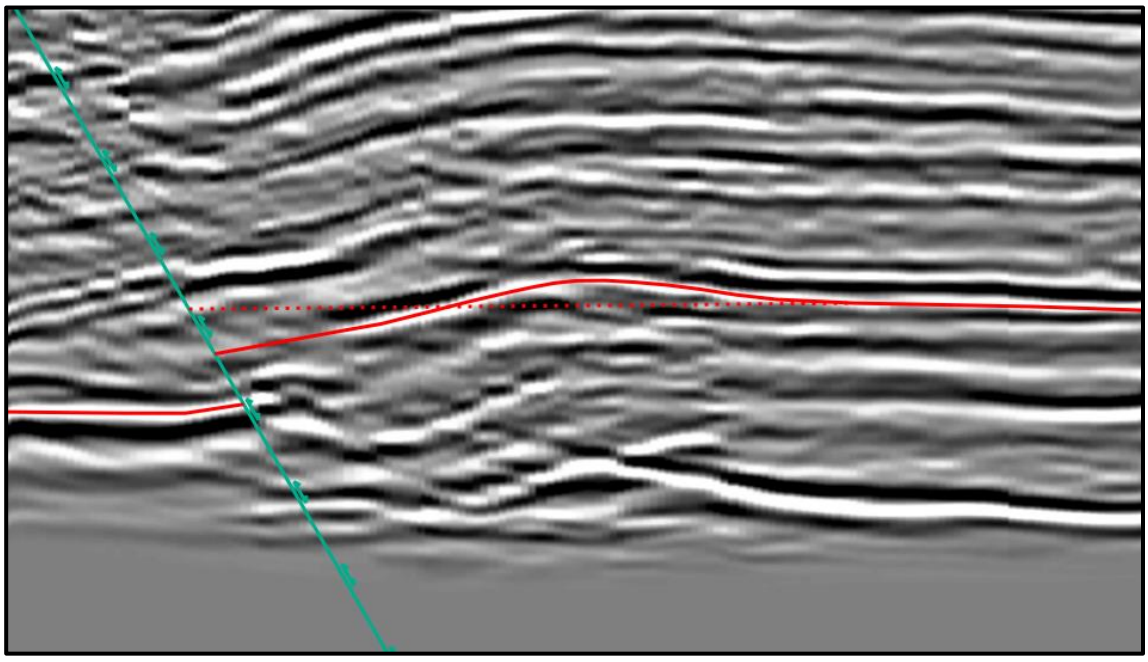

Figure 12. Observed null point bed geometry. The red dashed line is an extension of the back-limb dip. The area above and below the line is in near area balance.

2.4 Manaia Fault Modeling Method

A workflow was developed to use inclined shear fault modeling and account for the observed fault propagation. One key assumption used in this workflow is that the maximum dip of the fault is around 60 degrees. This is assumed because faults with dips greater than 60 degrees are not mechanically advantageous to reactivate in compression. For steeper dips it is more likely for a new fault to breakout with a lower dip.

The fault modeling procedure starts with seismic interpretation of the bed geometry and the intersection of the bed with the fault in the hanging wall and footwall. Next the fault is drawn to connect the hanging wall and footwall bed intersection. The fault is then drawn in at 60 degrees below the bed footwall fault intersection and extended above the hanging wall bed intersection at an angle equal to the interpreted geometry or modified to fit the observed fault location depending on the seismic quality.

A template bed is forward modelled from the initial position of the bed using inclined shear with a shear angle of 20 degrees. The horizontal displacement is set so that the area above and below the modeled template bed to the observed bed are in area balance as shown in Figure 13. The horizontal displacement parameter for the template bed is then used for inclined shear modeling of the remainder of the fault as shown in figure 14.

The workflow is then repeated for a series of cross sections across the model area. For this study, a series of ten equally spaced cross sections was created with nine additional cross sections in the Kupe oil field area. The interpreted geometries are then

compared in 3D and checked for compatibility. The process is then repeated to correct for 3D discrepancies.

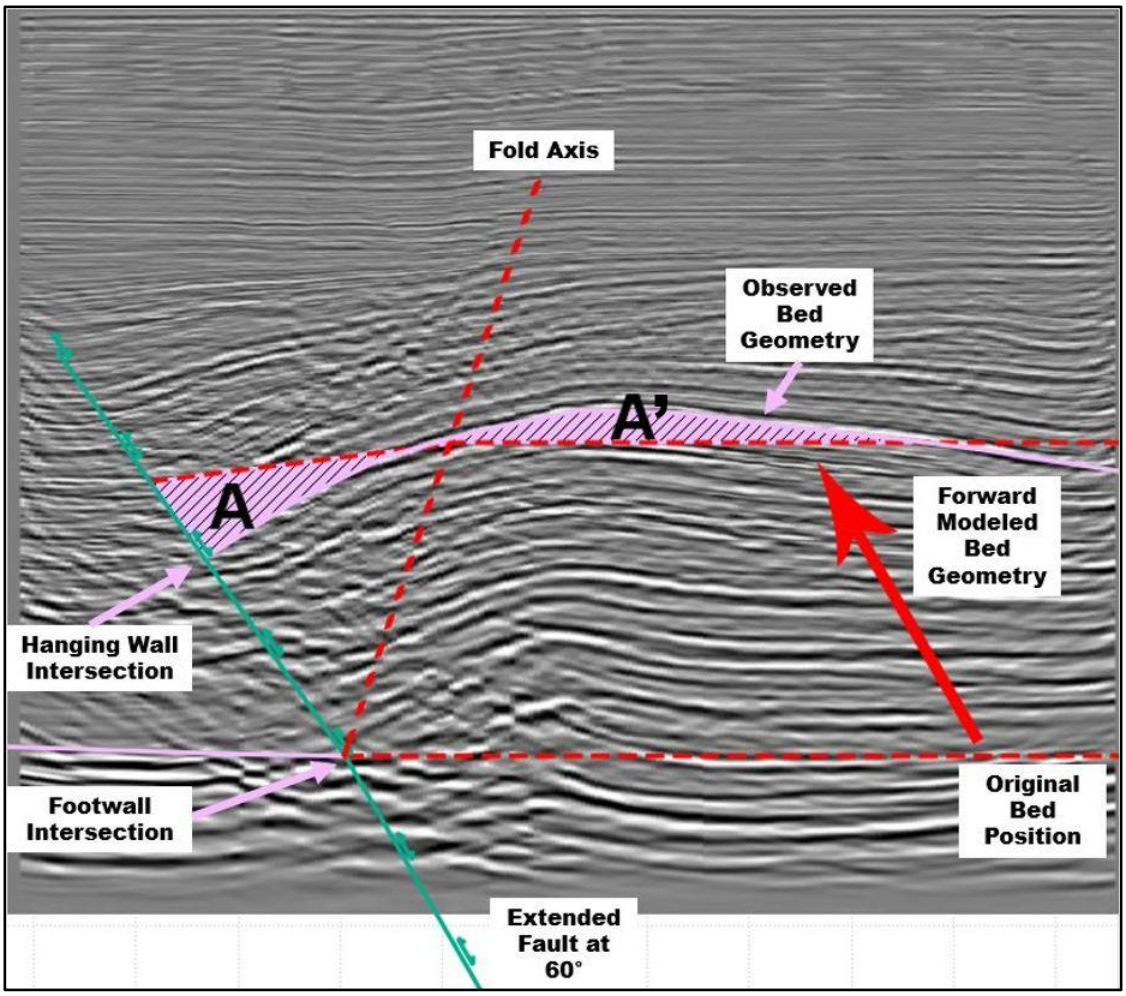

Figure 13. The workflow used to area balance the structure. After establishing the location of the fault using seismic interpretation of the hanging wall and footwall fault intersections the fault is extended below at 60 degrees. The hanging wall bed is then forward modeled from the original position such that the area above (A') and below (A) the observed bed geometry to the modeled bed are in area balance. This gives the horizontal compression parameter used for inclined shear modeling.

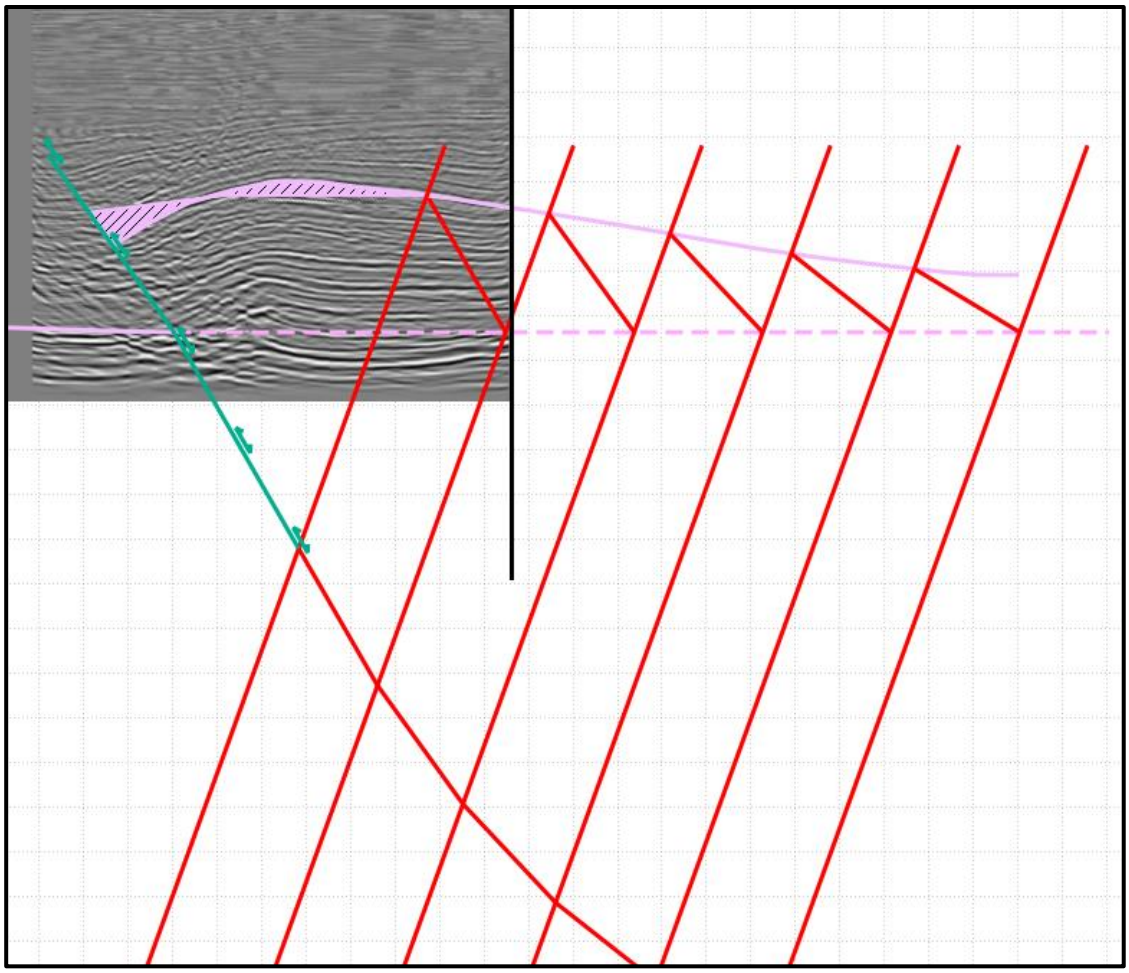

Figure 14. After the horizontal compression parameter is set by area balancing, the inclined shear method is used to model the fault. In this figure, the bed is extended beyond the available seismic data to model the fault to a greater depth.

2.5 Rua Fault Modeling Method

Modeling the Rua fault requires additional steps because it is in the hanging wall of the Manaia fault and has been deformed by the Manaia fault. Points in the hanging wall of the Rua fault have been translated along a vector which is not parallel to the Manaia or Rua faults. This vector is constructed from two vectors with one parallel to the Rua fault and one parallel to the Manaia fault with lengths proportional to the horizontal displacement on each fault. Figure 15 shows how a point at location A would move to its final position at point C. Line AB represents the movement from the Manaia fault and line BC represents the movement from the Rua fault resulting in the combined vector AC.

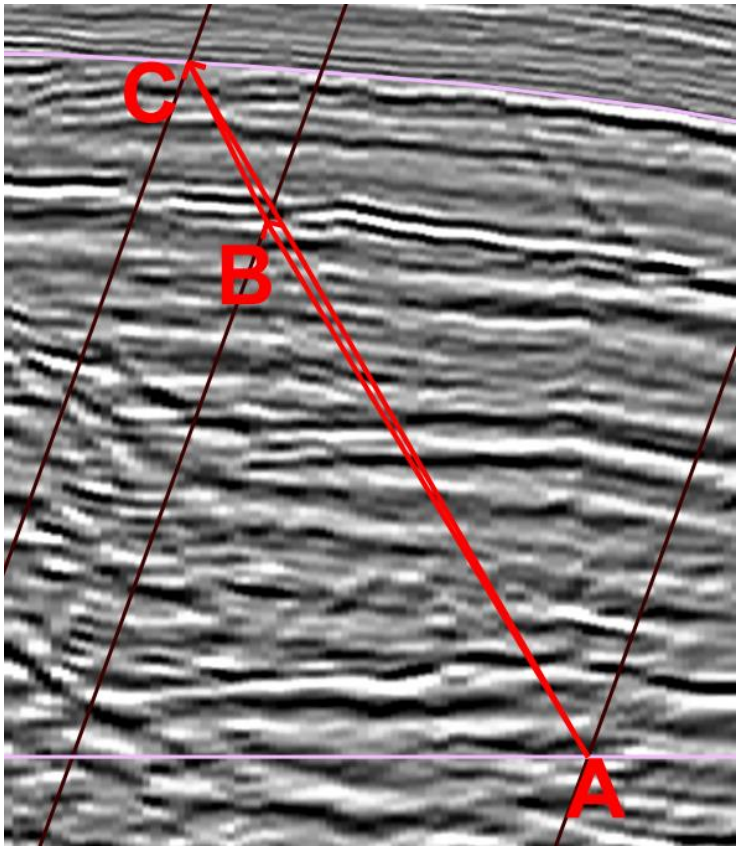

Figure 15. Combined movement vector to accommodate movement along two faults. Line AB shows the displacement of the bed caused by movement on the Manaia fault and the line BC shows the displacement caused by the movement on the Rua fault. The Combined vector AC shows the total displacement of the bed from the two faults.

Modeling the two faults in a way which is compatible with the observed geometry requires an iterative process. To complicate the matter, the geometry of the Rua fault has been deformed by the Manaia fault and so it should not exhibit a simple listric geometry. The process began by modifying the geometry of the Manaia fault modeled in other parts of the area to fit the observed seismic geometry. A simple initial geometry for the Rua fault was then forward modeled to its current position along the Manaia fault along with a bed. This is shown in Figure 16 as the pink dashed line and blue dashed fault which are forward modeled to their respective solid colored line

position. Then the modeled geometry is forward modeled along the Rua fault to align with the observed bed geometry. Changes were then made to the faults so that the observed and modeled bed geometries would match. Careful consideration must be made to maintain a plausible initially listric geometry for each fault.

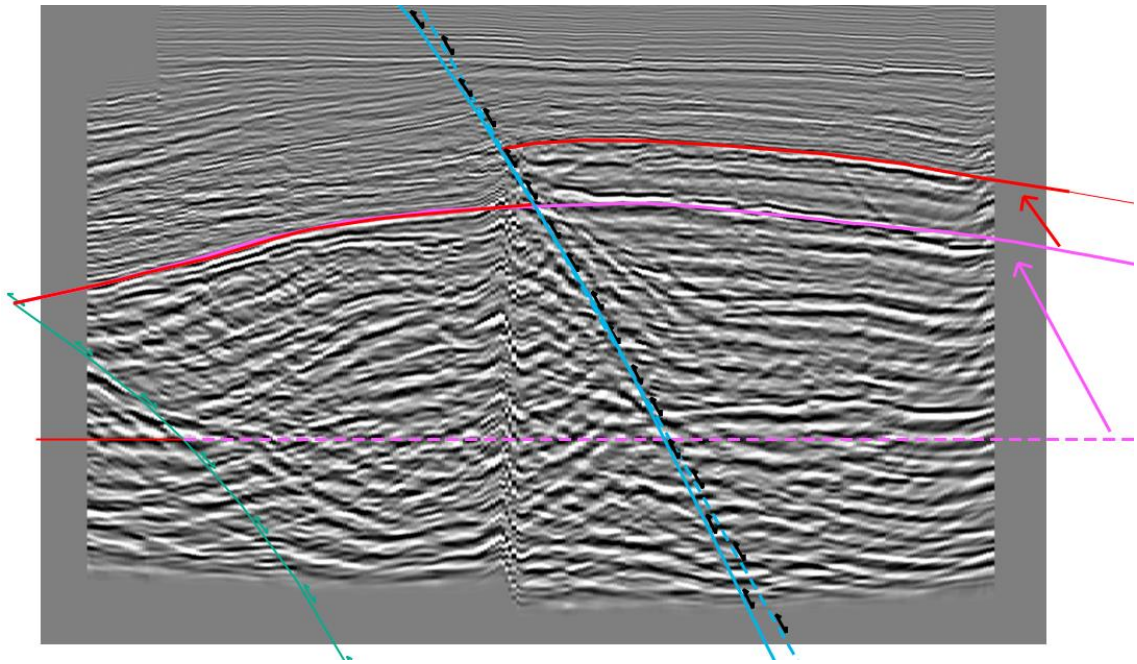

Figure 16. The iterative process used to model the Rua fault. The dashed blue line is the initial geometry of the Rua fault and the solid blue line shows the geometry after forward modeling on the Manaia fault. The dashed pink line shows the initial bed geometry and the solid pink shows an intermediary geometry to account for movement on the Manaia fault. The bed is then forward modeled on the Rua fault to the final position of the bed.

2.6 Unfolding Theory and Method

Restoring these cross sections requires two components to accommodate the deformation from fault bend folding and other folding. The faults have been modeled using inclined shear which allows for restoration of the fault bend folding component. One common technique used to account for fault propagation in cross section restoration is trishear. Trishear uses a zone of triangular deformation in both the hanging wall and footwall to maintain area balance through deformation as shown in Figure 17A-C.

The observed bed and fault geometry shows a triangular zone of deformation from fault propagation folding entirely in the hanging wall. The observed bed and fault geometry is schematically shown in Figure 17D for comparison. The red lines show where the block would be located if it was translated along the fault. In trishear the footwall side of the triangular deformation zone shows increased displacement compared to translation and decreased displacement on the hanging wall side. The observed fault propagation style in comparison shows the opposite relationship. The footwall side shows decreased displacement and the hanging wall side shows increased displacement when compared to the translated block. The observed fault propagation style is not compatible with trishear restoration.

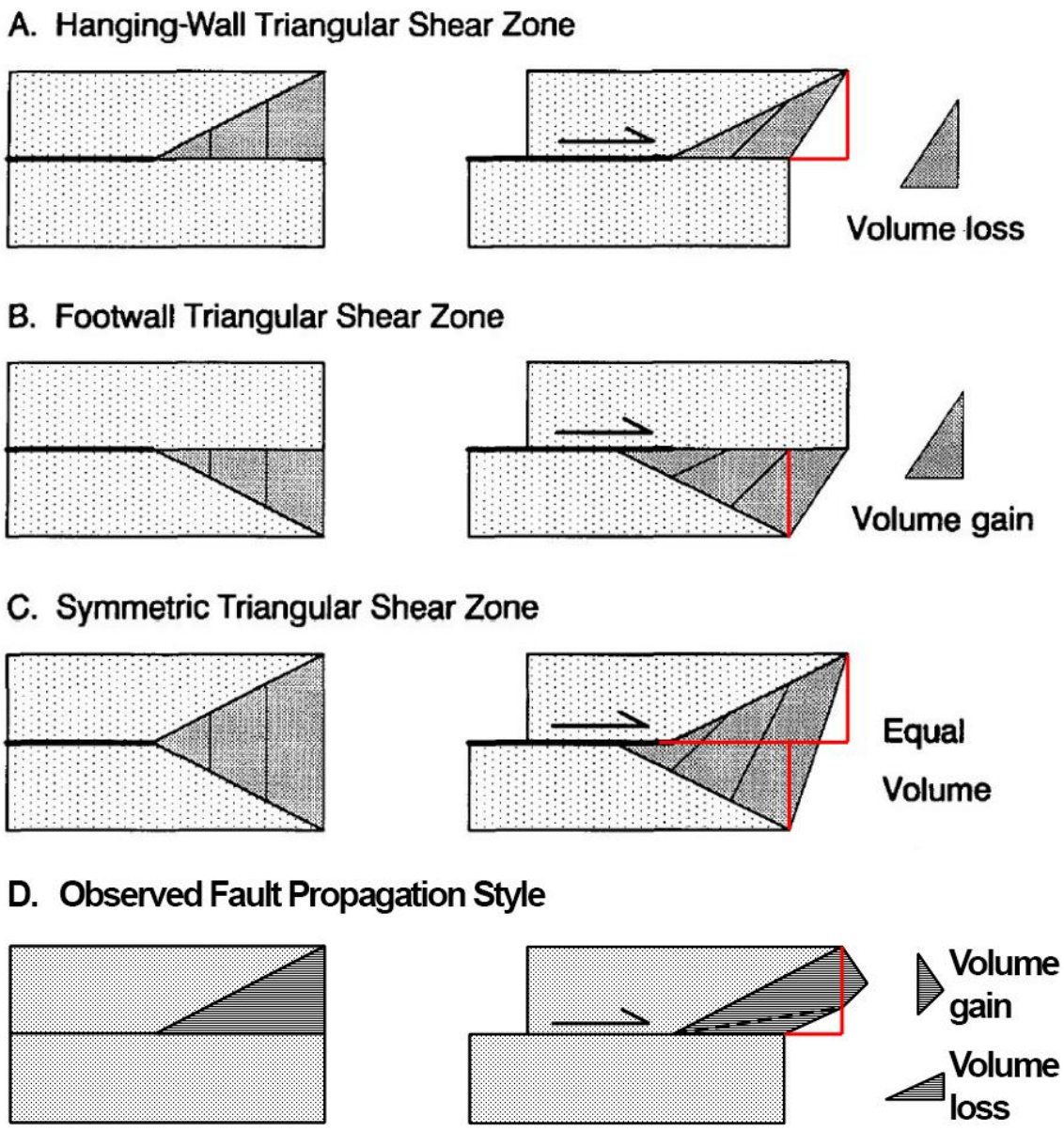

Figure 17. A schematic comparison of the observed fault propagation style with trishear. A and B show the volume gain and loss in the hanging wall and footwall which balance out in trishear. The combined deformation is shown in C with the location of the translated blocks outlined in red. The observed fault propagation style in the study area is shown in D. Modified from Erslev (1991).

To restore fault propagation folding a flattening algorithm was used after moving the bed using inclined shear so the back limb was in the original position. A variety of fold flattening methods are available and they imply different mechanisms of

deformation. Three common methods include line length preservation, simple shear, and flexural slip folding. Line length flattening is the simplest method and simply straightens the lines while maintaining length. Beds cannot be passively unfolded relative to another bed so thickness variations will not be maintained. This method is not appropriate for this application.

Simple shear unfolding displaces the template bed a variable amount along a set inclination. A bed passively unfolded will be displaced by the same amount along the inclination. Inclined shear flattening does not preserve line length or area. Figure 18 shows the P10 bed in pink and the P00 bed in red. The arrows show the schematic vector needed to restore the bed to the original position which is shown as a dashed line of the same color. The beds are believed to be correctly modeled to the right of the right of the right most dashed black line and so any flattening method should not deform the beds past that line. The vectors needed to restore the bed vary in inclination which shows that inclined shear is not appropriate in this situation.

The third common unfolding method is flexural slip unfolding. This algorithm works by translating beds a variable amount along the bed bisectors. This method can passively unfold beds relative to a template bed. This method maintains a constant area and line length. Flexural slip unfolding requires the user to define a pin from which flow paths are determined. This is the method which was used in this study with the beds pinned relative to the fault.

Figure 18 was generated to show the importance of considering the fold flattening algorithm and the associated parameters. The pink P10 bed was used as a template bed to passively unfold the red P00 bed. Different algorithms were used with

varying parameters and the corresponding productions are shown as solid purple lines. Inclined shear was used with a shear angle parallel to the fault, vertical, and parallel to the right most dashed black line. Flexural slip was used with a vertical pin and a pin parallel to the two black lines. The blue line was generated using flexural slip with the fault as a pin. The blue line is believed to be the most correct geometry.

The different passively unfolded bed geometries show significant variance. Only the beds modeled with parameters parallel to the fault maintained contact with the fault. There is also significant variation in the location of the thickest part of the P10 bed. The incorrect unfolding algorithm would suggest an incorrect depocenter which could lead to incorrect stratigraphic interpretation and modeling. Incorrect methods also significantly changed the total area affected by fault propagation.

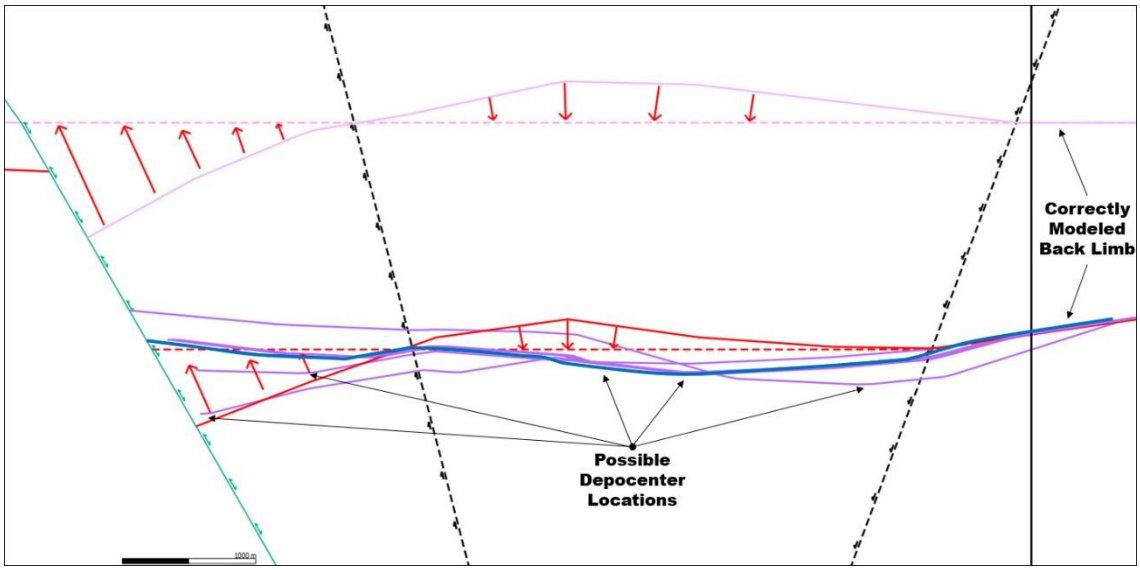

Figure 18. A comparison of various flattening techniques. The template line is shown in pink and is flattened to the dashed pink position. The solid red line is passively flattened and the modeled position using inclined shear is shown as a dashed red line. The solid purple lines show the different outputs and the solid blue line is the result of the flexural slip algorithm which was used for restorations.

Chapter 3. Geometry and Evolution of the Kupe Structure

3.1 Maps

The time surfaces and resulting depth conversions are shown for three key horizons, N40, P10, and the basement, in Figures 19 through 24. The depth converted basement structure map is shown in figure 19. Some minor artifacts from depth conversion can be seen in the Manaia fault footwall.

The depth converted P10 horizon is shown in Figure 21. The P10 horizon is the most important horizon for fault modeling and analyzing the structure. It was the last unit deposited during extension and is assumed to have had a near horizontal dip before compressional deformation. The extensional units below the P10 horizon show apparent drape folding deformation while the P10 horizon does not.

The geometry of the P10 horizon shows two en echelon structures related to the Manaia and Rua faults. The structure on the Manaia fault is doubly plunging, whereas that on the Rua fault plunges north within the study area. The structural traps for the Kupe South field and other accumulations are localized along the crestal area within the transfer zone between the two faults.

The depth converted N40 horizon is shown in figure 23. The N40 horizon is the last picked horizon showing compressional deformation. There is no apparent fault offset in this horizon suggesting that all fault slip is being accommodated by fault propagation or fault-independent folding. The structurally highest part of the N40 horizon has been eroded away in the southern part of the map.

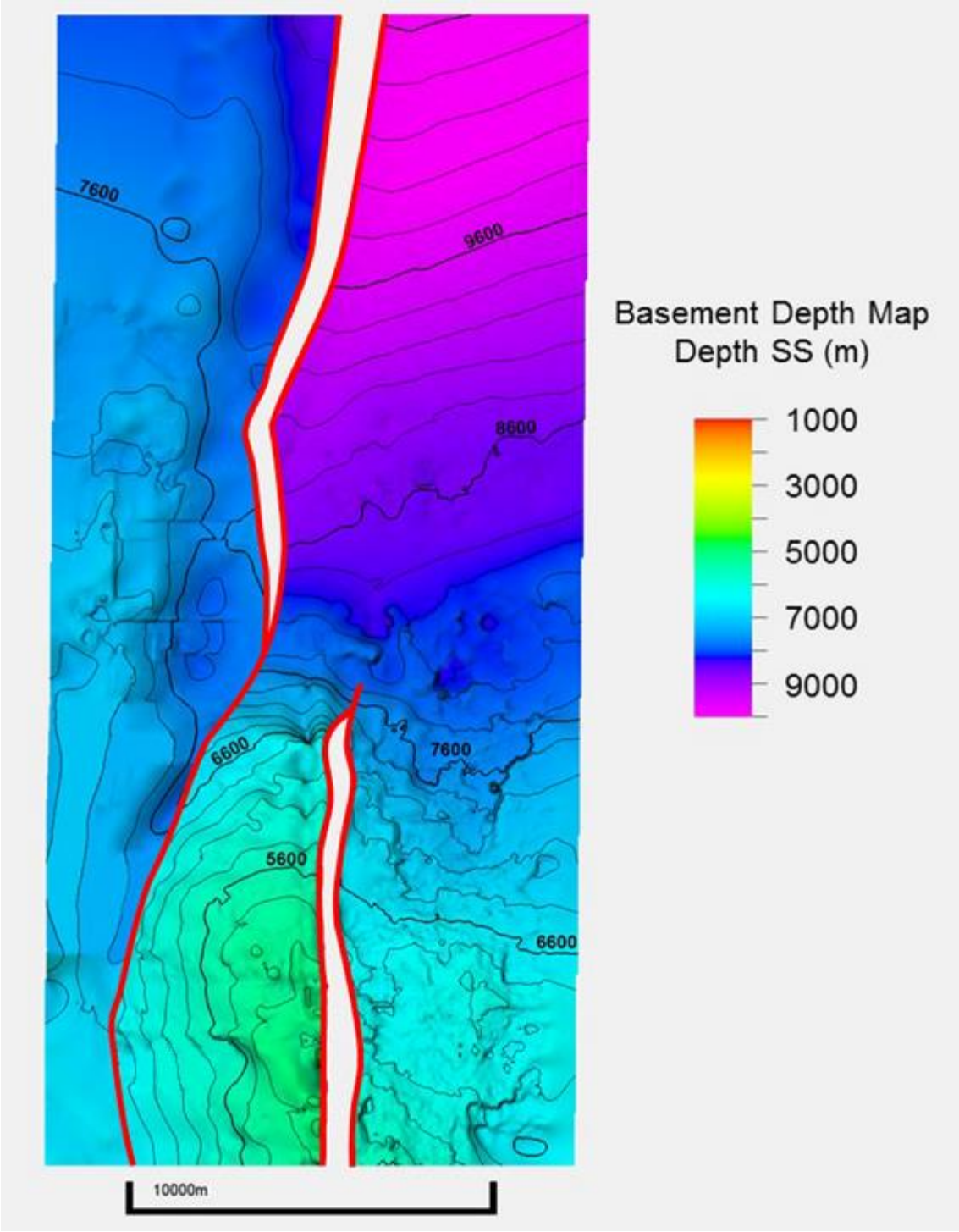

Figure 19. Basement depth map.

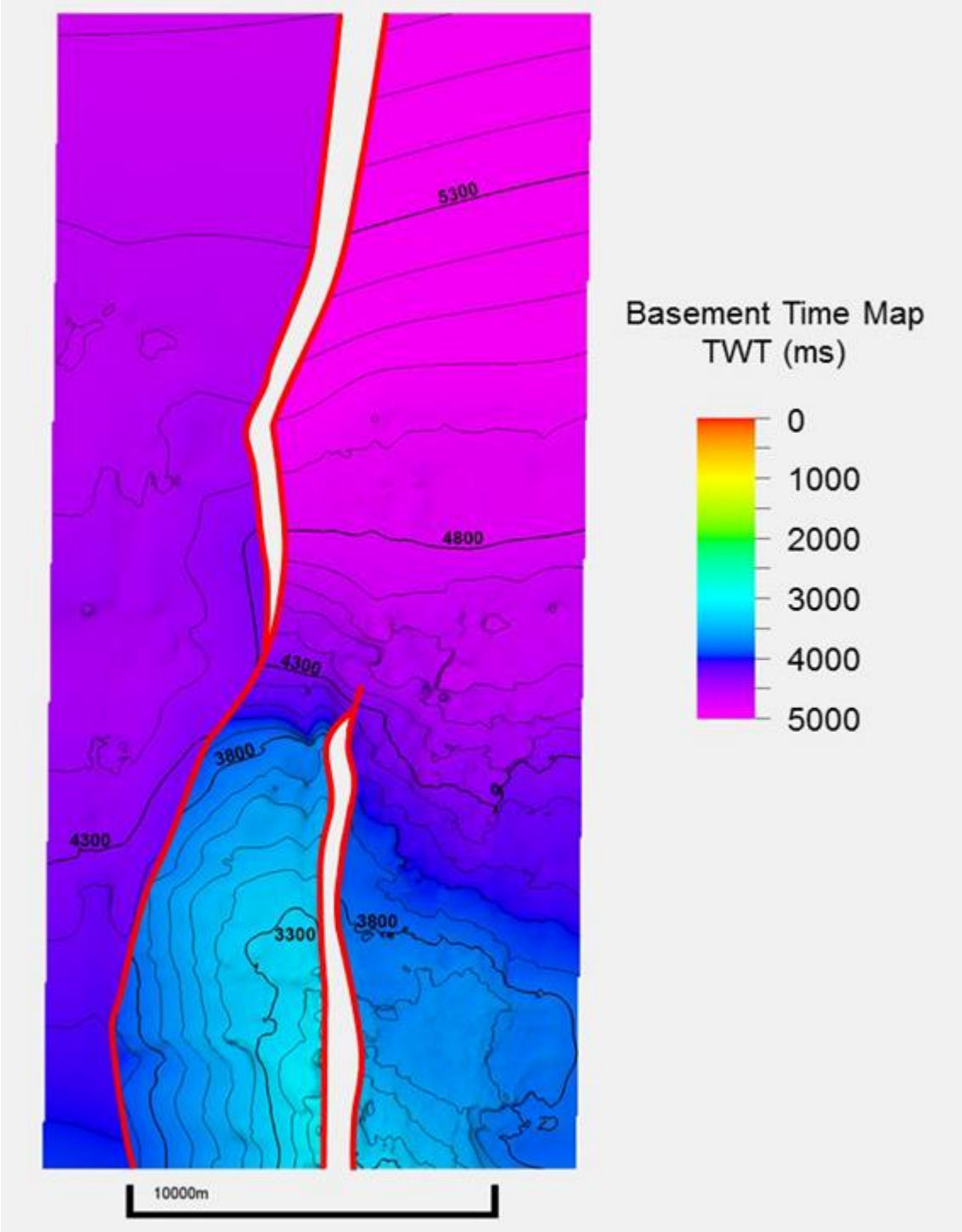

Figure 20. Basement time map.

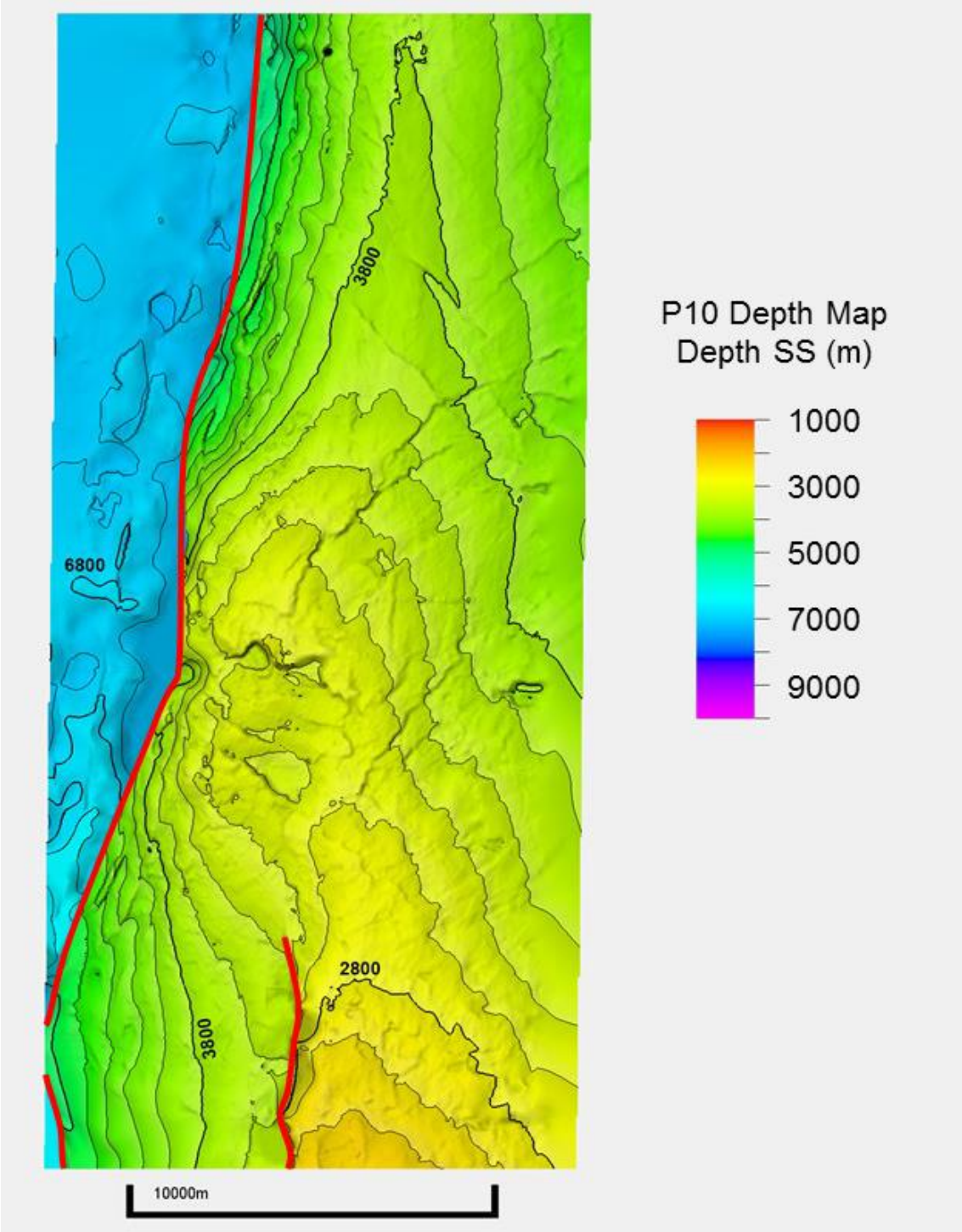

Figure 21. P10 depth map.

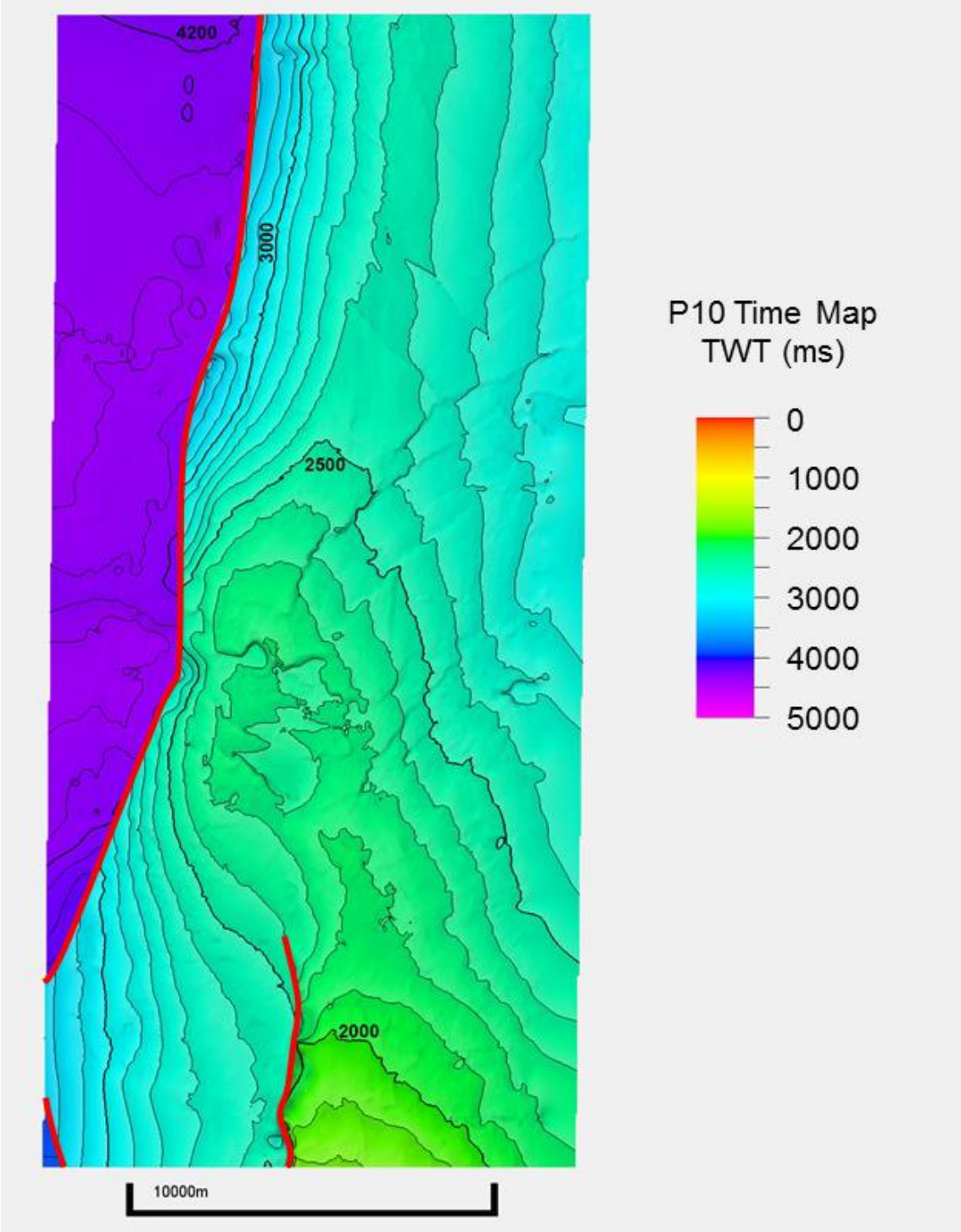

Figure 22. P10 time map.

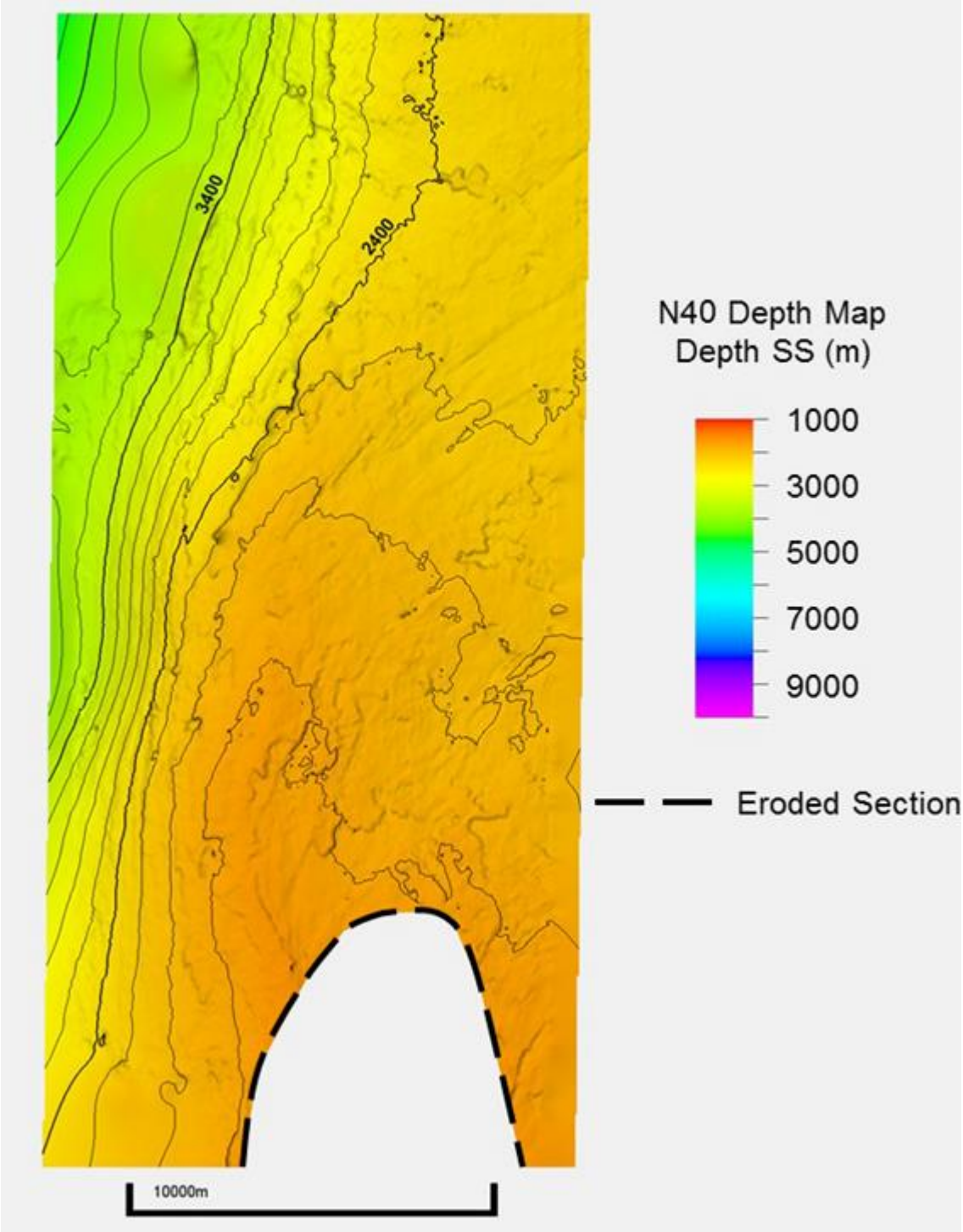

Figure 23. N40 depth map.

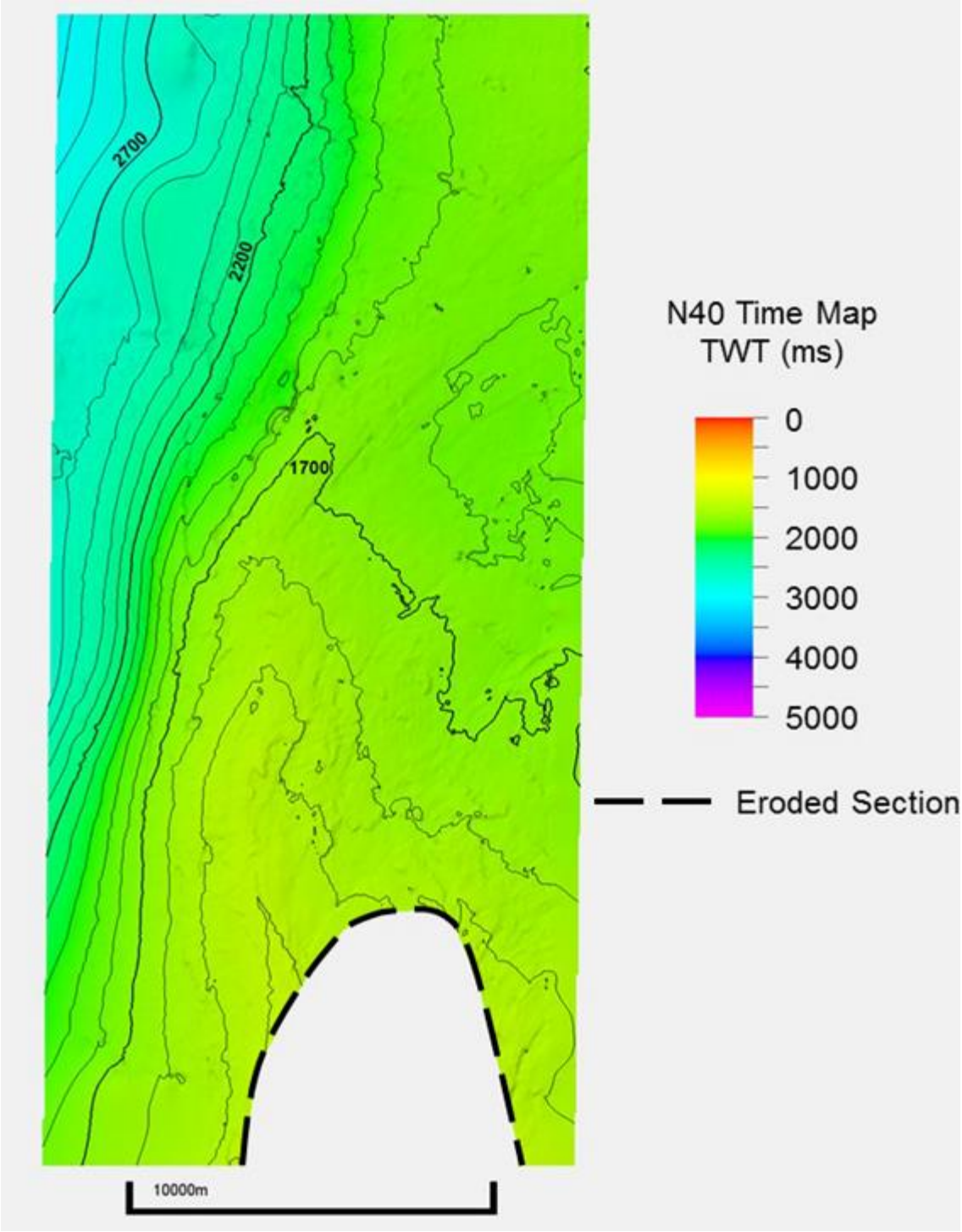

Figure 24. N40 time map.

3.2 Cross Sections

A series of ten equally-spaced time and depth cross sections was constructed to cover the Kerry 3D seismic dataset. Their location can be seen in figure 26 where they have been labelled as lines A through J. Figure 25 shows the legend for the cross sections. Additional cross sections were needed in the central part of the model area where the Manaia fault has a significant change in strike. A second set of infill cross sections were made between lines D through G and the fault modeled from these lines was used to when creating the 3D model.

The cross sections show the modeled faults with interpreted beds to a depth of 11km in figures 27 through 46. The cross sections were cut off at this depth because it coincides with the approximate depth which can be modeled with the seismic volume used. The faults were also modeled to their decollement depth but modeling at this depth has a high degree of uncertainty and requires incorporating additional data sources with different quality. The deep fault geometry is discussed in section 4.2 of this study. The seismic line used for each cross section is shown below the section.

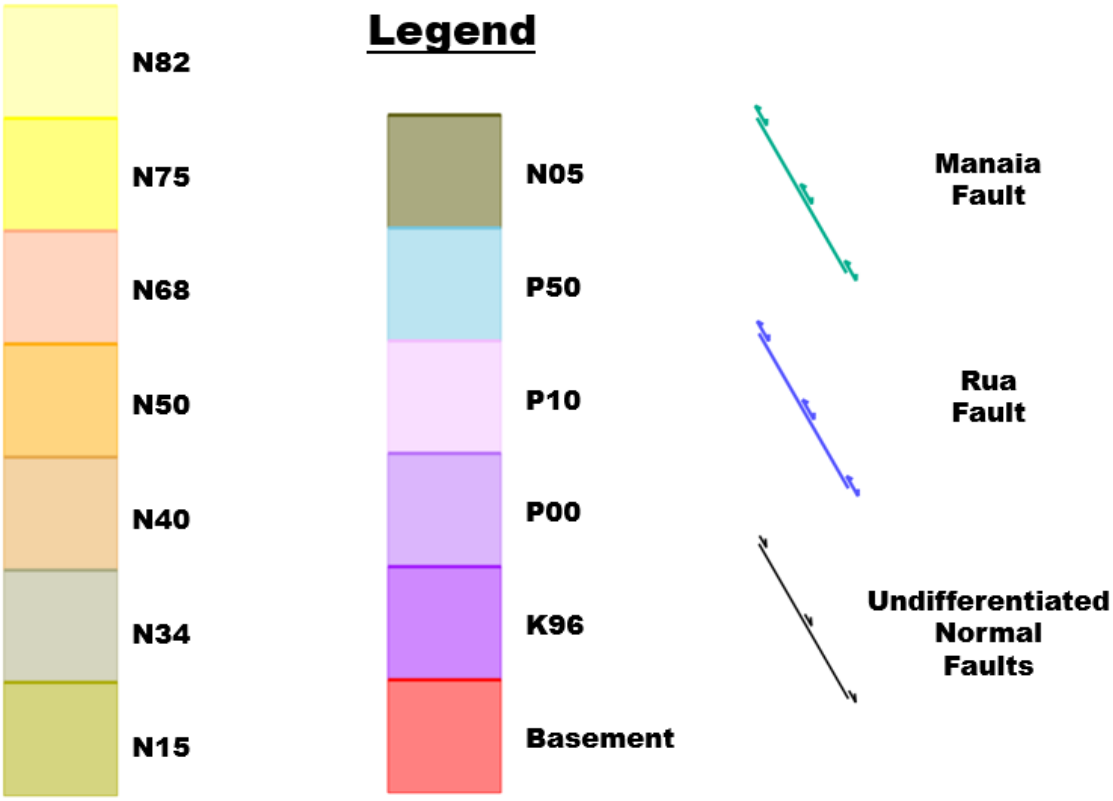

Figure 25. Cross section legend.

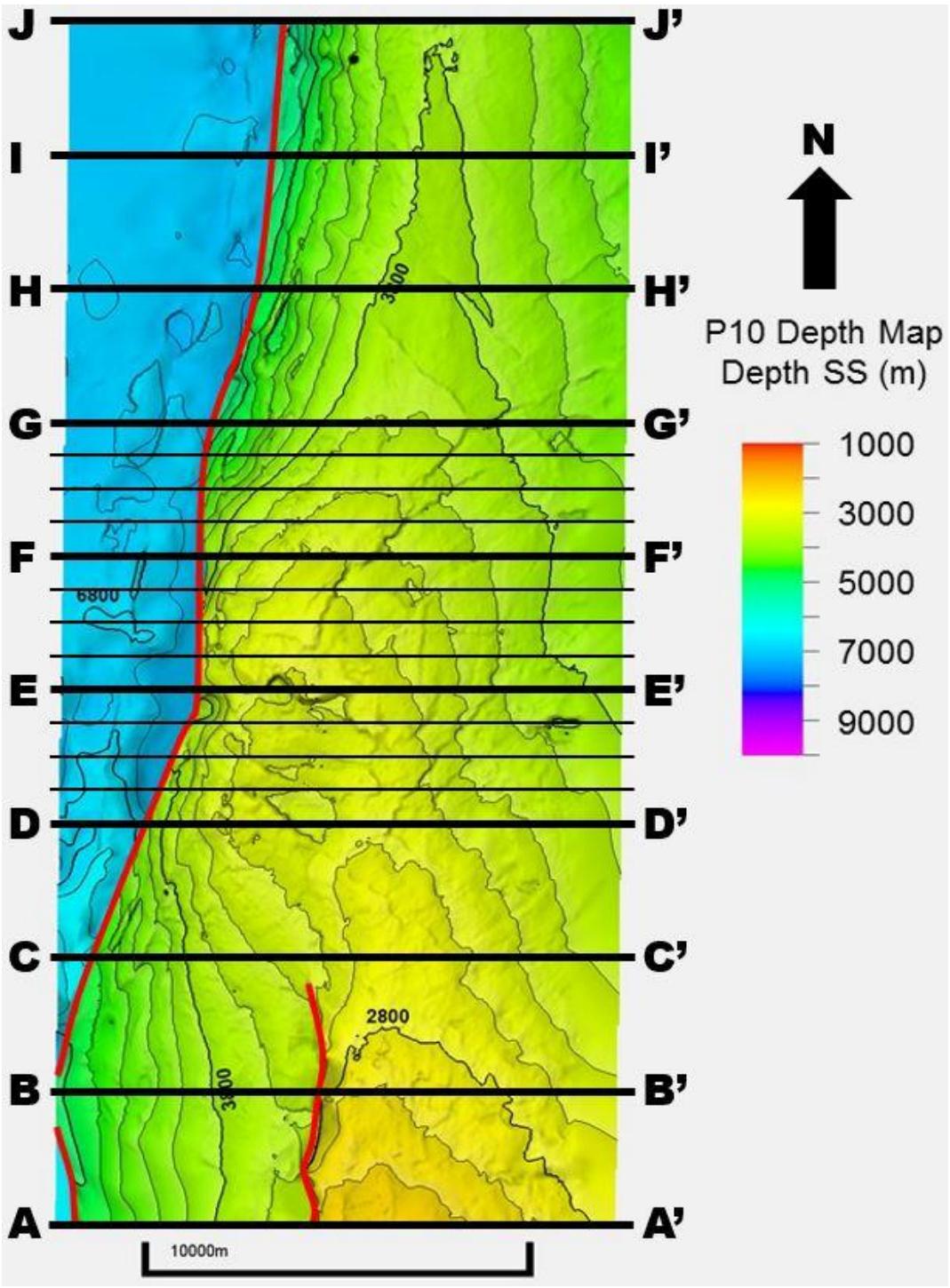

Figure 26. Map of the depth to basement with cross section locations to show their location relative to fault locations.

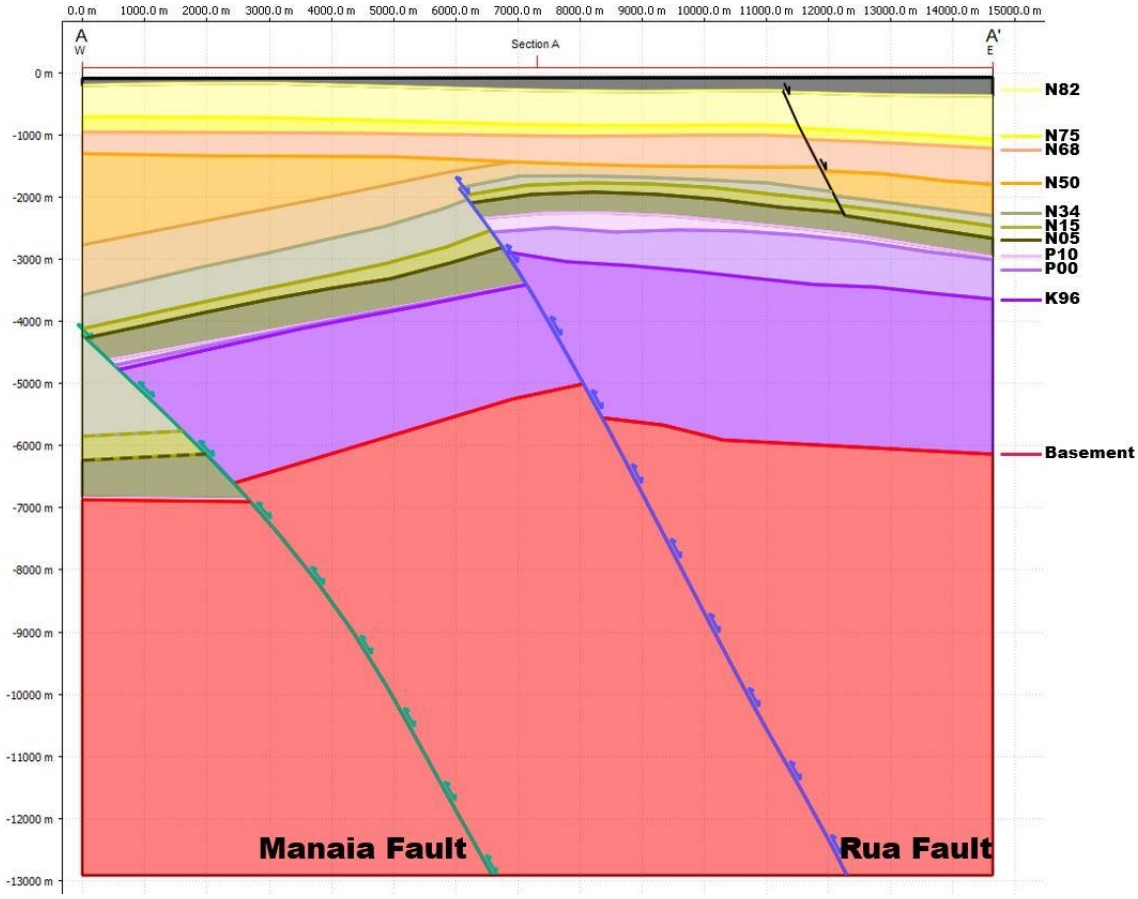

Figure 27. Depth cross section A.

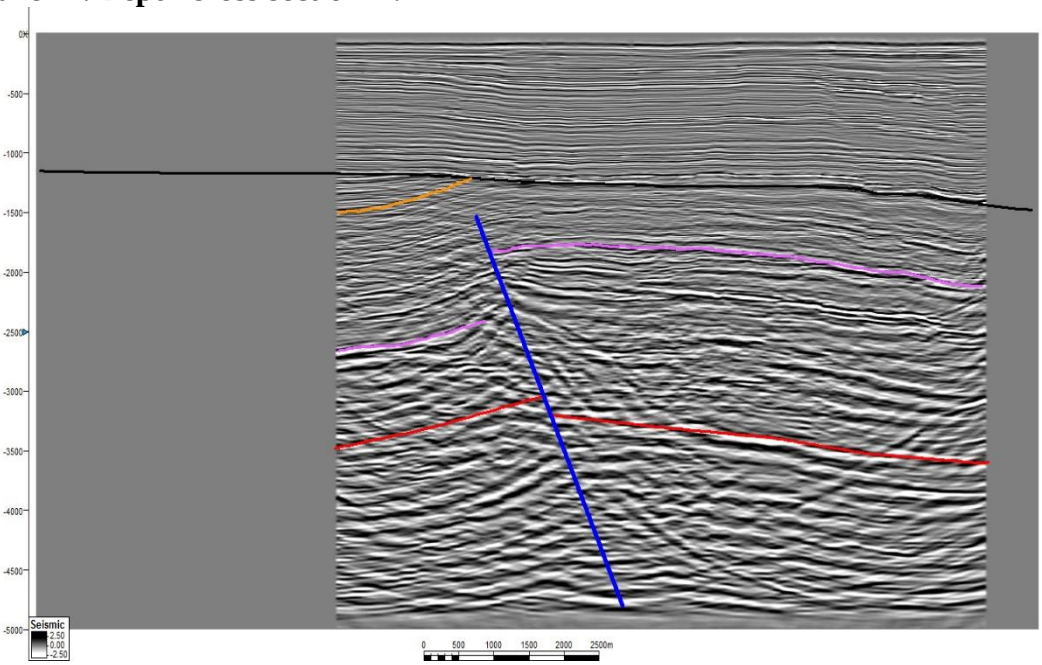

Figure 28. Time cross section A.

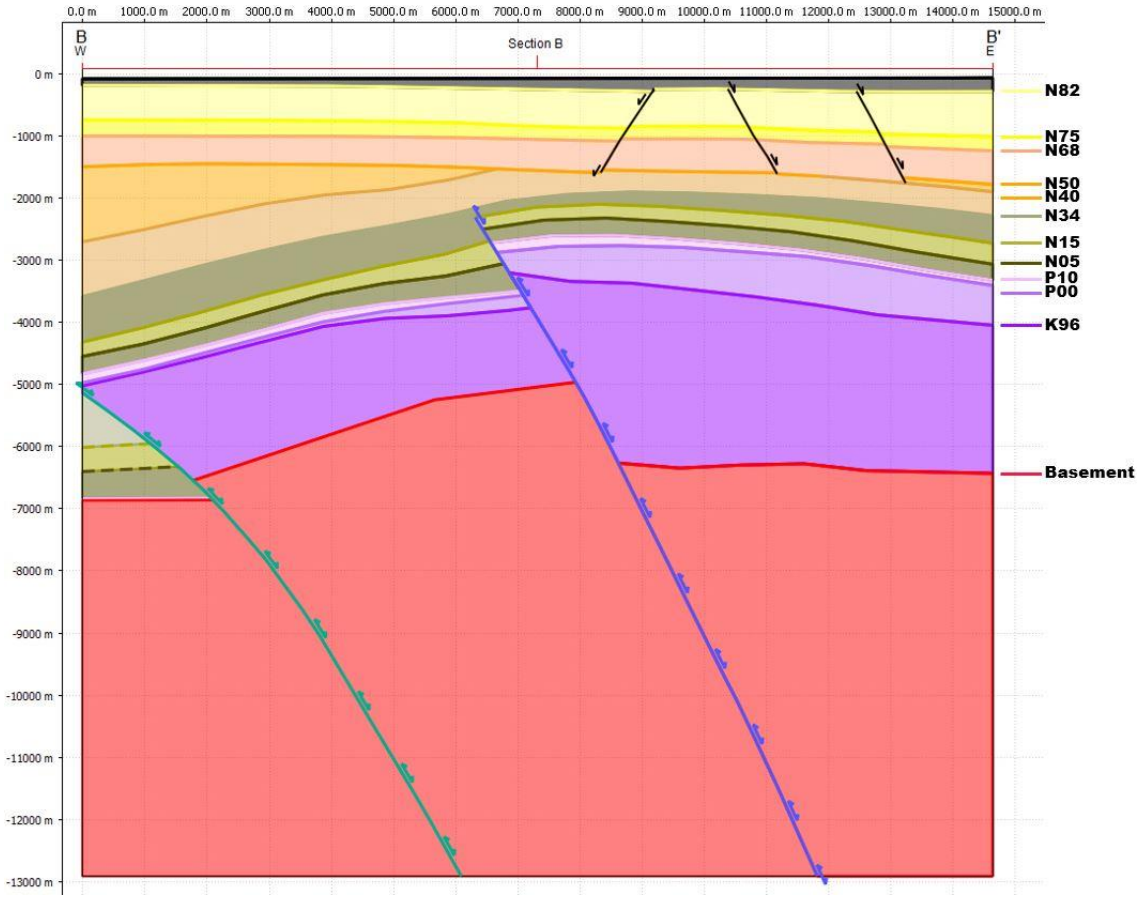

Figure 29. Depth cross section B.

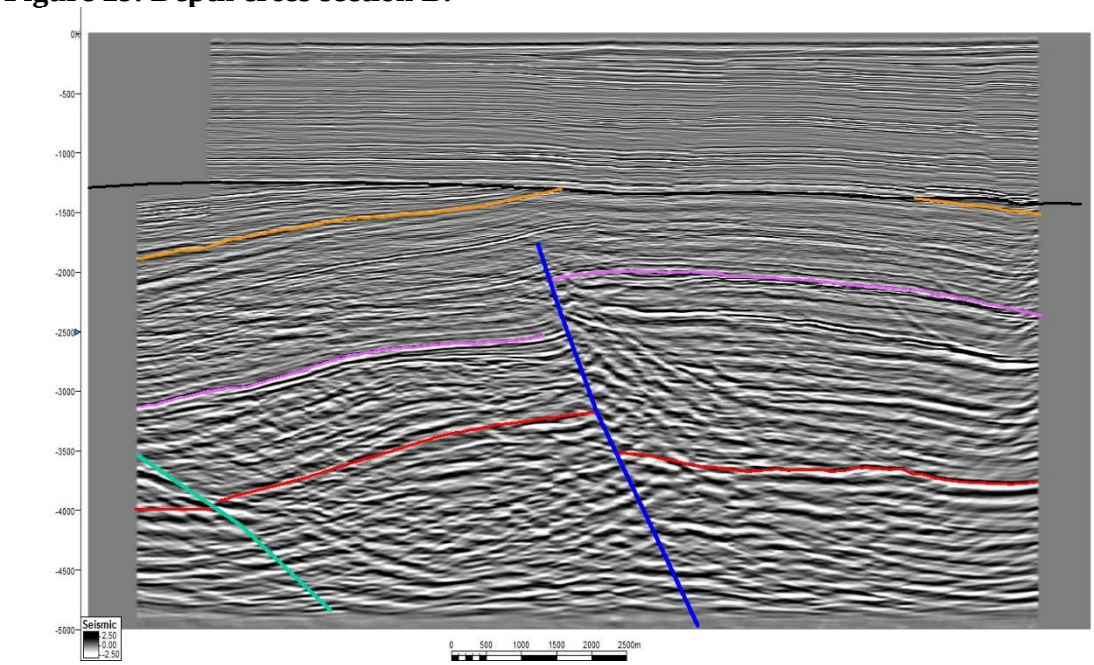

Figure 30. Time cross section B.

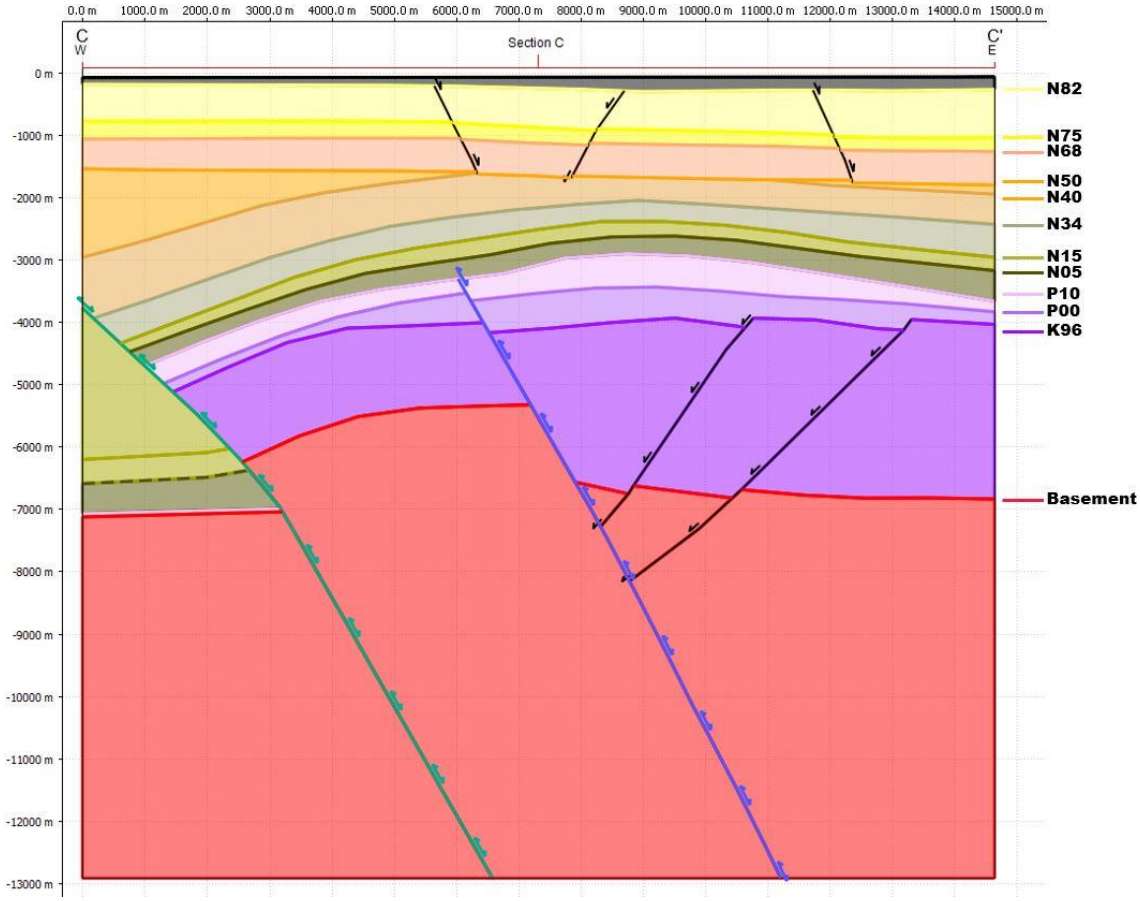

Figure 31. Depth cross section C.

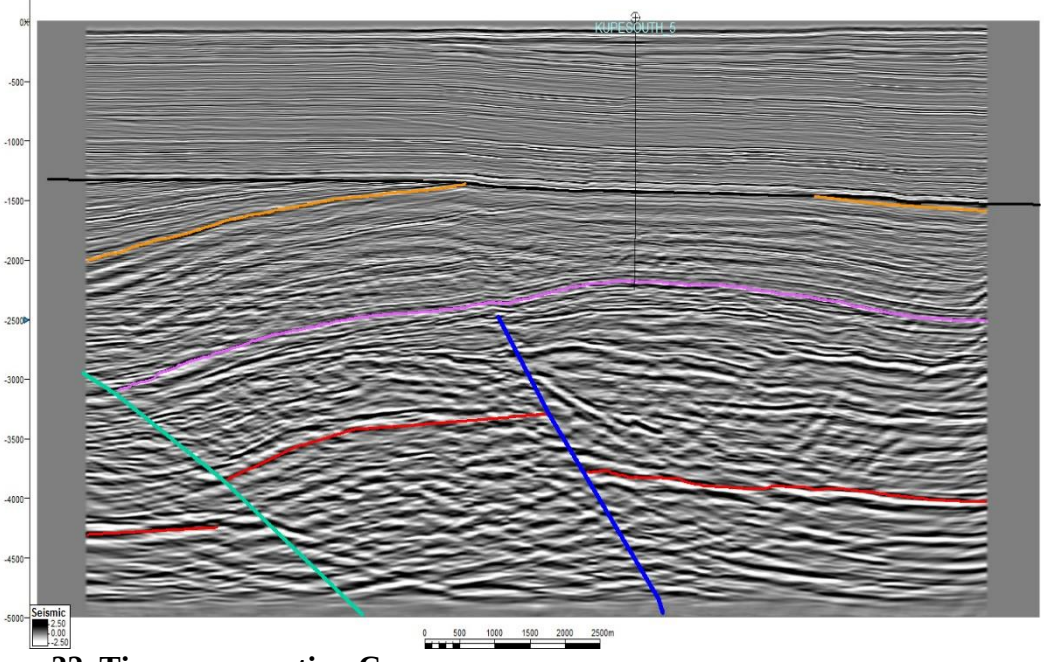

Figure 32. Time cross section C.

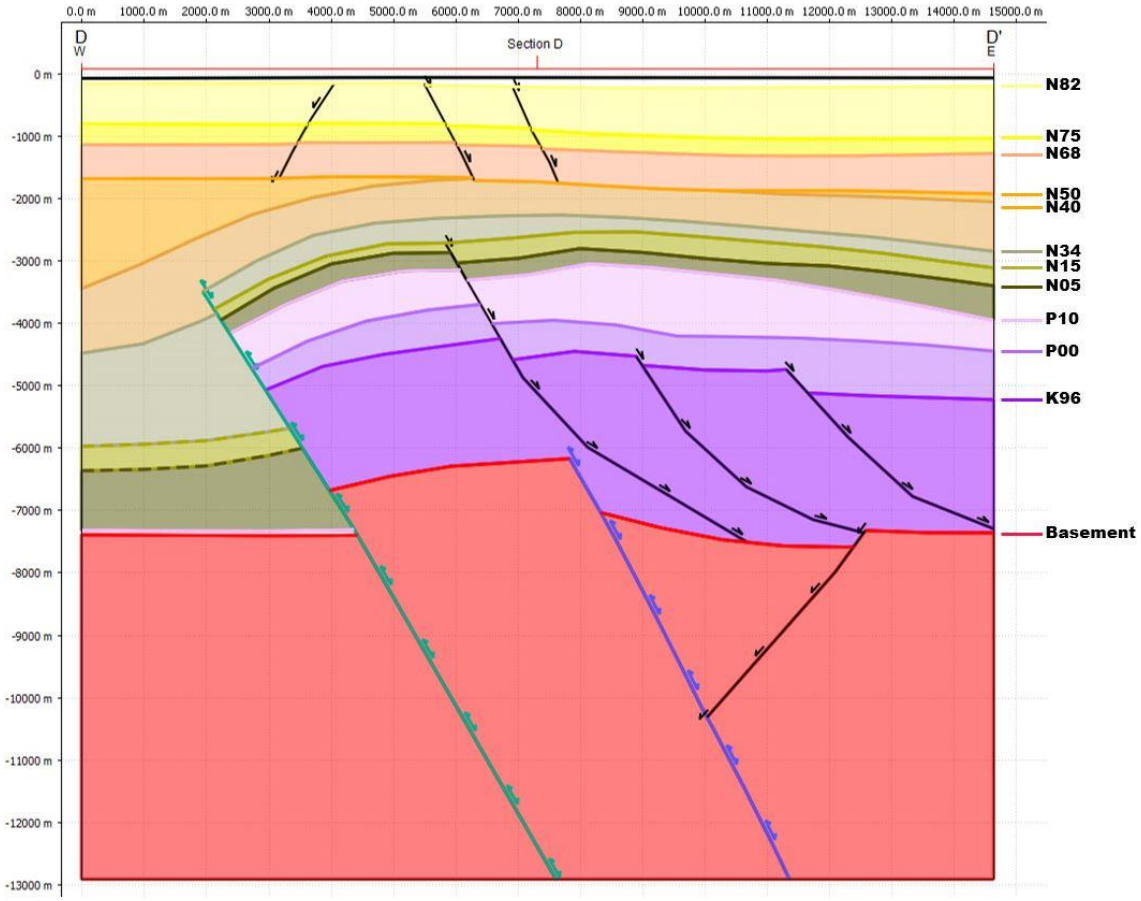

Figure 33. Depth cross section D.

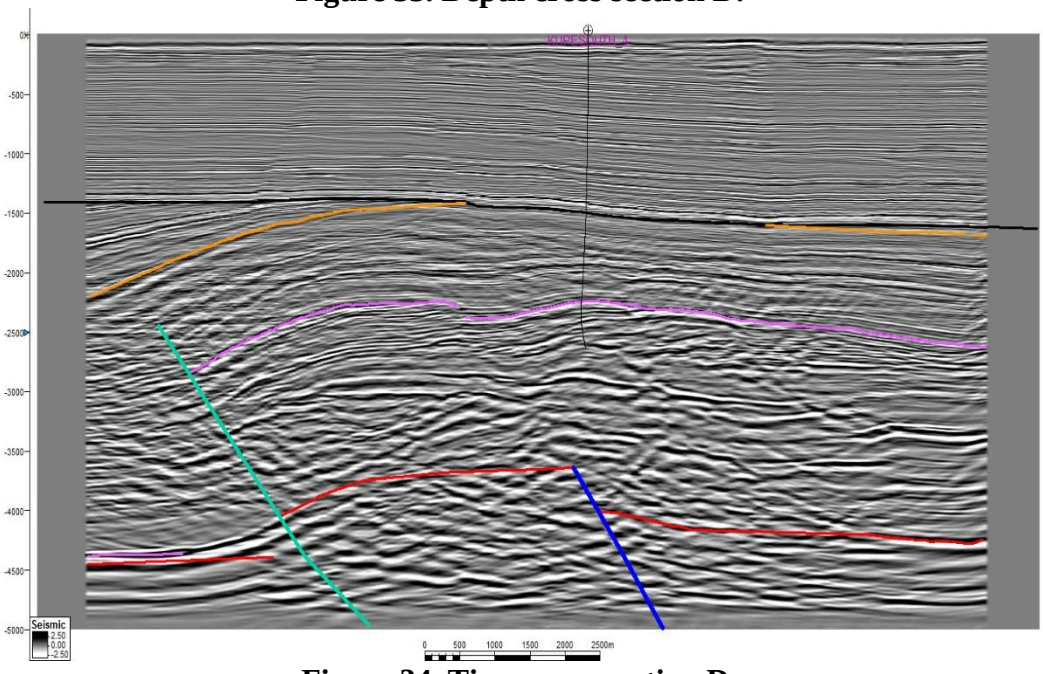

Figure 34. Time cross section D.

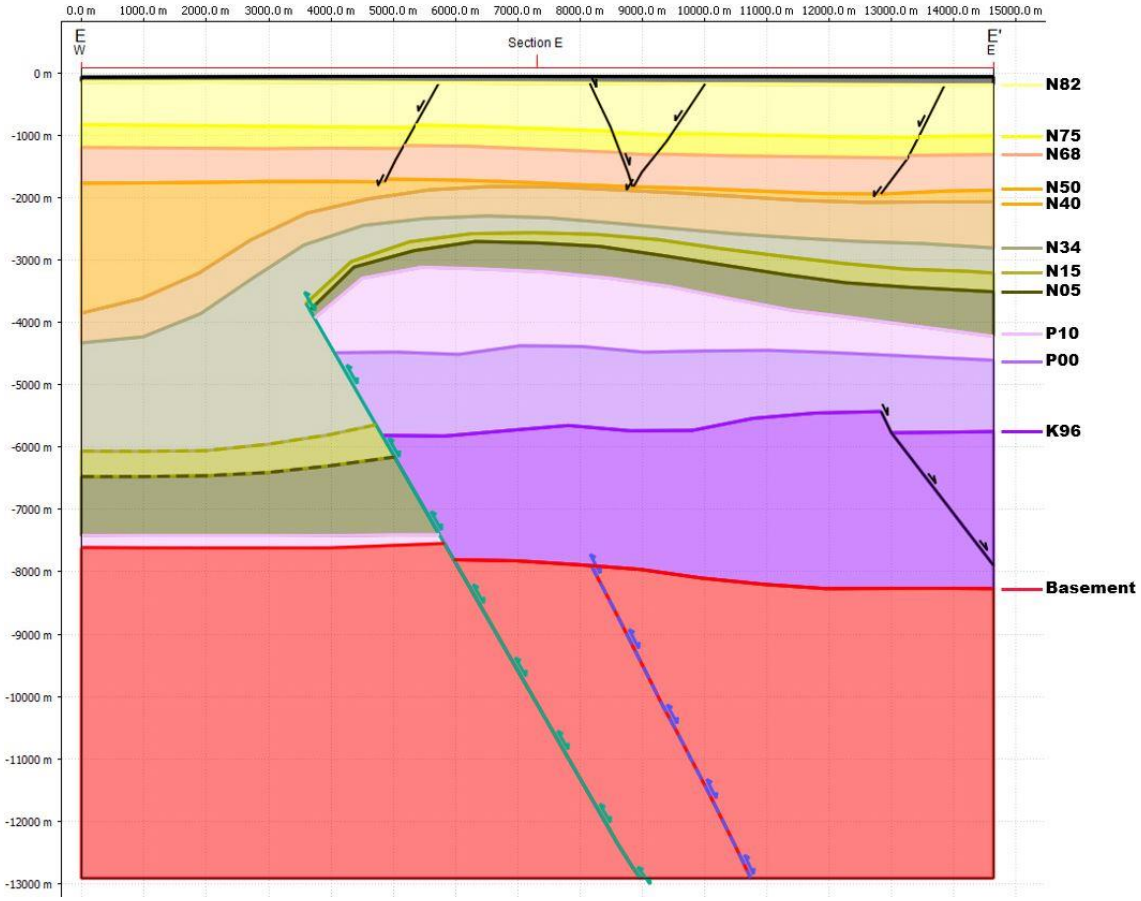

Figure 35. Depth cross section E.

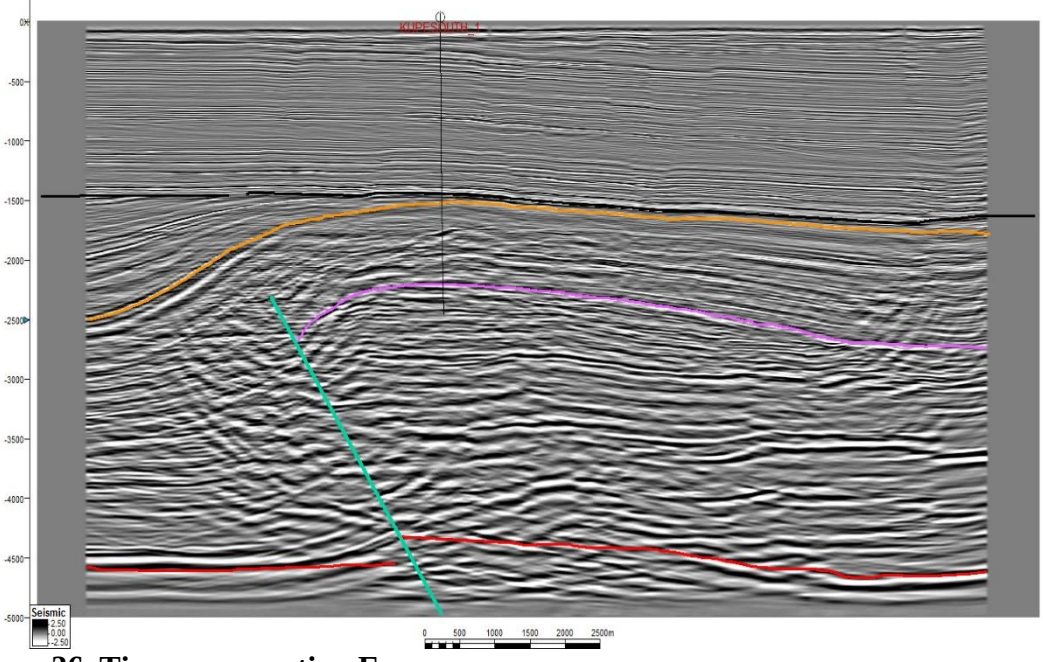

Figure 36. Time cross section E.

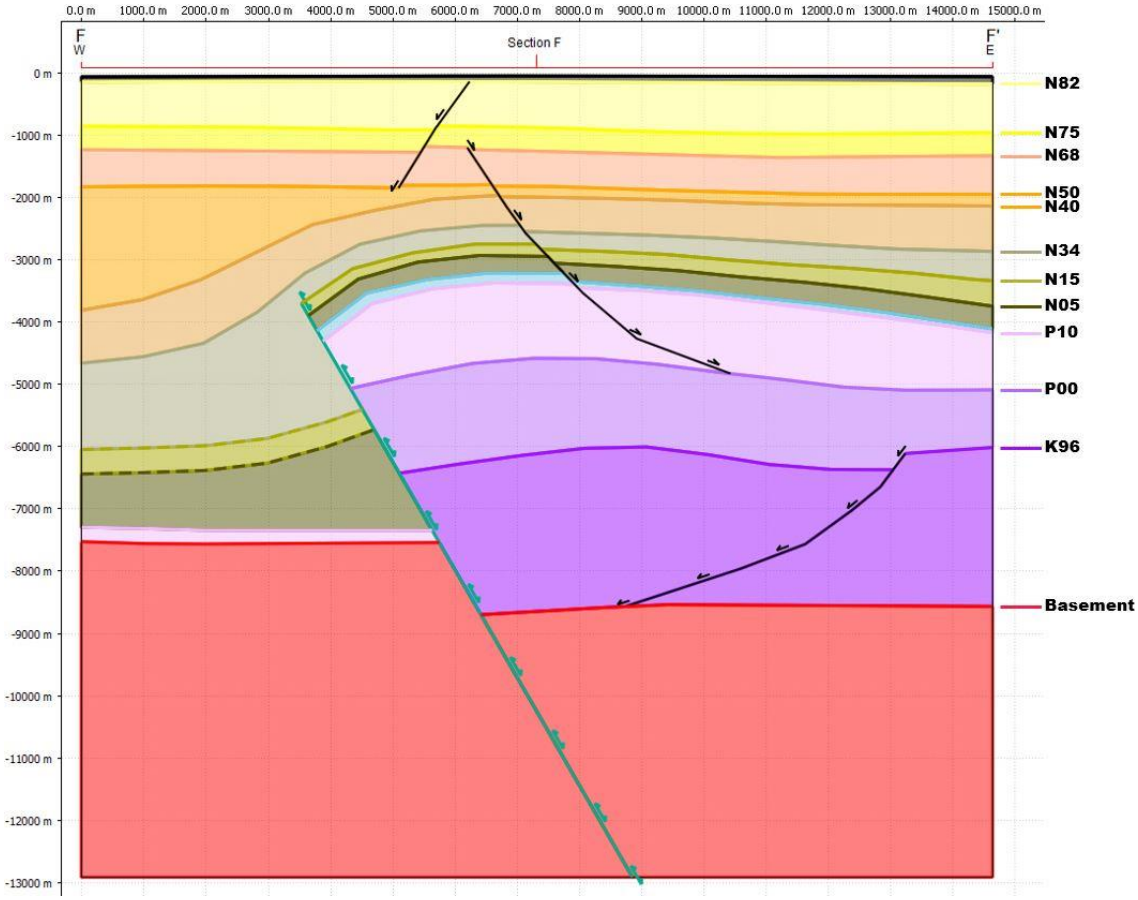

Figure 37. Depth cross section F.

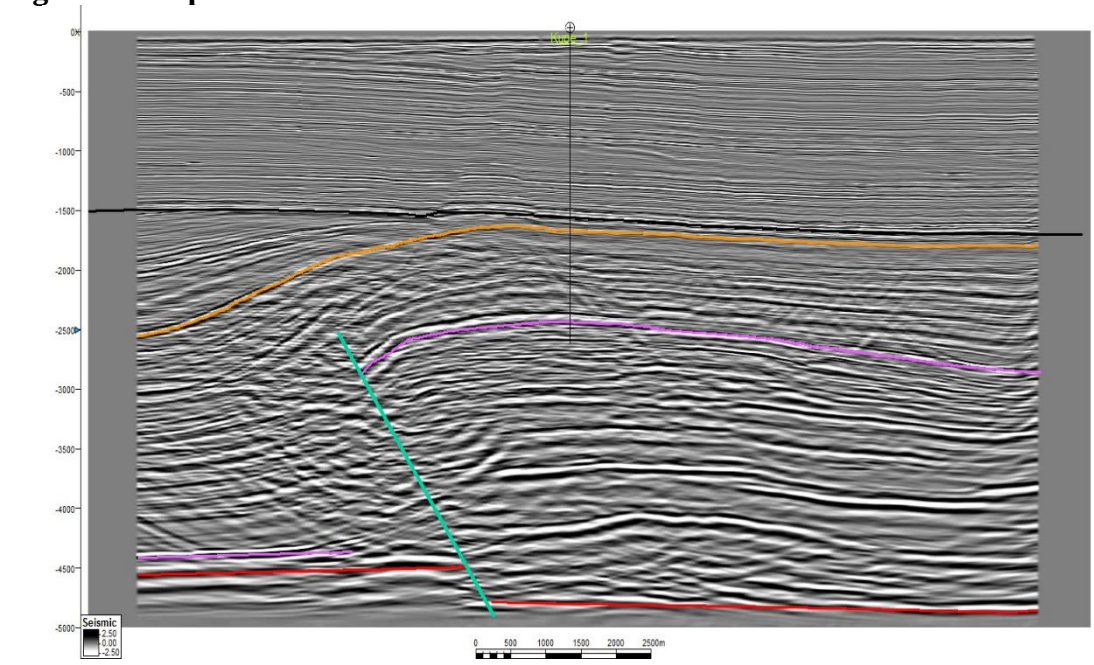

Figure 38. Time cross section F.

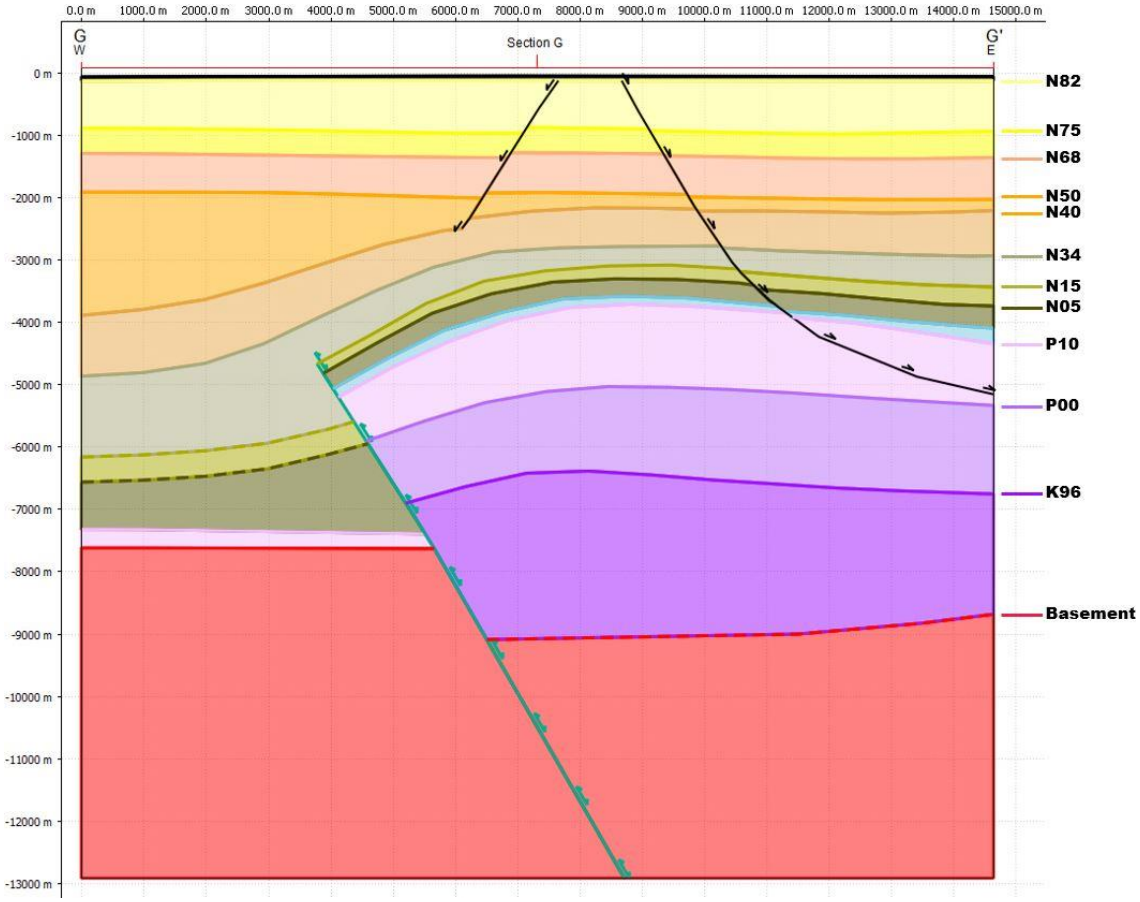

Figure 39. Depth cross section G.

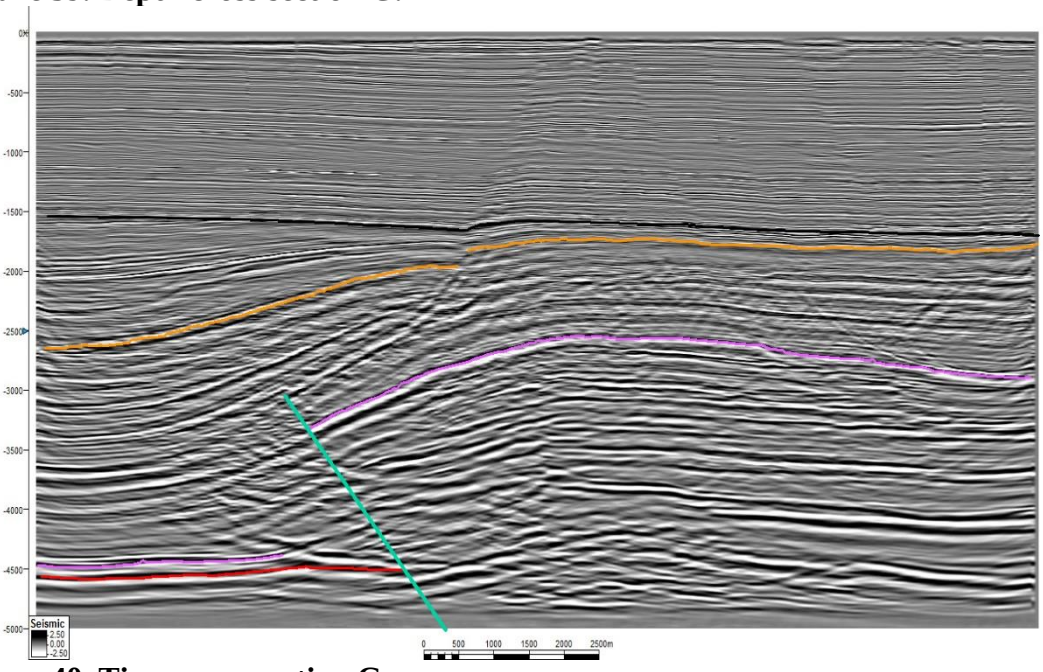

Figure 40. Time cross section G.

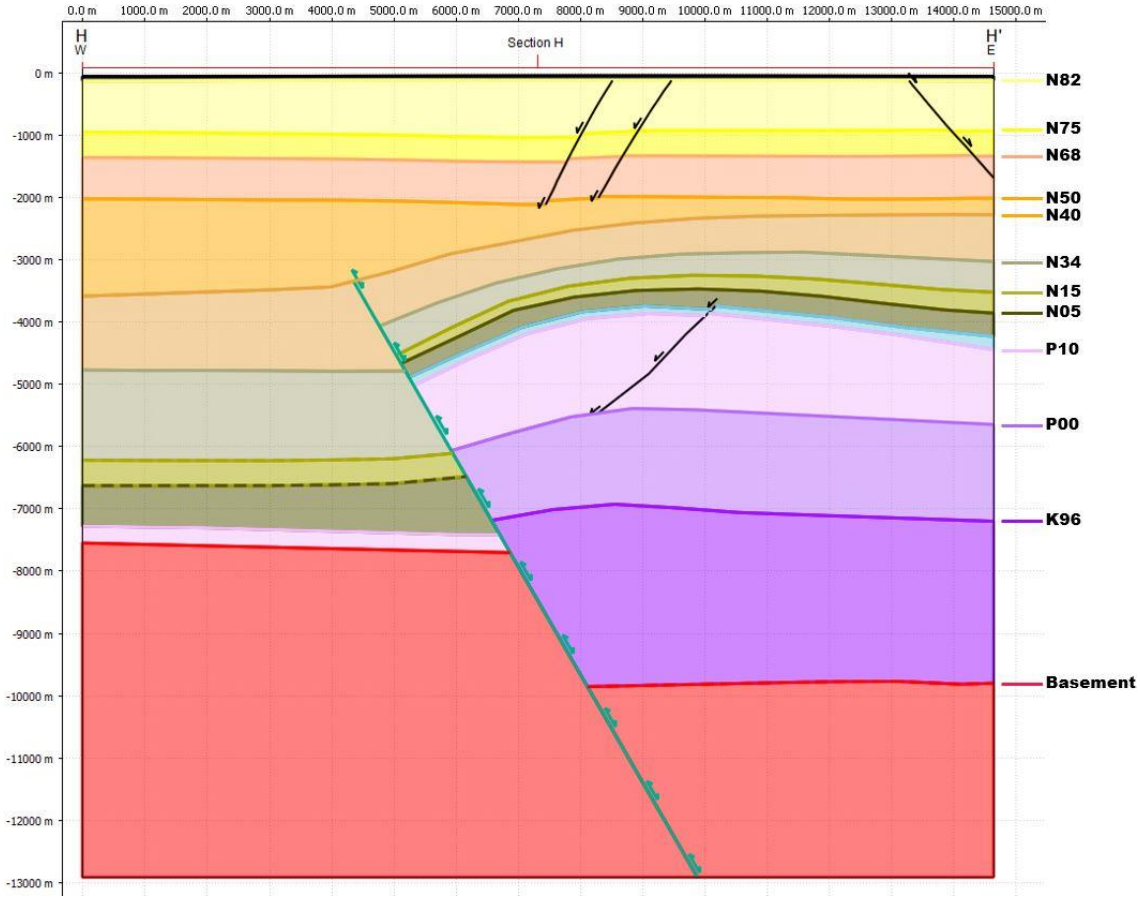

Figure 41. Depth cross section H.

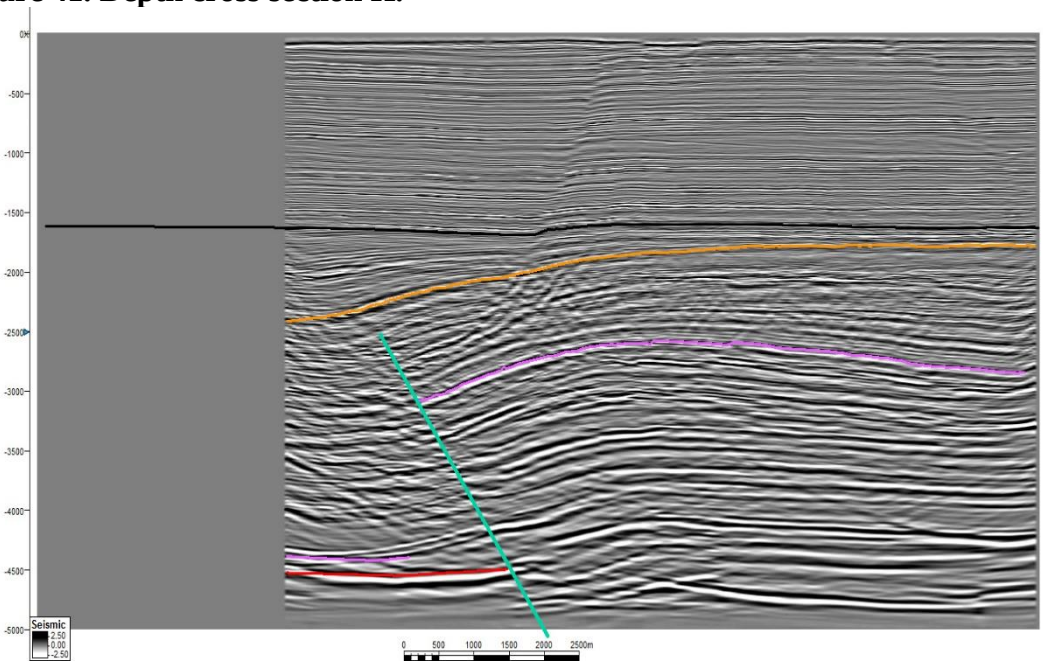

Figure 42. Time cross section H.

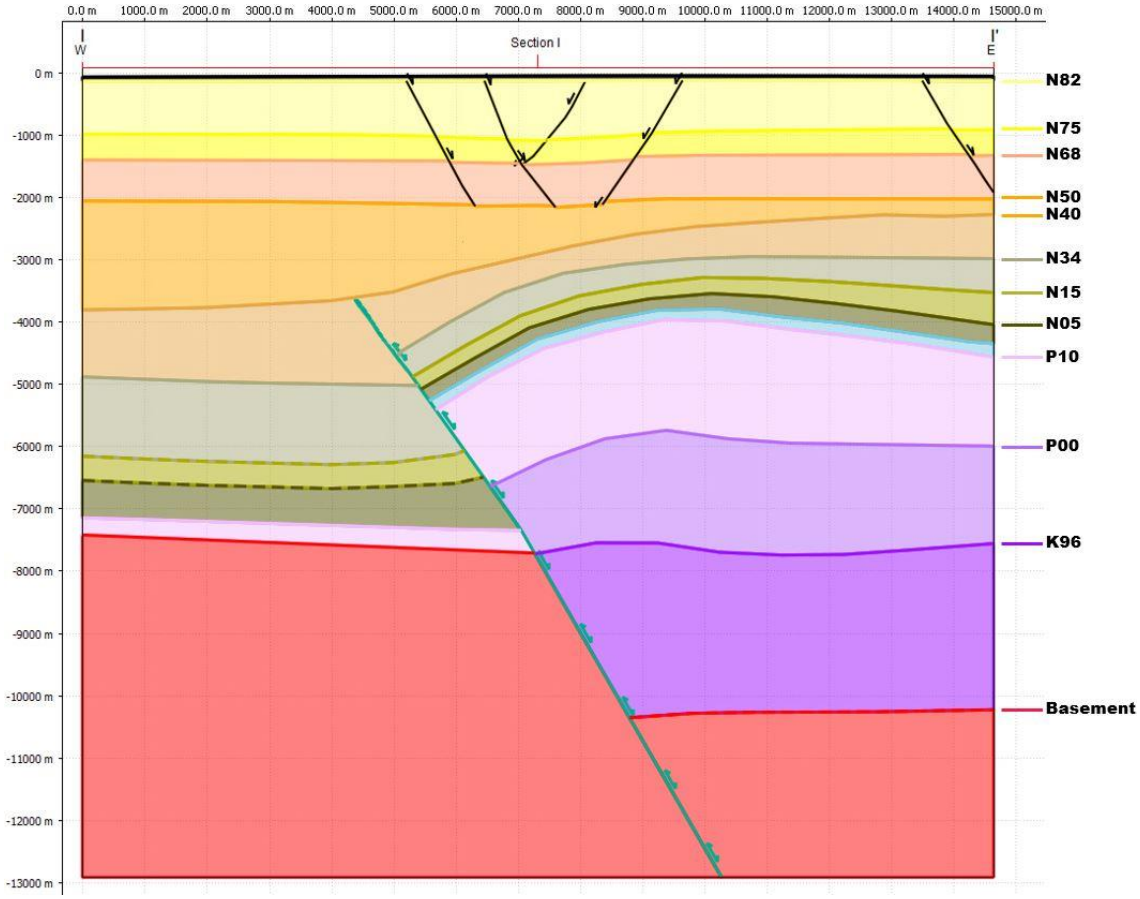

Figure 43. Depth cross section I.

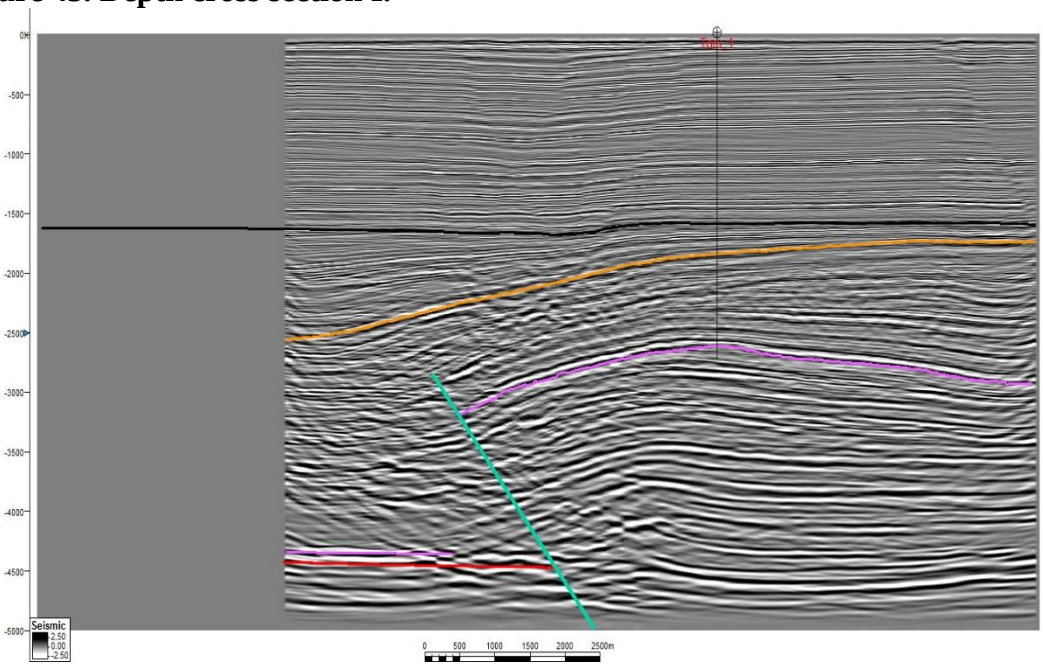

Figure 44. Time cross section I.

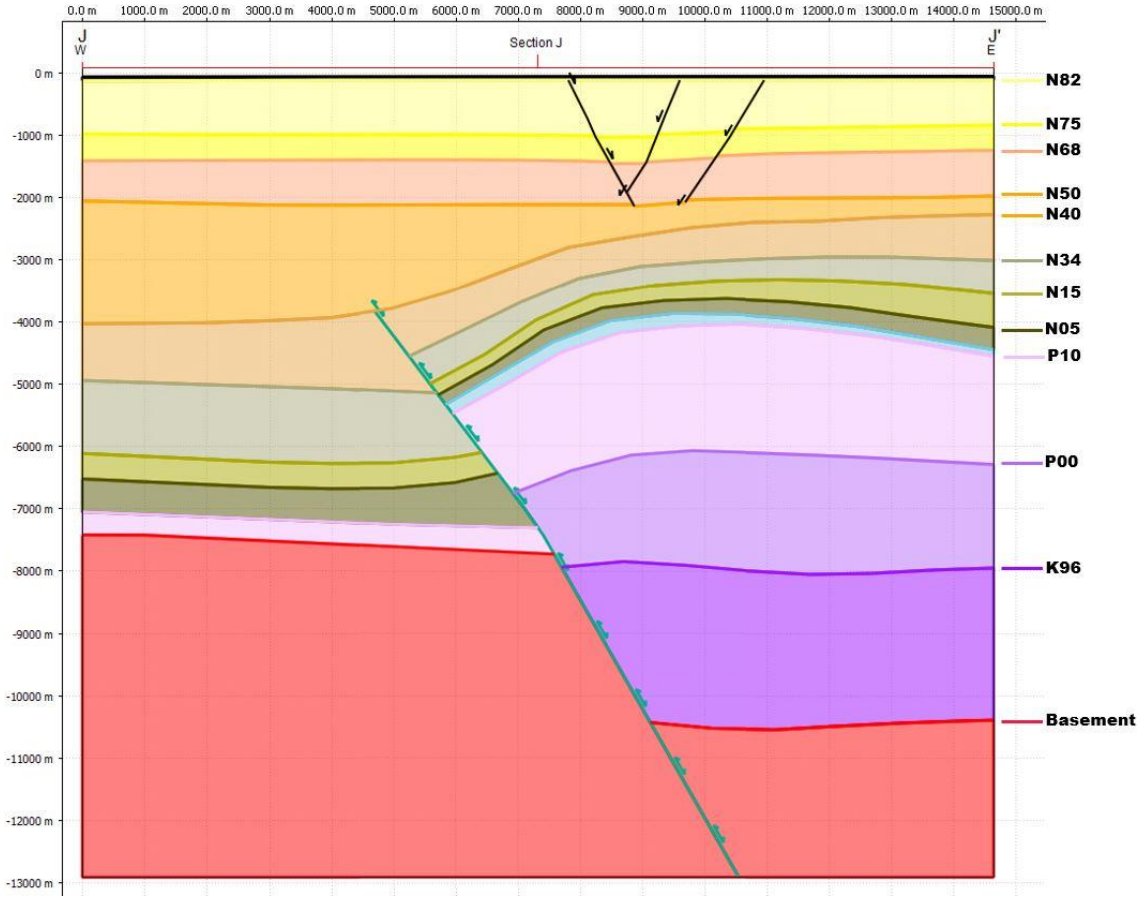

Figure 45. Depth cross section J.

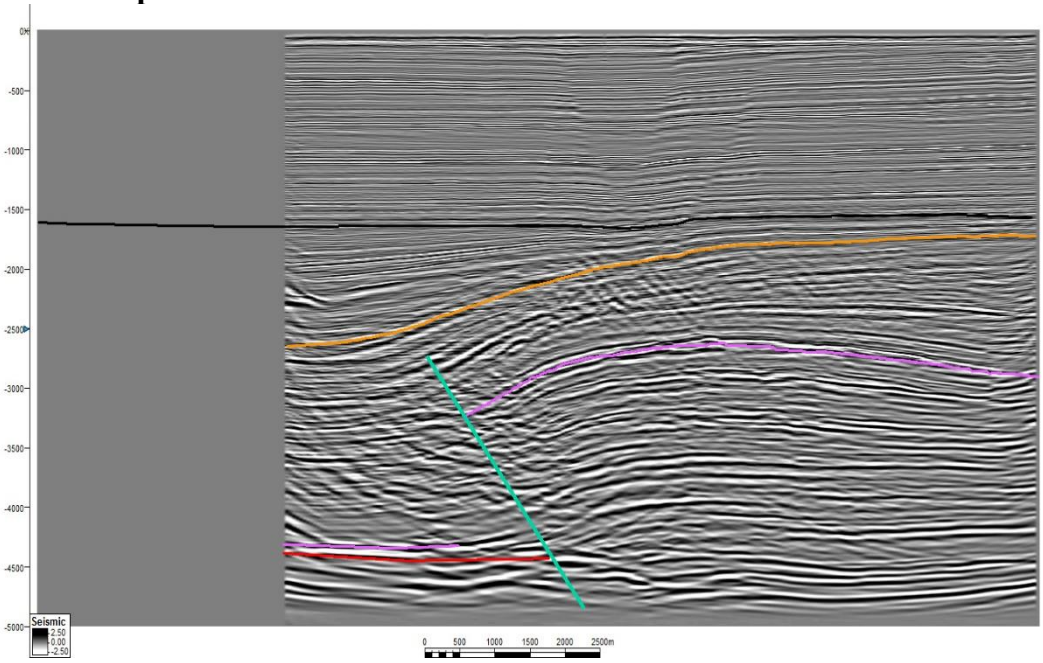

Figure 46. Time cross section J.

There are several geometric characteristics which are found in each cross section. Units deposited during extension show a general thinning away from the fault due to rollover folding. In the immediate vicinity of the fault units thin into the fault, indicative of drape or extensional fault-propagation folding. Units deposited during compression show thickening away from the crest of the anticline and thicken in the footwall.

The upper part of the Manaia fault has a gentle convex-upward bend to a shallower dip in sections A through C. This results in a gentle western dip in of the overlying beds. All units show apparent reverse offset on the Manaia fault in these sections. This suggests that the magnitude of compression exceeds extension along the Manaia fault in these sections.

The Rua fault is present in these sections and has a gentle concave downward curvature resulting from deformation from the Manaia fault. The Rua fault has apparent reverse and normal offset of the sedimentary units in sections A and B. This suggests that the magnitude of compression does not exceed the magnitude of extension on the Rua fault in this area. A flexure above the Rua fault can be seen in Section C which suggests that compressional reactivation extended at least that far to the North along the Rua fault but it resulted in fault propagation or fault-independent folding rather than slip along the fault.

In section D, compressional reactivation of the Rua fault is not directly observable. A small amount of normal offset can be seen on the P10 horizon in section D.

All apparent offset along the Rua fault ends by section E. The basement is at almost 4 seconds of seismic depth in section E and is not well imaged. It is possible that the Rua fault is still present at this interval. The two faults converge between sections A and E and it is possible that they eventually merge in this area.

In sections E and F, the front limb of the anticline has transitioned from gently dipping with broad curvature to steeply dipping with tighter curvature in the P10 through N40 Horizons. The observed geometry of the Manaia fault in these sections has a near constant 60-degree dip. The basement horizon is nearly at the null point along the fault in section E. In sections G through H, the front limb of the anticline returns to a gentle westward dip.

3.3 3D Geometry

The cross sections were used to create a 3D model. The modeled 3D fault geometries are shown in figure 47 for units deposited during extension. The top of the P10 unit, which approximates the reservoir horizon, shows that the area is marked by two overlapping structures related to the Manaia and Rua faults. The structural trap for the Kupe South field occurs in the transfer zone between the structures. The Kupe 1 well which has gas shows but no commercial accumulation is located on the northern flank of the structure related to the Manaia fault. More details regarding the variations in geometry and evolution of the structures can be obtained by analyzing variations in throw associated with extension and the total throw at the end of compression.

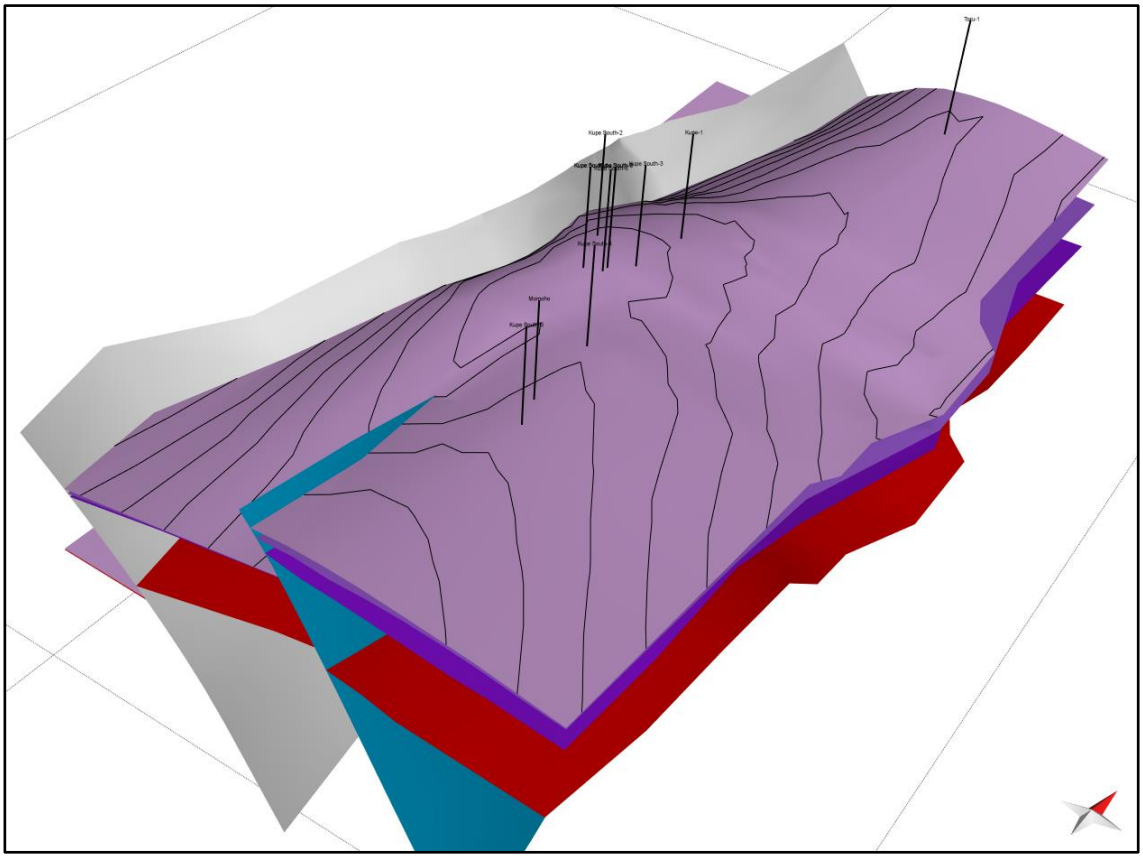

Figure 47. The 3D model showing the units deposited during extension. The Pink horizon is the approximate reservoir horizon.

The throw profile utility within the fault analysis module of Midland Valley Move was used to study the variations in throw along the faults. This utility calculates the vertical throw between the hanging wall and foot wall fault intersections of beds along a 3D model. It then allows for the back stripping of beds to show the approximate fault parameters at different times. This technique incorporates the throw lost to compressional fault propagation or extensional drape folding which are both present in the study area.

Figure 48 shows the throw of horizons at the end of extension with the Manaia fault shown as solid lines and the Rua fault shown with dashed Lines. The relative location of wells along the trend of the structure is shown at the top of the figure. Wells which produced oil are shown in green, gas are shown in red, and abandoned wells are shown in grey. The location of cross sections is shown at the bottom.

The figure shows that both the Manaia and Rua faults were active during Late Cretaceous extension. The depocenter along the Rua fault was initially located near section B but shifted to the south out of the study area during the deposition of the P00 and P10 horizons. The depocenter change is likely a result of individual faults linking together with progressive deformation. The K96 horizon shows that initially the Rua and Manaia faults had a similar magnitude of throw in the area of overlap and total throw in the area was roughly equal to the area to the north. The P00 horizon shows decreased total throw in the area of overlap with near constant throw to the north. The P10 horizon shows similar throw to the P00 horizon with a significant departure in the central part of the area. The throw of the Manaia fault increases notably to the north

between sections E and G. The location of increased throw coincides with the end of the Rua fault and the location of the Kupe and Kupe South fields. A possible explanation is that the Rua fault grew into the Manaia fault during this time and increased the total throw in this location.

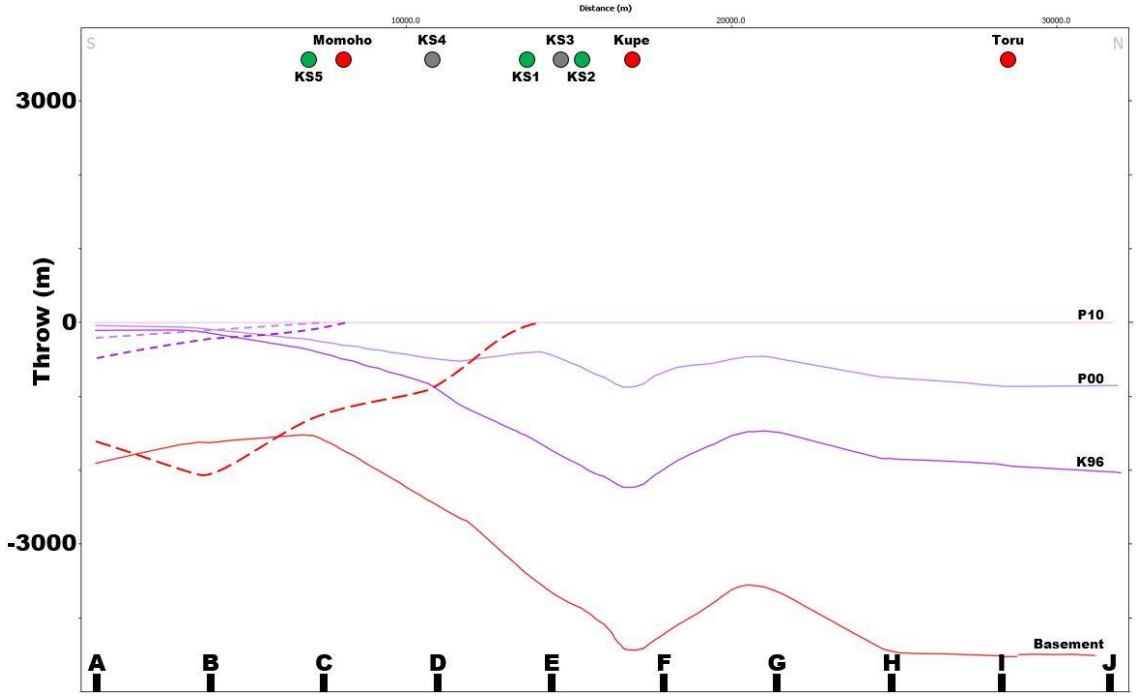

Figure 48. Fault throw at the end of extension. The Manaia fault is shown with solid lines and the Rua fault is shown with dashed lines.

Figure 49 shows the throw along the Rua and Manaia faults at the end of compression. A solid black line shows the percent throw lost to fault propagation or fault-independent folding, as modeled for the P10 horizon along the Manaia fault. The heave lost to fault propagation gives a better idea of total deformation. The Manaia fault has a near constant dip between sections D and J so heave and throw changes are directly proportional to changes in net slip. The heave lost to fault propagation as

modeled shows an approximate 50% increase in sections G through J when compared to sections D through F. Sections D through F coincide with a structural high and the location of the Kupe and Kupe South fields.

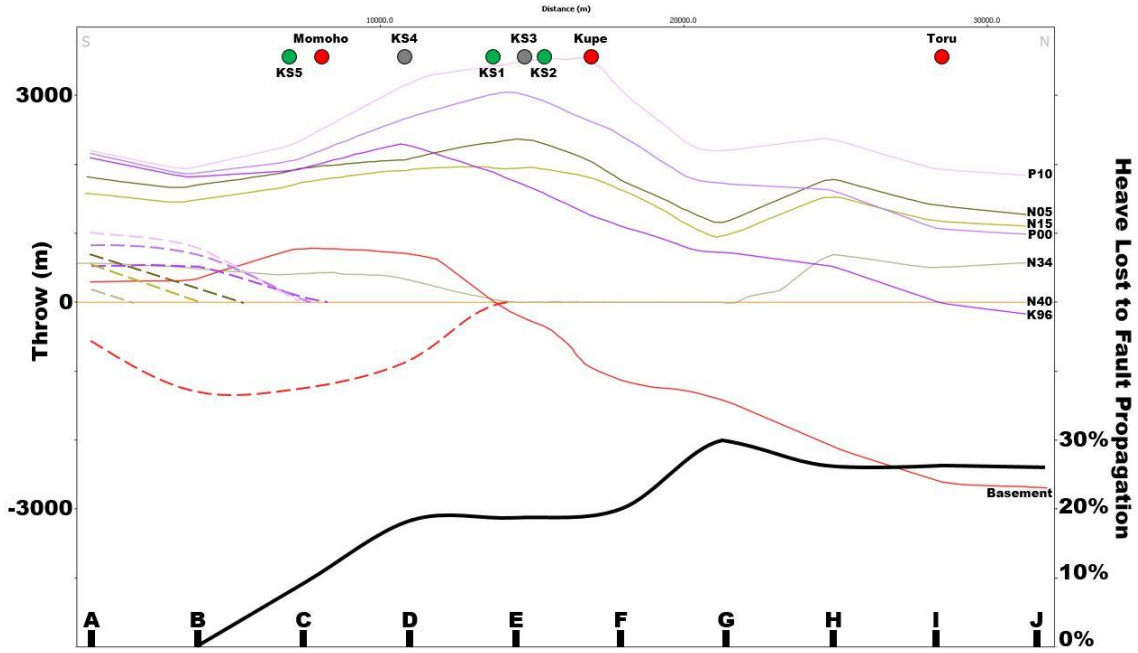

Figure 49. Cumulative fault throw at the end of compression. The Manaia fault is shown with solid lines and the Rua fault is shown with dashed lines. The percent of fault heave lost to fault propagation is shown as a solid black line.

The area between sections E and F had increased fault throw at the end of both compression and extension. The increase in fault throw in the area of fault overlap at the time when the two faults would have connected suggests that the increase is related to the interaction of the two faults. The N05 unit thins in this area which suggests that fault slip was increased in this area during the initiation of compression. This increased offset could have caused subsequent large slump features like those observed between sections D and F as shown in figure 50. The Kupe South field produces from the footwall of the northern normal faults labeled here as slump features. These normal faults show hanging wall thickening in compressional units which has led to a wide

variety of explanations. Slumping features located between two structural highs is a simple explanation which matches the observed geometry.

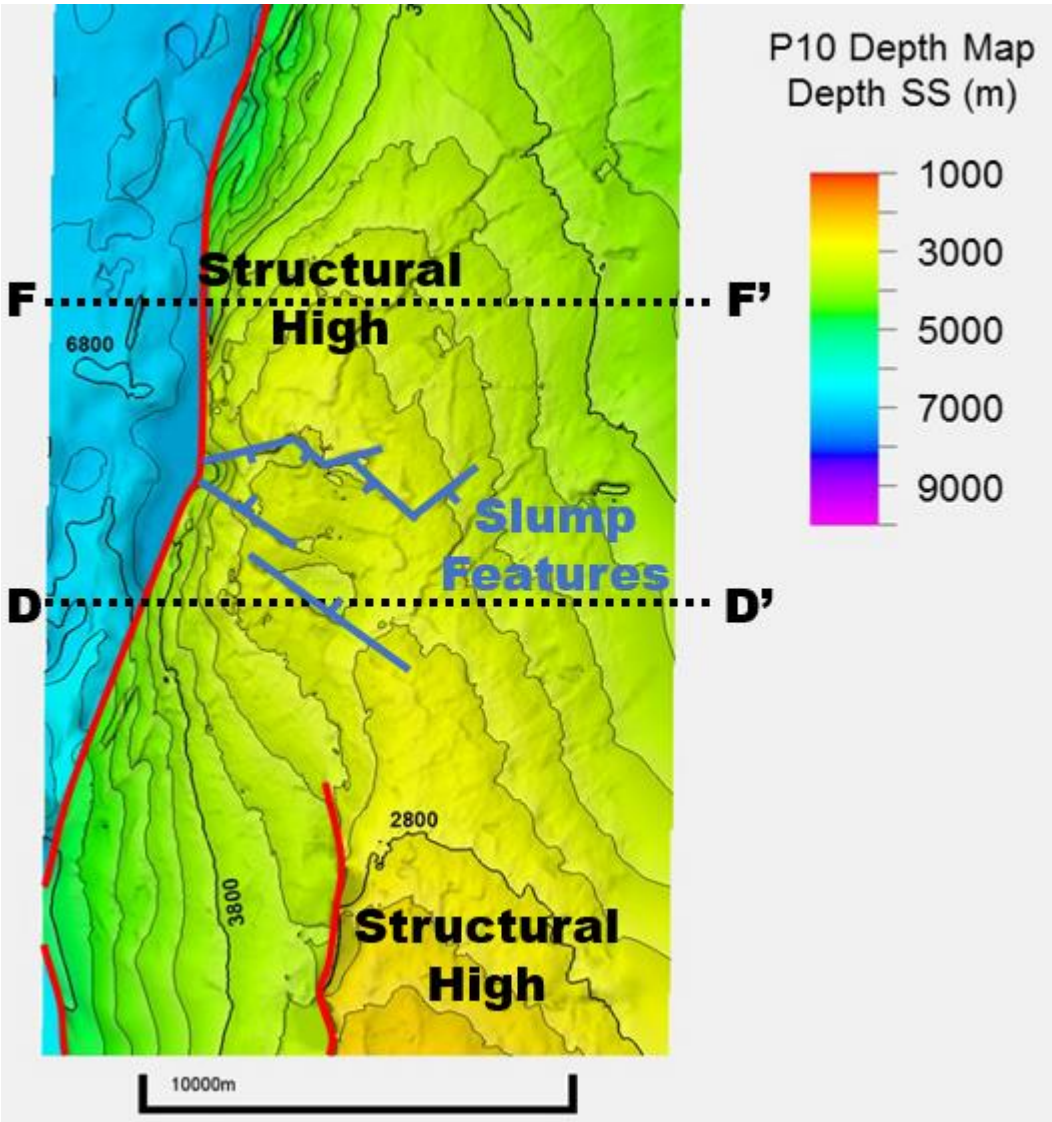

Figure 50. P10 structure map showing the location of the potential slump features.

3.4 Restorations

Restoring the sections in this area to the level at the end of the extensional phase allows for better understanding of the fold-fault relationships in the development of the structure. Restoration also enables an understanding of the thickness variation of units during the extensional phase. In the southern part of the model area the beds can be restored to the pre-compressional level using inclined shear alone. Figure 51 shows section B restored to the P10 horizon. After restoration, the two faults have simple ~60 degree dips with some shallowing in the upper part of the Manaia fault. The restoration shows significant drape folding during the deposition of the P00 unit above the Rua fault.

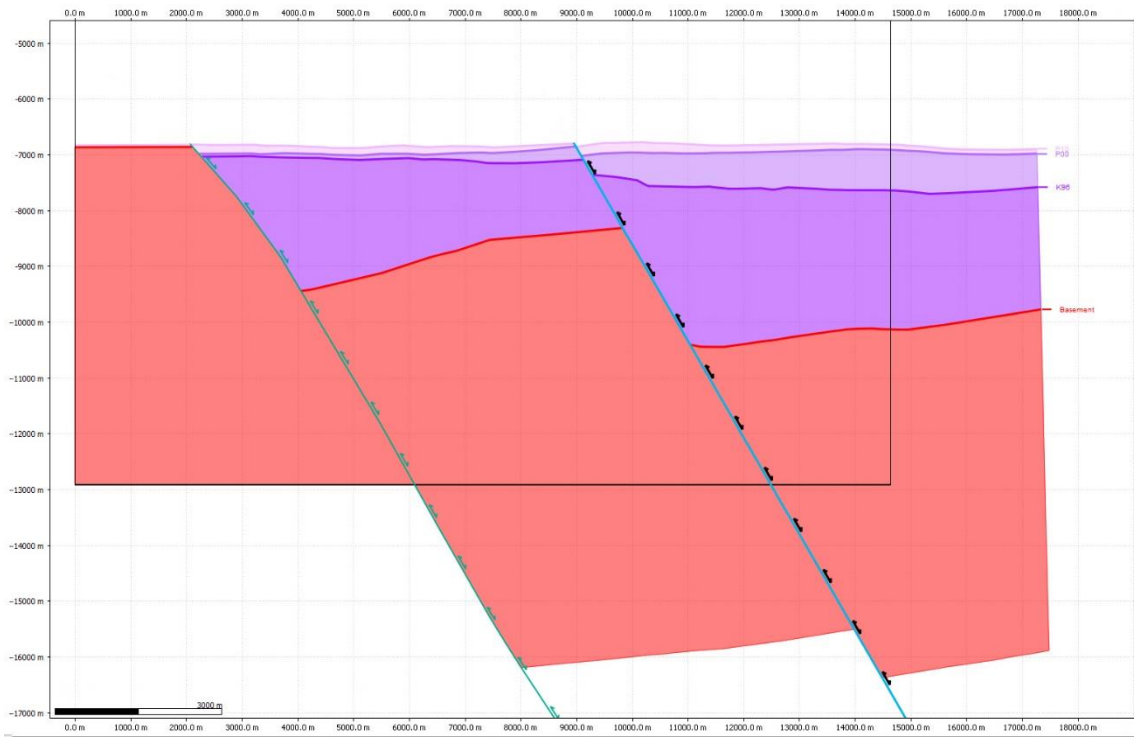

Figure 51. Section B inclined shear restoration.

Structures in the central and northern parts of the area involve both fault bend folding and some component of fault-propagation or fault-independent folding. Therefore, restoration of the sections requires a two-step process to account for the two mechanisms. The first step uses inclined shear to restore the fault-bend folding component. This is followed by unfolding using a flexural-slip restoration with the fault as a pin.

Figure 52 shows the inclined shear component of restoration and figure 53 shows the final restored geometry after the unfolding component of restoration in section E. Section E is in the area of the Kupe South oil wells. The restored section shows significant drape folding during the deposition of the P10 unit. The depocenter is located close to the fault and nearly vertically above the hanging wall basement fault intersection.

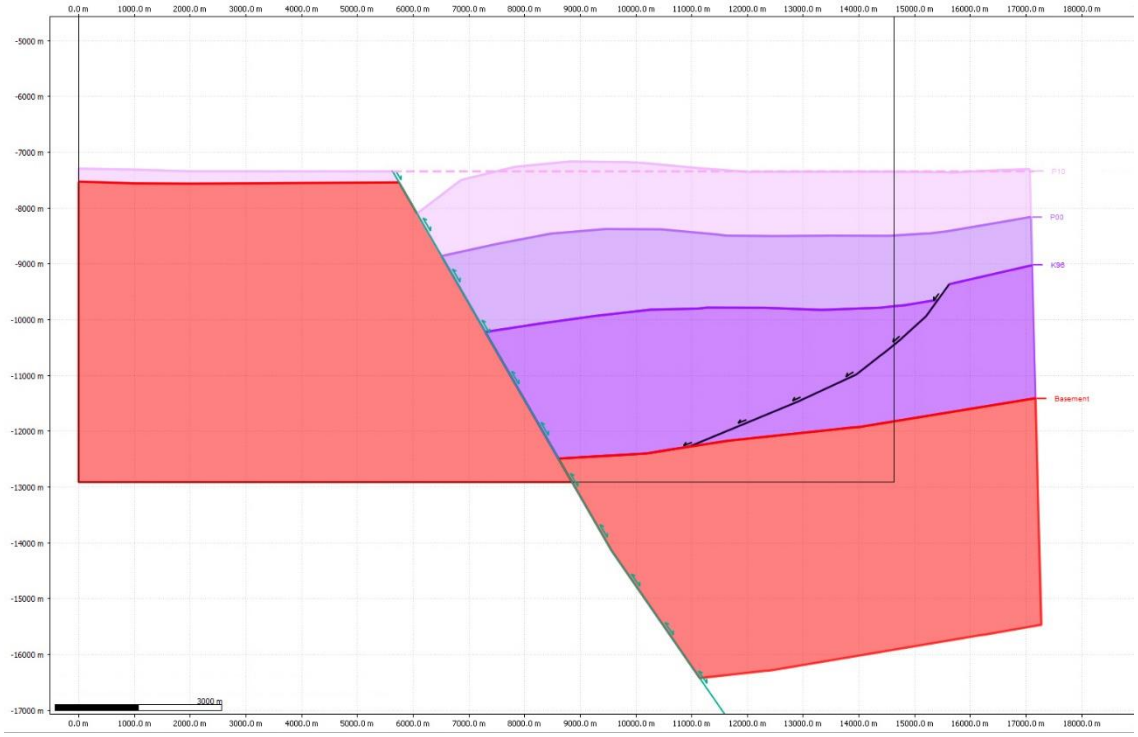

Figure 52. Section E inclined shear restoration.

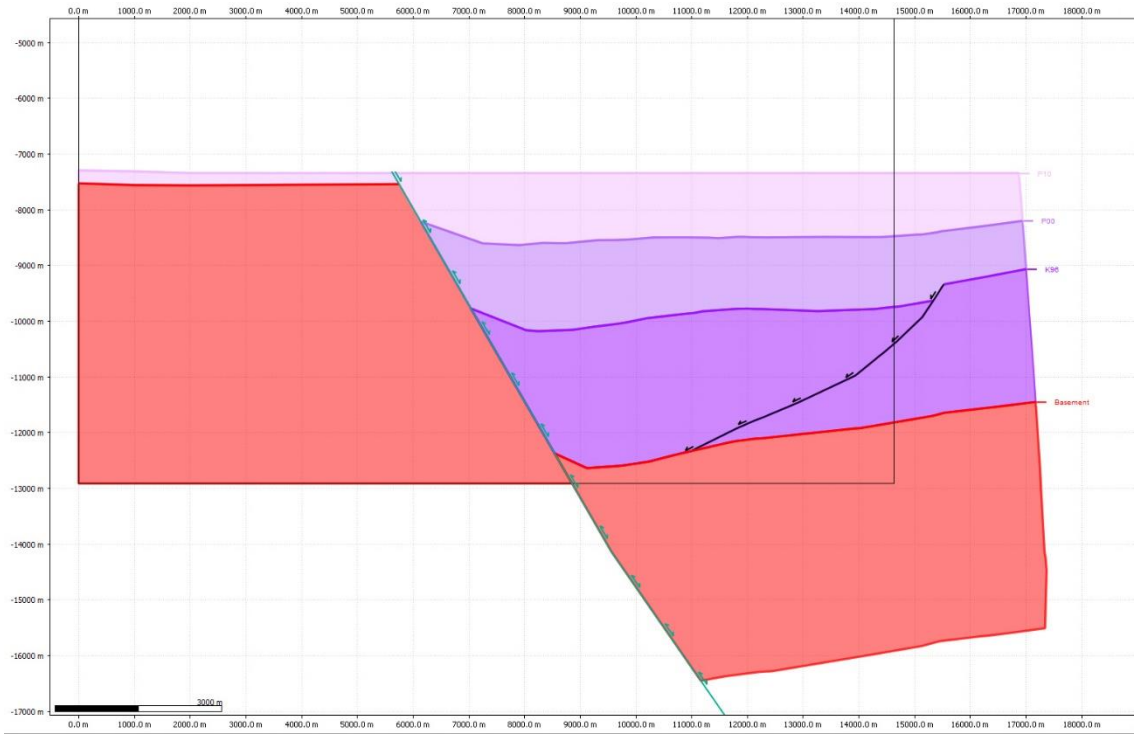

Figure 53. Section E restored section.

Figure 54 shows the inclined shear component of restoration and figure 55 shows the final restored geometry after applying flexural-slip unfolding to section I. Section I is in the area of the Toru oil well. The restored section shows significant drape folding during the deposition of the P00 and K96 units with minor drape folding in the P10 unit. The depocenter is located further away from the fault and nearly vertically above the hanging wall basement-fault intersection.

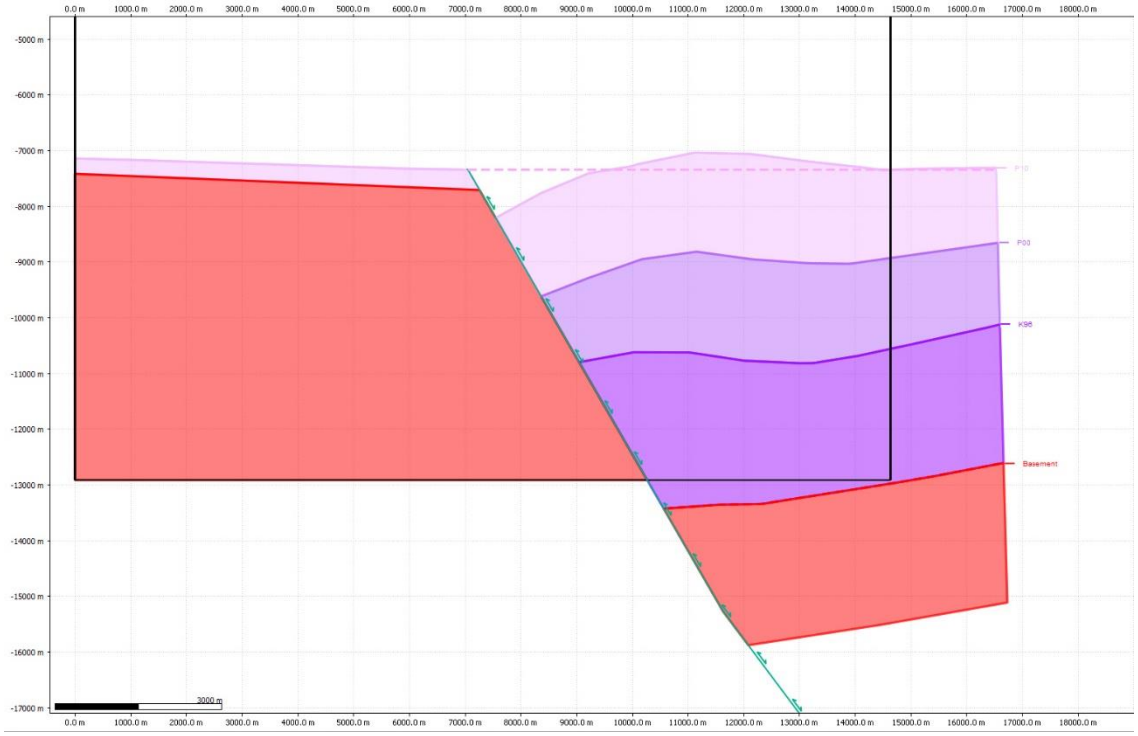

Figure 54. Section I inclined shear restoration.

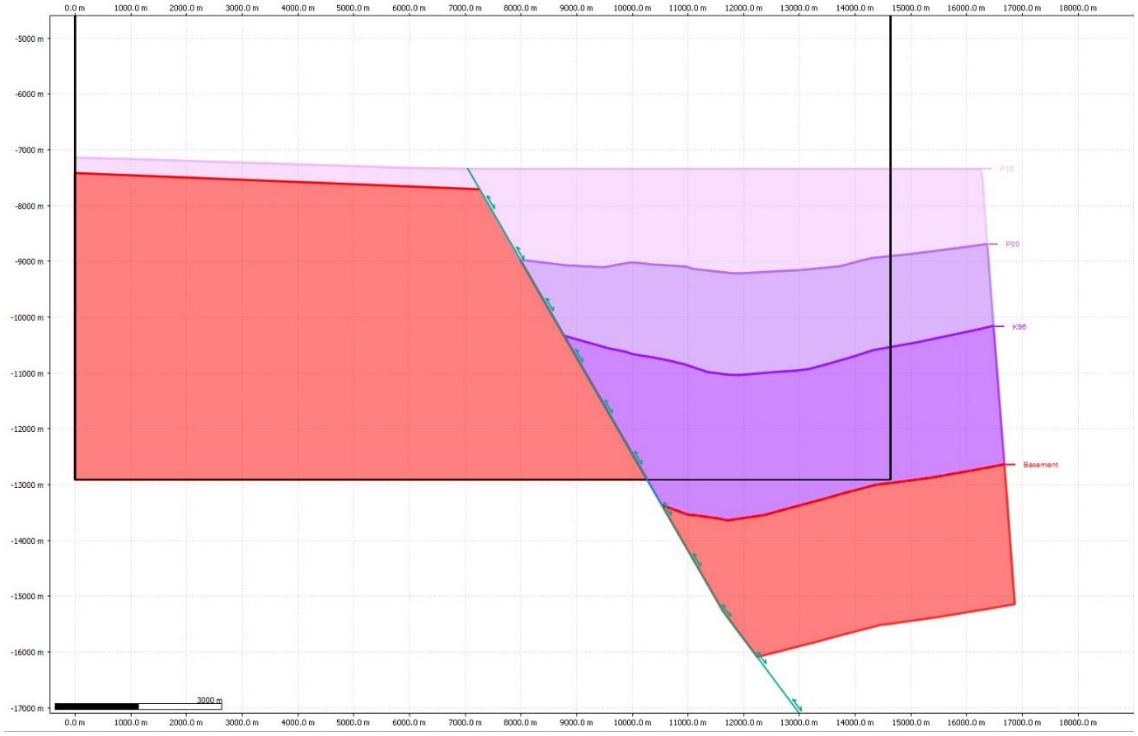

Figure 55. Section I restored section.

Chapter 4. Discussion

4.1 Fault Propagation in Inversion Structures

The style of fault propagation folding observed in this study has been observed by others in inversion structures (Mitra, 2005). Figure 56 shows a cross section of the Maui field from Abbott, 1990. This is an inversion structure in the Taranaki basin with a similar geologic history to the Kupe structure. The distinct downward flexure near the fault followed by an upward flexure away from the fault before returning to a gently dipping back limb is observed. A similar geometry is present in other inversion structures within the Taranaki Basin.

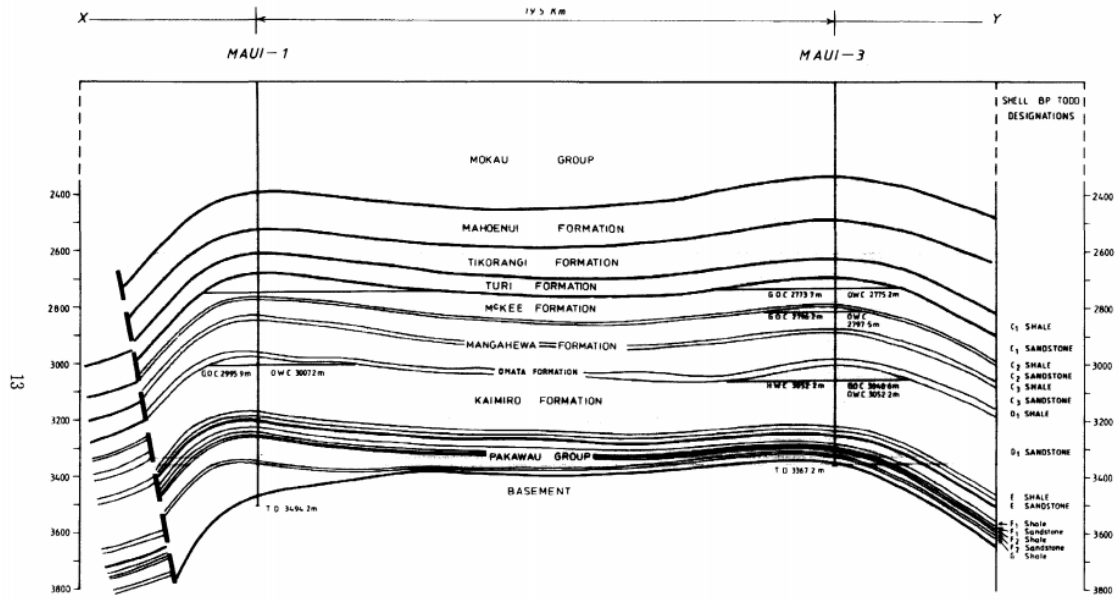

Figure 56. Structural cross section of the Maui structure in the Taranaki basin of New Zealand from Abbott (1990) showing folding adjacent to a compressionally reactivated normal fault.

Figure 57 shows an inversion structure in the Wessex Basin of southern England. Two faults are present in the cross section. The central fault is interpreted to

be a normal fault with drape folding causing flexures in the hanging wall and footwall. The fault located in the right side of the figure is interpreted as being a normal fault with compressional reactivation. A downward flexure can be seen against the fault with an upward flexure away from the fault before returning to a gentle dip away from the fault.

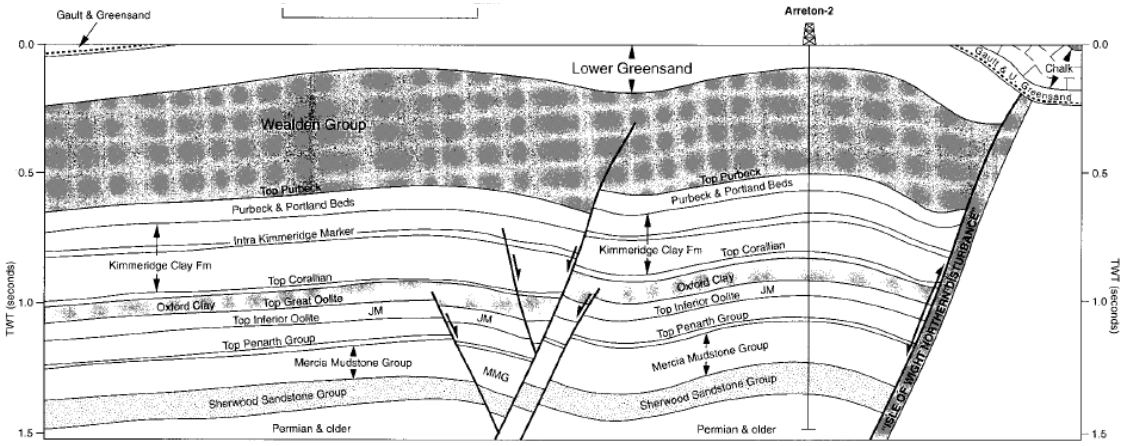

Figure 57. Structural cross section of the Arreton structure in the Wessex basin of southern England from Underhill and Patterson (1998) showing folding adjacent to a compressionally reactivated normal fault.

Figure 58 shows the Sakala inversion structure which is located in the East Java Sea. Image A shows the interpreted fault geometry with the extensional units shown in the yellow polygon. The geometry of the extensional units exhibits the same style of fault propagation as this study. Image B shows a restoration of the extensional units. The area balancing method used in this study was used to restore this section.

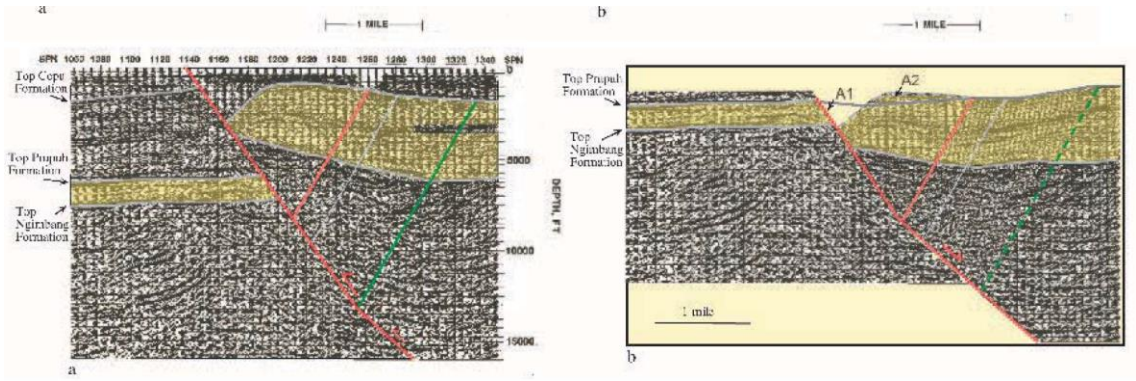

Figure 58. Structural cross section of the Sakala structure in the East Java Sea from Mitra (2005) showing folding adjacent to a compressionally reactivated normal fault.

The examples shown above from existing literature show that this style of fault propagation can be found in inversion structures with diverse locations, lithologies, and timing of deformation. Several mechanisms have been suggested and observed for folding along inverted faults. Cooper et al. (1989) and Hayward and Graham (1989) both noted that anticlines tend to form over inversion structures. They suggested that buttressing caused ductile deformation of incompetent units resulting in folding of upper units as shown in figure 59. The fault is not shown breaking through the upper beds but would with progressive deformation. Underhill and Paterson (1998) observed flexural slip and back thrusting above an inverted fault in the Wessex Basin as shown in figure 60. This resulted in thinning of units along the fault with thickening away from the fault. The style of fault propagation found in this study likely results from a combination of multiple deformation mechanisms. Analog models created by Buchanan and McClay (1991), Bulnes and McClay (1999), and Mitra and Islam (1994) have shown similar deformation mechanisms to the examples.

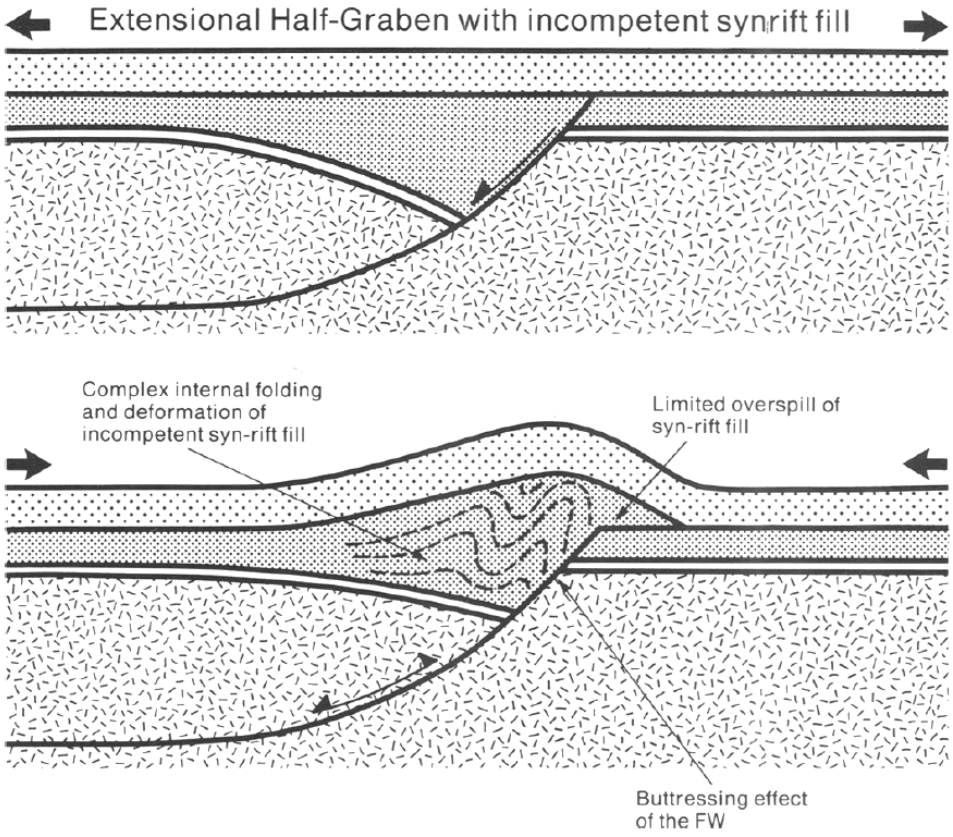

Figure 59. Fault-independent buckle folding through buttressing of incompetent units. The footwall is un-deformed and deformation is confined to the hanging wall. (Cooper, 1989)

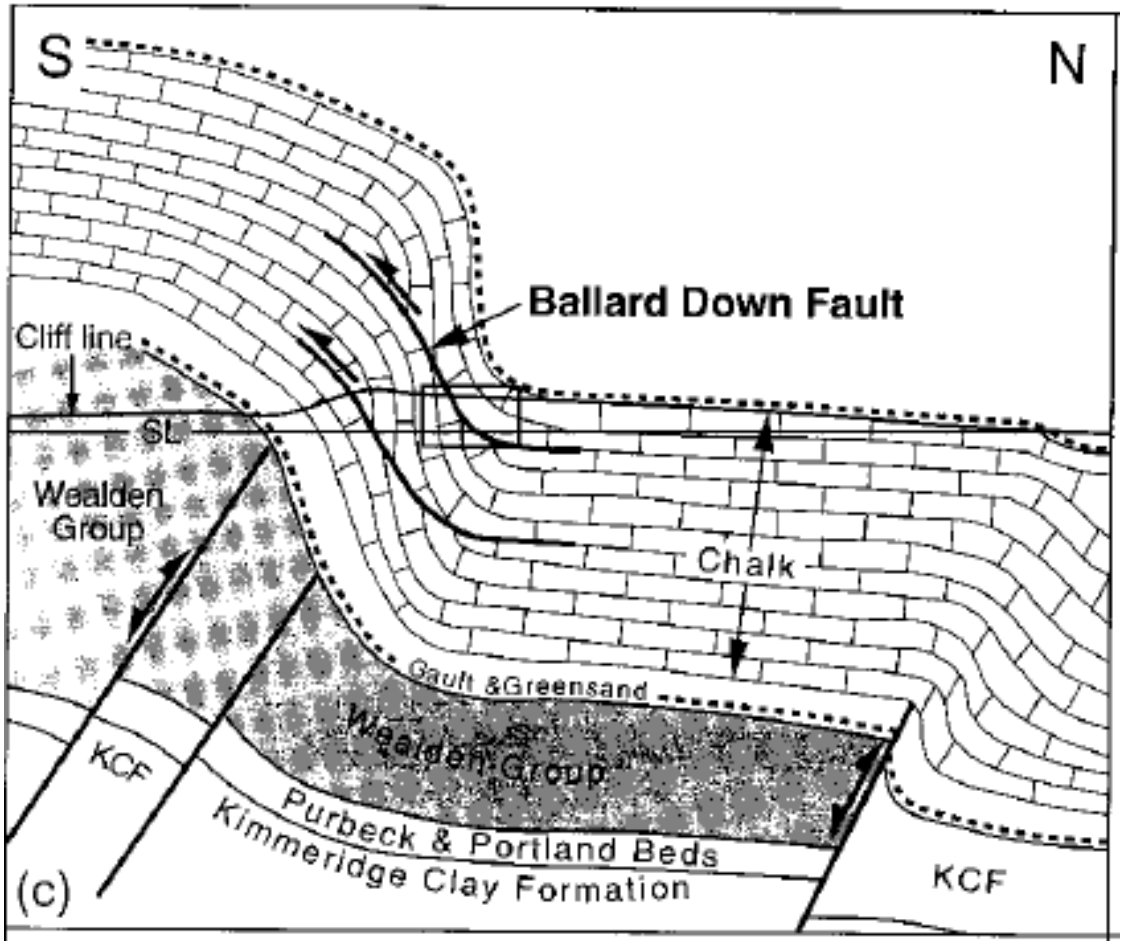

Figure 60. Fault propagation accommodated by back thrusts. (Underhill and Patterson, 1998)

A simple analysis of the geometry observed in this study suggests that this style of fault propagation behaves in a predictable manner. Figure 61 shows the area lost and gained above and below the bed geometry predicted by inclined shear for the pink P10 and purple P00 horizon for section I. The percent area lost can be calculated by dividing A by B and the percent area gained can be calculated dividing C by D.

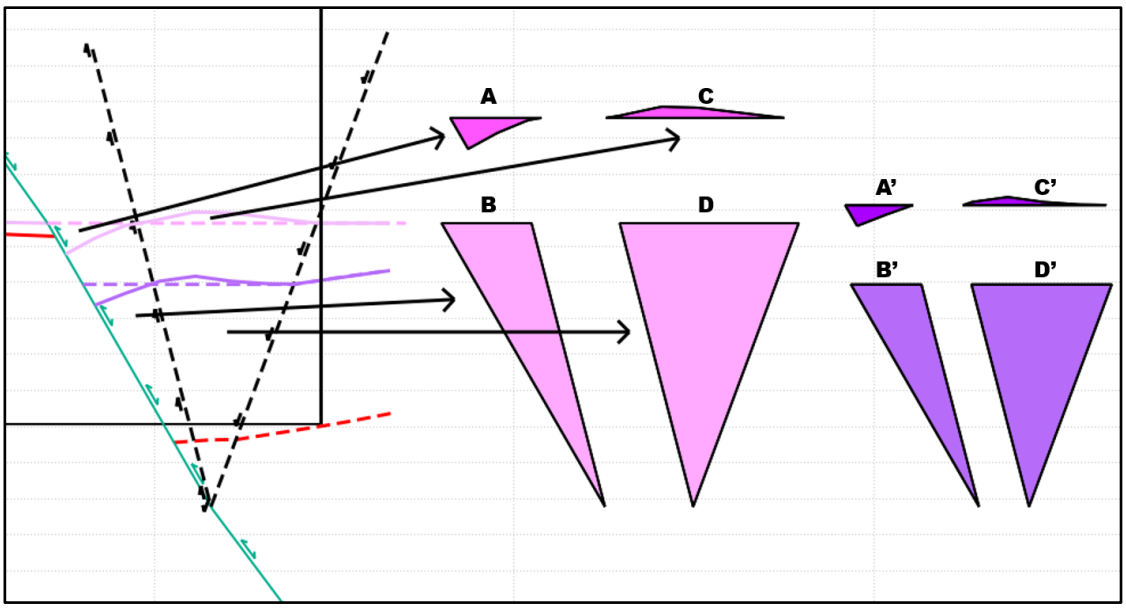

Figure 61. A representation of how the percent area lost and gained can be calculated. The area within the downward and upward folding deformation panels are calculated between the modeled horizon and the observed horizon. This is then compared to the total area below the modeled horizon within the deformation panel. The areas A/B=A'/B' and C/D=C'/D'.

These calculations resulted in an area gain of 4.5% for P10 and 3.4% for P00. The calculated area loss was 10.7% for P10 and 9.5% for P00. The calculated area relationships are similarly consistent when calculated for other sections within the model and when calculated for other published sections. Some of the inconsistency in percent area change is likely a result of drape folding during extension. These relatively consistent area changes would suggest that a method for modeling bed geometries and unfolding deformation could be developed.

A proposed unfolding technique is shown in figure 62. This technique assumes that the observed bed geometries are located a set percentage above or below the predicted inclined shear location along a vector radiating from the base of the triangular deformation zone from the base of the triangular deformation zone. Figure 62 shows the

inclined shear restored geometry of the P10 and P00 horizon for section I. To manually unfold these beds using the pink P10 horizon as a template and P00 as a passive bed first the percent line length along a line must be calculated. The figure shows the line lengths which need to be measured for along the fault with red arrows. The lengths for these lines are 9083.4m for line AE, 995m for line AB, 7120.7m for line CE, and 665.2m for line CD. The percent length change for the P10 horizon calculated as AB divided by AE is 11% and 9.3% for the P00 horizon. This suggests that the stratigraphic thickness of P10 was originally thinned by drape folding during deposition. Moving the P00 horizon up 11% will move it above the modeled location.

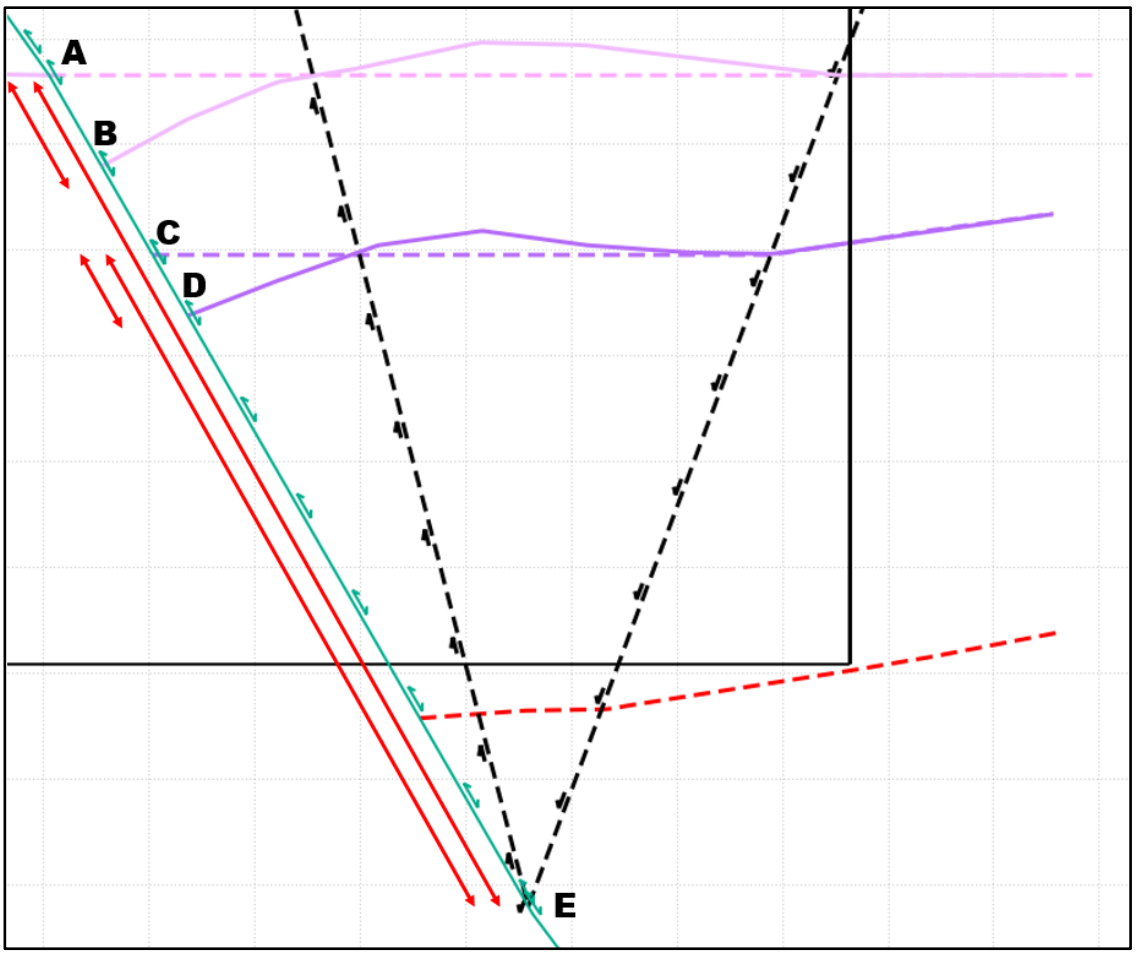

Figure 62. The basic approach to unfolding uses the length of the modeled bed to the base of the triangular deformation zone (Line AE) and the length from the modeled bed to the observed horizon (AB) to maintain a constant percent length change. A bed can be passively unfolded using AB/AE=X/DE where X is the unknown length which the bed should be unfolded. The unknown X should move the bed more than the length DC to restore the bed above the modeled position resulting in a drape folded geometry.

Figure 63 shows the results of passively unfolding the P00 horizon using the P10 horizon. The result of the method described above using the dashed lines and the fault is shown in red. The inclined shear geometry is shown in dashed purple and the blue line was passively flattened using flexural slip pinned to the fault. The two unfolded geometries are similar and show drape folding with the depocenter away from

the fault. The new method of unfolding has some notable differences. First the flexural slip unfolding shows a minor depocenter close to the fault with the major depocenter away from the fault. The new method shows only one depocenter with a consistent gentle dip towards the depocenter in both directions. The magnitude of drape folding is also decreased by the new method. This same approach could be used to model horizons which are poorly imaged. In the model area, this modeling method would have limited use because it would not account for drape folding. Drape folding could be manually accounted for to give a rough estimation of bed location.

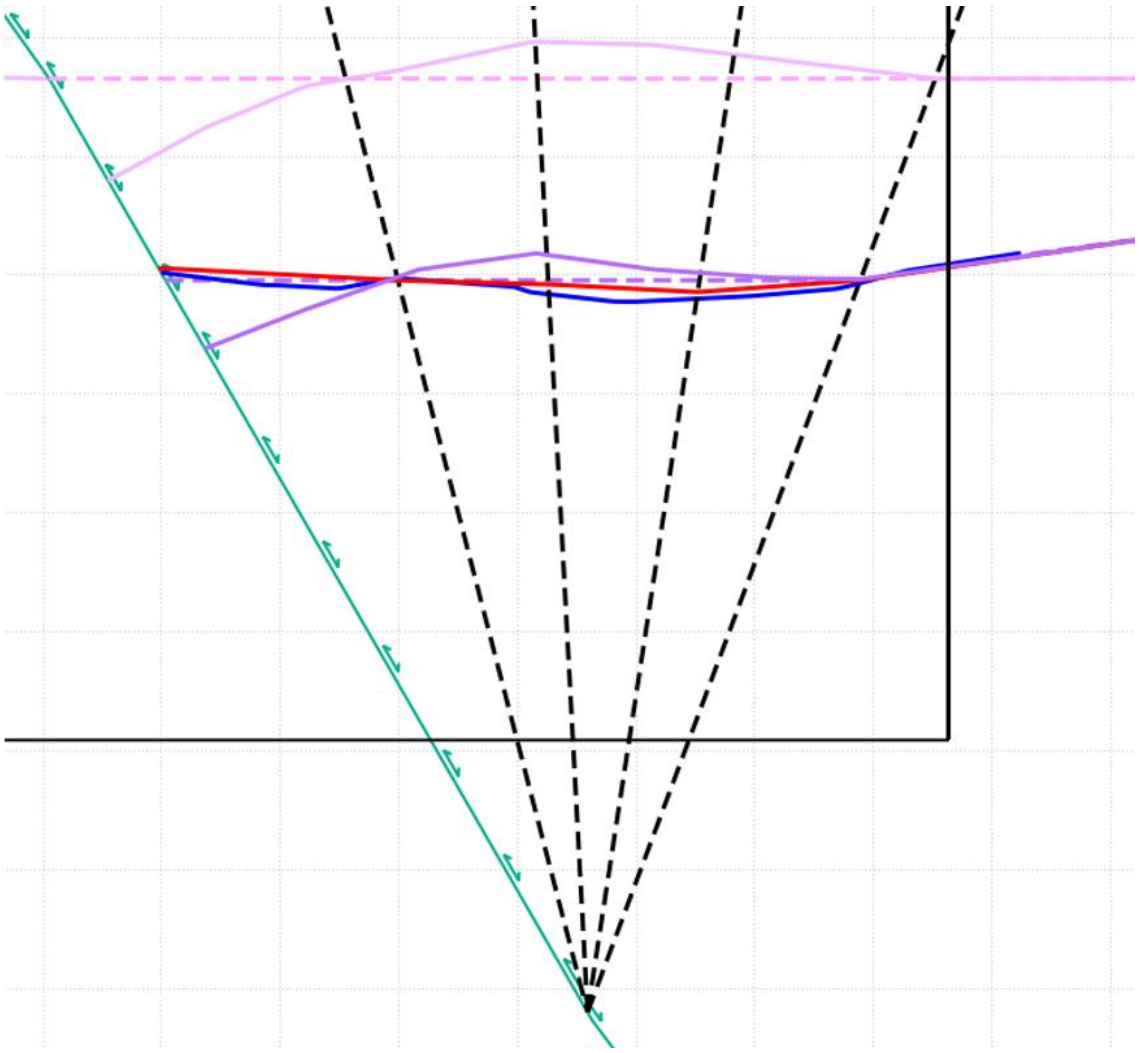

Figure 63. Comparison of passive unfolding techniques of the purple P00 horizon using the pink P10 as a template. The red line shows the output using the new technique and the blue line shows the output using flexural slip with the fault as a pin.

The comparison of the proposed unfolding method and the flexural slip algorithm shows that the two methods give similar and compatible outputs in the given situation. The proposed unfolding method gives an apparently geologically valid output. The proposed unfolding and associated bed modeling method are highly interpretive. It requires the user to interpret the location of the fault, the plane separating upward and downward flexure, and the plane defining the extent of folding. When coupled with the

uncertainties of inclined shear modeling the possible output geometries can vary greatly. The proposed methodologies are a hypothesis and further study is needed before they can be used as anything more than a hypothesis.

4.2 Deep fault geometry

The cross sections in section 3.2 of this study are cutoff at 11km of depth but the fault was modeled to the detachment depth of more than 30km at the brittle-ductile transition. Data outside of the Kerry 3D seismic dataset is needed to model the full extent of the Manaia and Rua faults. Depth structure contour maps available from Fohrmann et al. (2012) were used to extend the horizons. This data has a lower resolution and uncertainty in fault modeling increases with depth.

Figure 64 shows the basement and figure 65 shows the P10 structure map from Fohrmann et al. The location and extent of the Kerry3D dataset is shown with a black outline. The P10 horizon map shows that the P10 horizon never returns to the Manaia fault foot wall level in the hanging wall. This causes a very deep detachment level when modeling the fault. Additional reverse faults could cause this, but the maps show no reverse faults between the Manaia fault and the eastern Taranaki fault.

Stagpoole and Nicol (2008) used gravity, resistivity, and seismic profiles to show that the Taranaki fault is a large back thrust coming off the subduction zone to the east. The modeled deep fault geometry has a similar geometry to the Taranaki fault geometry suggested by Stagpoole and Nicol. The Modeled geometry is shown on their gravity model in figure 66 with the modeled geometry enlarged below. The extent of the fault which can be modeled using inclined shear is shown with a black line. The relationship with the Taranaki fault and the subduction zone to the East help explain the very deep detachment level.

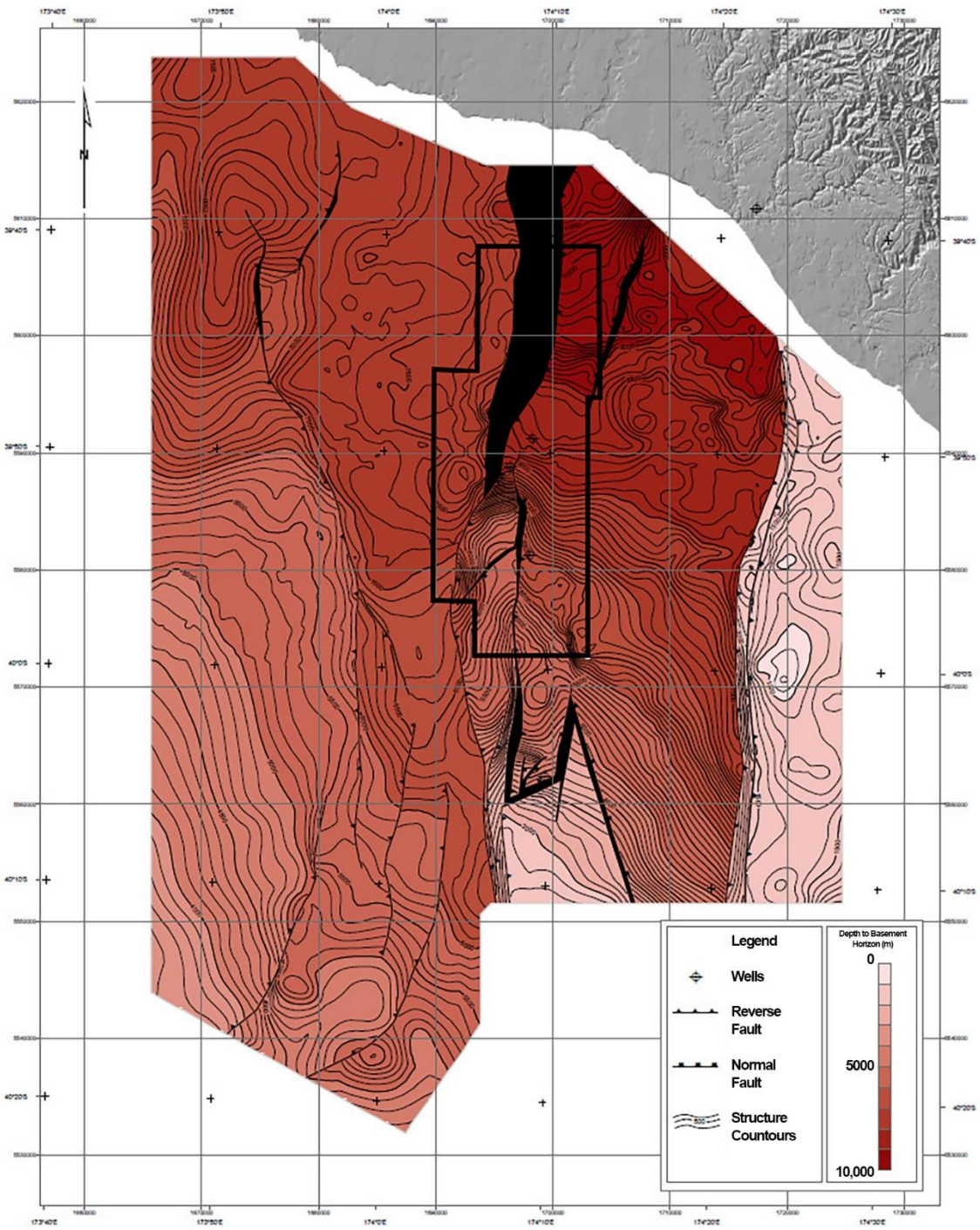

Figure 64. Basement horizon structure map from Fohrmann et al. (2012)

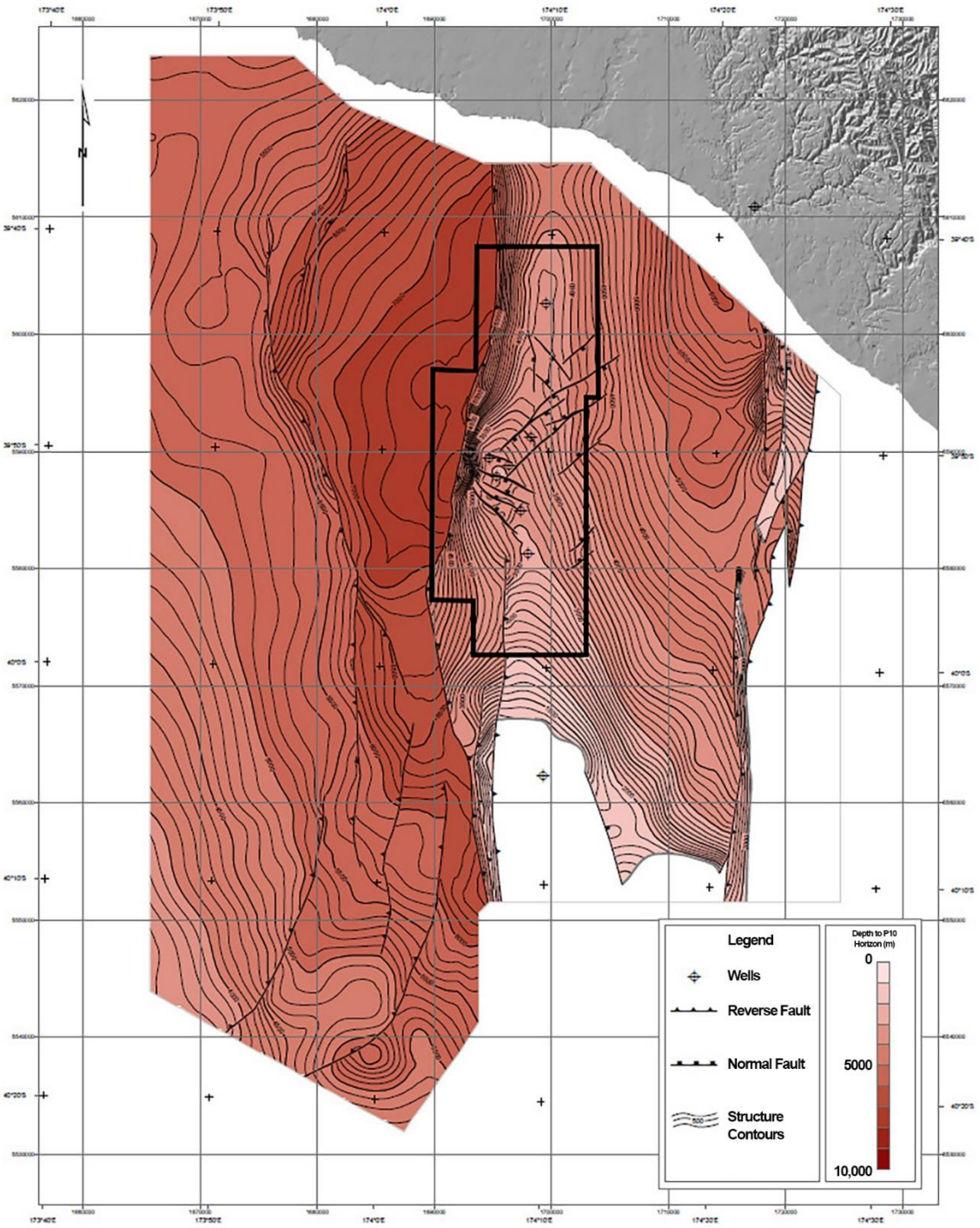

Figure 65. P10 horizon structure map from Fohrmann et al. (2012)

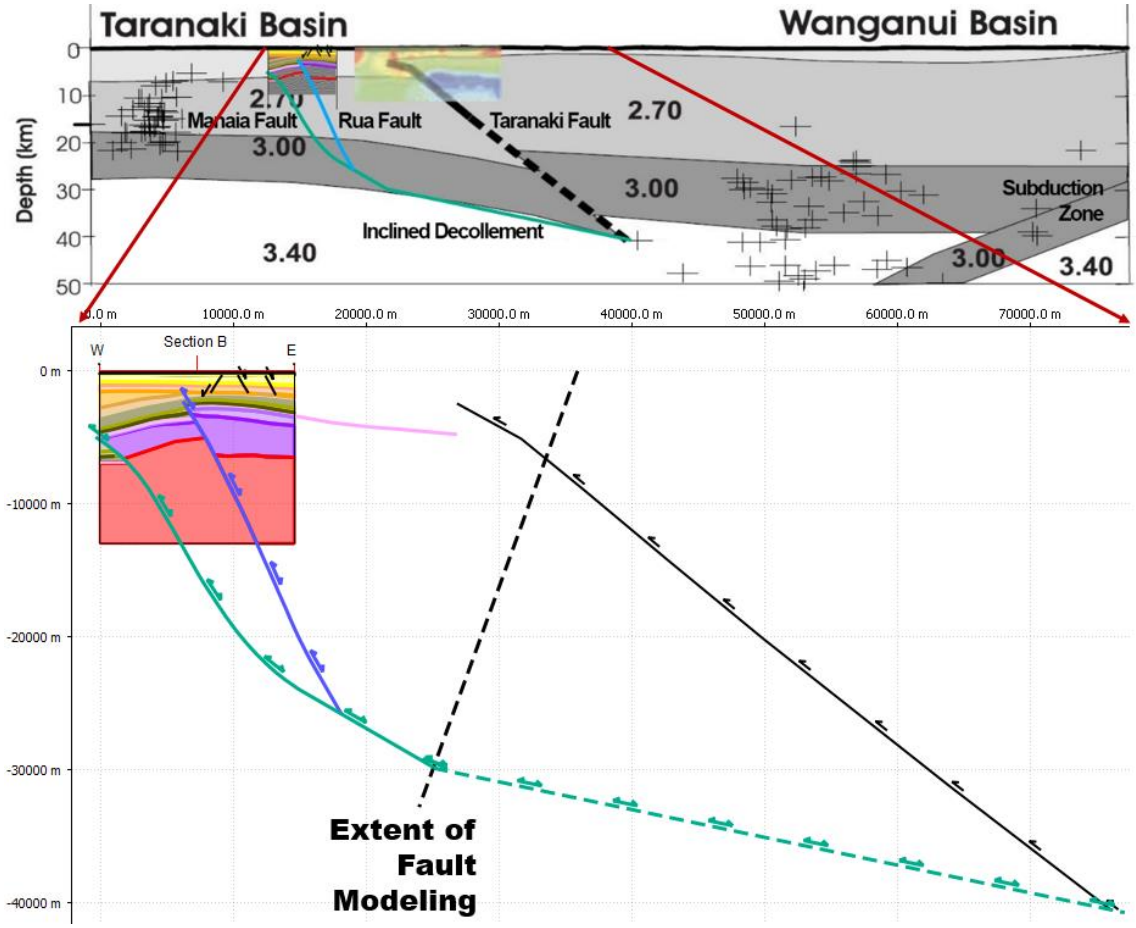

Figure 66. The deep fault geometry is shown on the gravity model created by Stagpoole and Nicol (2008). Below that the deep fault geometry is expanded to show detail. The dashed black line shows the extent of the fault which can be modeled from the horizon do to the presence of the Taranaki fault which is shown in black.

Summary

The Kupe structure located in the Southern Taranaki Basin of New Zealand, is an asymmetric fault cored anticline which formed as the result of compressional reactivation of two overlapping crustal scale listric normal faults. The area was subject to extension from the Late Cretaceous to the Eocene because of the breakup of Gondwana and seafloor spreading in the Tasman Sea. The Manaia and Rua normal faults were then reactivated in the Oligoene to Miocene because of the subduction zone to the East.

The structure shows deformation resulting from fault bend folding and fault propagation or fault independent folding. A modified inclined shear technique was used to model the Rua and Manaia faults. A 3D model was created to analyze the structure. The Manaia fault has a near constant 60-degree dip in the upper crust in the central and northern parts of the study area and the fault dip progressively decreases to the south. This model shows that fault propagation decreases along the Manaia fault to the south. In the area of overlap between the two faults slip progressively transfers from the Manaia to the Rua fault to the south. The structural high which forms the trap for the Kupe South Field is caused by the overlap of the two faults. Increased fault slip causes the structural high.

References

Abbott, W.O., (1990), Maui Field, in E. A. Beaumont and N. H. Foster, eds., Structural Traps I: Tectonic Fold Traps: Tulsa, Oklahoma, AAPG, 1-21.

Bull, S., M. Hill, M. Arnot, H. Seebeck, K. Kroeger, H. Zhu, and C. Reilly, 2015, Time Structure and Isochron Maps from the Southern Taranaki Basin (4D Taranaki Project): GNS Science Data Series 12b.

Bulnes, M., & McClay, K. (1999). Benefits and limitations of different 2D algorithms used in cross-section restoration of inverted extensional faults: application to physical experiments. Tectonophysics, 312(2), 175-189.

Buchanan, P. G., & McClay, K. R. (1991). Sandbox experiments of inverted listric and planar fault systems. Tectonophysics, 188(1-2), 97-115.

CGG Australia Services Pty Ltd, 2004, Reprocessing Report for Kerry 3D Survey: Origin Energy Resources Limited - KS96 Kerry 3D Marine Project No: 502p1cz

Cooper, M. A., Williams, G. D., De Graciansky, P. C., Murphy, R. W., Needham, T., De Paor, D.. & Ziegler, P. A. (1989). Inversion tectonics—a discussion. *Geological Society, London, Special Publications*, *44*(1), 335-347.

Dula Jr, W. F. (1991). Geometric Models of Listric Normal Faults and Rollover Folds (1). *AAPG Bulletin*, *75*(10), 1609-1625.

Erslev, E. A. (1991). Trishear fault-propagation folding. Geology, 19(6), 617-620. Chicago

Fohrmann, M., Reid, E., Hill, M. G., King, P. R., Zhu, H., Bland, K. J., ... & Scott, G. P. L. (2012). Seismic reflection character, mapping and tectono-stratigraphic history of the Kupe area (4D Taranaki Project), south-eastern Taranaki Basin. GNS Science.

Hayward, A. B., & Graham, R. H. (1989). Some geometrical characteristics of inversion. Geological Society, London, Special Publications, 44(1), 17-39.

Hill, M., Fohrmann, M., Zhu, H., & Bull, S. (2013) Velocity Modelling in the Southern Taranaki Basin 4D Taranaki Project.

Hill, M. G., & Milner, M. (2012). The Kupe velocity model-4D Taranaki Project. *Lower Hutt: GNS Science. GNS Science report*, *37*, 39.

King, P. R., & Thrasher, G. P. (1996). Cretaceous Cenozoic geology and petroleum systems of the Taranaki Basin, New Zealand (Vol. 2). Institute of Geological & Nuclear Sciences.

Mitra, S. (1993). Geometry and kinematic evolution of inversion structures. *AAPG Bulletin*, *77*(7), 1159-1191.

Mitra, S., & Islam, Q. T. (1994). Experimental (clay) models of inversion structures. Tectonophysics, 230(3-4), 211-222.

Mitra, S. (2005). Structural inversion along the Sakala Fault, East Java Sea, Indonesia. *Seismic Interpretation of Contractional Fault-Related Folds. American Association of Petroleum Geologists Seismic Atlas, Studies in Geology*, *53*, 100-102.

Reilly, C., Nicol, A., Walsh, J. J., & Seebeck, H. (2015). Evolution of faulting and plate boundary deformation in the Southern Taranaki Basin, New Zealand. Tectonophysics, 651, 1-18.

Roncaglia, L., Arnot, M., Baur, J., Fohrmann, M., King, P., Kroeger, K. F., ... & Milner, M. (2010, January). Integrated workflow for modeling basin-scale petroleum systems: applications to the Kupe area, Taranaki, New Zealand. In SPE Annual Technical Conference and Exhibition. Society of Petroleum Engineers. Chicago

Stagpoole, V., & Nicol, A. (2008). Regional structure and kinematic history of a large subduction back thrust: Taranaki Fault, New Zealand. *Journal of Geophysical Research: Solid Earth*, *113*(B1).

Underhill, J. R., & Paterson, S. (1998). Genesis of tectonic inversion structures: seismic evidence for the development of key structures along the Purbeck–Isle of Wight Disturbance. Journal of the Geological Society, 155(6), 975-992.

Wandrey, C. J., Schenk, C. J., Klett, T. R., Brownfield, M. E., Charpentier, R. R., Cook, T. A., ... & Tennyson, M. E. (2013). *Assessment of undiscovered oil and gas resources of the Cretaceous-Tertiary Composite Total Petroleum System, Taranaki Basin Assessment Unit, New Zealand* (No. 2012-3139). US Geological Survey.

Xiao, H. (1990). Kinematics and mechanics of normal faulting and associated folding with applications to the Gulf of Mexico. Princeton University, Princeton, New Jersey, Ph.D. dissertation, 133.